This is to certify that the
thesis entitled

A COMPREHENSIVE STUDY OF A REGIONAL SCALE DOWNSLOPE FLOW IN NORTHERN ARIZONA

presented by

LOWELL CROSBY SAVAGE III

has been accepted towards fulfillment
of the requirements for the

M.S. degree in Geography

Major Professor's Signature

May 20, 2008

Date

A COMPREHENSIVE STUDY OF A REGIONAL SCALE DOWNSLOPE FLOW IN NORTHERN ARIZONA

By

Lowell Crosby Savage III

A THESIS

Submitted to
Michigan State University
in partial fulfillment of the requirements
for the degree of

MASTER OF SCIENCE

Department of Geography

2008

ABSTRACT

A COMPREHENSIVE STUDY OF A REGIONAL SCALE DOWNSLOPE FLOW IN NORTHERN ARIZONA

By

Lowell Crosby Savage III

The consequences of downslope flow are an obstacle in determining the environmental and economical impacts of a region due to the affects on transportation management, land use planning, and air pollution. Previous studies observed downslope flow in various climates, but are generally focused on small scale slopes limiting understanding of downslope flow at the regional scale (~100 km). Boundary layer observations taken during the METCRAX field study in October of 2006 in northern Arizona revealed the frequent presence of a regional scale downslope flow. Data from a sodar, a radar wind profiler, several surface stations, and frequent high-resolution rawinsonde soundings characterize the downslope flow and its relation to the ambient environment. The data analyses are augmented by high-resolution mesoscale numerical modeling. The depth of this downslope flow is between 100 and 250 m with a peak speed of 4-6 ms^{-1} usually within the lowest 50 m above ground. Opposing ambient winds lead to a longer evening transition period, shallower slope flows, and a smaller horizontal extent as compared to supporting ambient winds. A simple analytical solution appears to agree fairly well with the observed downslope wind speed, but the classic Prandtl solution for maximum downslope wind speed fails to match the observations. The properties of the flow appear to be insensitive to changes in soil moisture, land cover, and surface roughness length. Contribution to the low-level wind maximum by an inertial oscillation at night is also found to be insignificant.

To my loving wife Katie, sister, and parents

who gave me the courage, confidence, and education

I needed to accomplish my goal

ACKNOWLEDGMENTS

I would like to thank my advisor Dr. Shiyuan Zhong for her advice, teachings, and review of this thesis; Wenqing Yao for assistance with figures; Dr. Julie Winkler, Dr. Jeff Andresen, and Dr. David Whiteman for their constructive edits; Dr. Nathan Moore for his assistance with RAMS; and Steve Oncley, Gordon Maclean, and the NCAR ISS and ISFF staffs for providing equipment, field support, and data processing during the experiment. A special thanks to my fellow graduate friends, especially Lesley and Brad, and my extended family whose inspiration guided me over the past two years. This research is supported by the U.S. National Science Foundation Physical and Dynamic Meteorology Division (S. Nelson, Program Manager) through Grants 0646206.

TABLE OF CONTENTS

LIST OF TABLES

LIST OF FIGURES

LIST OF EQUATIONS

KEY TO SYMBOLS AND ABBREVIATIONS

Acronyms

PBL	- Planetary Boundary Layer
CBL	- Convective Boundary Layer
LLJ	- Low-Level Jet
CFL	- Courant-Friedrichs-Lewy
RAMS	- Regional Atmospheric Modeling System
METCRAX	- Meteor Crater Experiment
NCAR	- National Center for Atmospheric Research
ISS	- Integrated Sounding System
IOP	- Intensive Observational Periods
NARR	- North American Regional Reanalysis
RASS	- Radio Acoustic Sounding System
AGL	- Above Ground Level
MST	- Mountain Standard Time
NCEP	- National Center for Environmental Prediction
NAM	- North American Model
TKE	- Turbulent Kinetic Energy

Symbols

W	- ageostrophic wind component
W_o	- initial ageostrophic component
V(t)	- actual wind vector
V_o	- actual wind
Vgs	- geostrophic wind vector
$\Delta\theta_{sfc}$	- surface potential temperature deficit
θ_0	- ambient potential temperature
α	- slope angle
g	- acceleration due to gravity
N	- Brunt- Väisälä frequency
K_h	- eddy diffusivity of heat
K_m	- eddy diffusivity of momentum
ι	- vertical length of the downslope flow
z_{max}	- height of the downslope wind maximum
u_{max}	- downslope maximum wind speed
h	- downslope flow depth
$\tau_0 - \tau_h$	- turbulent stress divergence across the slope layer
C_D	- surface drag coefficient
k	- frictional force due to momentum exchange
F	- Froude number
z_o	- surface roughness

Chapter I – Introduction

Mountainous terrain covers almost one fifth of the Earth's land surface and is home to about 10 percent of the world's population (Beniston, 1997). Climate within mountainous regions is crucial not only to those living atop mountains, but also to those in adjacent lowlands that are impacted by various mountain circulations. Mountain environments also house many different animal and plant species due to the diversity of the climate, resulting primarily from differences in altitude and topographic shading. Climatological studies within these regions have examined each of these factors in varying detail, ranging from simple observations to more advanced energy budget analysis utilizing complicated numerical models.

Early studies of mountain climates were limited by the quality and quantity of meteorological observations due to the harsh conditions and remote locations which deterred nations from investing resources (Barry, 1992). Köppen's (1918) classification of climate zones is a prime example of these limitations within mountainous areas as sparse precipitation and temperature data made for a general classification of highland climates for only the largest mountain ranges. As the number of observations improved, investigations of the physical forces behind Köppen's climate zones increased, leading to better understanding of the climate system at a finer scale (Terjung, 1976). Through the help of advancing computer technology, climate research is now studying atmospheric phenomena at a resolution of only a few meters (Soler et al., 2002). This enhanced detail has enlightened climatologists of the importance of boundary layer circulations, primarily around complex topography, where varying topographic relief can alter characteristics of the surface circulations.

The Planetary Boundary Layer (PBL), as defined by Holton (2004), is the "portion of the atmosphere in which the flow field is strongly influenced directly by interaction with the surface of the earth." Within this layer, which on average is within 1 km of the Earth's surface, turbulent motions caused by the friction of the Earth and eddies created by uneven surface heating dominate atmospheric circulation. This becomes amplified over areas of high terrain relief and high altitudes. A unique feature within mountain boundary layers are slope flow circulations. These thermally driven flows are typically seen around mountain areas during quiescent synoptic conditions, which enable the circulation to develop near the surface. More on the characteristics of slope flows is offered in Chapter II, but observations of these thermally driven circulations consistently show a wind maximum near the surface directed upslope during the day and downslope at night. These slope flows, specifically downslope flow, as the effects of upslope flow are limited by external forcing caused by solar heating, are now being investigated as environmental and economical risk factors.

Smith et al. (1997) has pointed to slope flows as a major obstacle to transportation, land use planning, and air pollution management within mountain regions. Most of the concern centers on the circulation's proximity to the surface and frequency of their occurrences; the western United States, for example, is dominated by high pressure ridging more than 70% of the summer and fall seasons (Wang and Angell, 1999), favoring the formation of terrain-induced slope circulations. These circulations can be a serious problem for metropolitan areas and industrial regions which emit high levels of nitrous oxide and other harmful gases. Over flat surfaces these emissions are advected a large distance downwind while being dispersed by turbulence and convection, but within

basins or mountain environments downslope flow confines these harmful particles near the surface and concentrates them over the same areas each night. A particular problem was observed over Salt Lake City, UT, where a thermally driven downslope flow was correlated with fluctuations of aerosol particles less than 10 microns in diameter (Alexandorva et al., 2003). High ozone concentrations in Mexico City were also found to be a result of nighttime downslope flow, where high levels of pollutants would drain towards urban areas (Raga et al., 1999).

Downslope flow may also impact emergency planning or geographically sensitive sciences. The Chinese government examined the observed downslope flow around a nuclear power plant for its potential role in nuclear fallout dispersion (Sang et al., 1999). Ecologists are beginning to take notice of the effect of downslope flow as well. Insect migration is a major concern for mountainous regions in malaria troubled Africa, and understanding downslope flow can aid in tracking small insects (Burt and Pedgley, 1997). Along with the negative consequences of downslope flow, enhanced knowledge of the circulation has introduced new efficient methods for monitoring the ecosystem. Pypker et al. (2007) utilized the high climatological frequency of downslope flows within a region as a cost effective means of monitoring CO_2 concentrations as air parcels exit the base of the slope. This method improved efficiency of observations, but was dependent on the varying characteristics of the downslope flow. Continued research and understanding of downslope flow circulations will undoubtedly enhance understanding of these positive and negative impacts.

The main objective of this thesis is to further understanding of the main characteristics and driving forces behind downslope flows, particularly over isolated

slopes at a larger scale. This is achieved through a detailed survey of historical knowledge and current research relating to downslope flows in Chapter II. A journal article accepted by the *Journal of Geophysical Research – Atmospheres* presents a thorough investigation of observations and numerical sensitivity studies of a downslope flow in northern Arizona in Chapter III. Extended conclusions from the study in northern Arizona are offered in Chapter IV, which is followed by appendices of supplemental information of model parameterization and observations of downslope flows. Images in this thesis are presented in color.

Chapter II – Literature Survey

Many terms have been used to describe downslope flow and its characteristics over recent history. It was referred to by first observers as a 'mountain breeze,' where winds drain down from a mountain peak to the valley floor (Atkinson, 1981; Poulos, 1996). Tower (1903) provided one of the first recorded accounts of these mountain winds, observing them within several valleys in the northern Colorado Rockies. Like many early observers, Tower (1903) generally applied the term 'mountain breeze' to describe a wide range of nocturnal circulations over complex terrain, including both a downslope flow along the valley sidewalls and a drainage flow from the valley to the adjacent plain. Soon the term 'mountain breeze' became more associated with describing the latter circulation, and a new term 'katabatic flow' was used to describe nocturnal slope winds along an isolated slope (Atkinson, 1981). This term was appropriate because of the Greek meaning "downward moving beyond," which describes an air parcel's migration down the slope (Poulos, 1996). While 'katabatic flow' is a general definition representative of all downslope flows, it has recently become more associated with nocturnal slope winds observed over ice covered polar regions (Yu et al., 2007; Zammett and Fowler, 2007, etc.). Despite representing the same physical processes, investigators have used the more fluvial term of 'downslope flow' to represent nocturnal slope winds outside the polar regions (Frye and Chen, 2001; Whiteman and Zhong, 2008).

Early accounts of downslope flow correctly hypothesized that the 'mountain breeze' is a result of radiation loss along the surface of the sloping terrain (Tower, 1903). Downslope flow occurs as cooler air near the sloping surface increases the horizontal

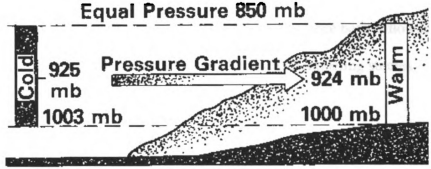

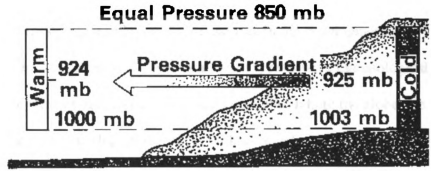

Figure 2.1 Illustration of the thermal imbalance between the slope and free atmosphere increasing the pressure gradient force. (Adapted from Hawkes 1947 and Whiteman 1990)

pressure gradient between the slope the adjacent free atmosphere over lower terrain due to temperature difference (Fig. 2.1). Winds then accelerate from the slope towards the free air, where gravity forces the dense flow to follow the sloping surface. An analysis of the physical mechanisms behind downslope flow was offered by Jeffreys (1922) in his famous work that classified all major winds. Downslope flow was considered antitriptic due to the typically small vertical and horizontal scale enabling the Coriolis effect to be

neglected, leaving the pressure-gradient force balanced mostly by surface friction. Jeffreys' early study provided initial understanding of the important mechanisms and characteristics associated with downslope flow, which has since been followed by observational analysis, analytical solutions, and numerical modeling studies.

a. Characteristics of downslope flows

1. Climatology

Downslope flow has been observed in several different climates, including the Arctic (Renfrew and Anderson, 2006), the mid-latitudes (Horst and Doran, 1986; Doran et al., 2002; Haiden and Whiteman, 2005), and the Mediterranean (Martinez et al., 2006). Climate within these regions plays a significant role in the development and characteristics of downslope flow. Atkinson (1981) presented a climatological study of nocturnal slope winds utilizing various observations throughout the globe. He found that a high frequency of downslope flows occur within the subtropical and polar regions during the winter season. In fact, katabatic winds within the polar regions frequently occur all day during the dark winter months. The mid-latitudes demonstrated the smallest frequency of downslope flow, though Atkinson (1981) admits this may be due to lack of observations. The climatological study also included an analysis of the mean wind speeds observed within downslope flows throughout the world. The survey results found a large range of mean wind speeds from 1 ms^{-1} to 12 ms^{-1}, with the strongest winds occurring within the Antarctic region. This region is often snow covered and lacks atmospheric moisture allowing longwave radiation to escape more efficiently and enhancing the thermal imbalance (Gudiksen et al., 1992). Atkinson's brief survey of latitudinal

variations of downslope flow provided a small glimpse of how the characteristics of downslope flows are dependent on external forces in varying climates.

2. Morning and evening transition

Downslope flow begins in the early evening, typically within a few hours of sunset. Understanding the exact time of the shift towards downslope flow is complicated by several factors (topographic landscape, shadow effects, clouds, ambient atmosphere), but the theoretical transition occurs when the ground temperature first equals the adjacent free air temperature (Atkinson, 1981). During this time, the slope is characterized by calm and variable winds, allowing the effective loss of longwave radiation to continue cooling the slope. Whiteman (1990) uses the sensible heat flux term as an indicator of downslope flow development, stating that the downslope flow begins when the sensible heat flux changes to negative.

Papdopoulos and Helmis (1999) used observations of a nocturnal slope wind at Mt. Hymettos in Greece to describe the transitional period of downslope flow in more detail. While each mountain slope is different, the case study analysis described by Papdopoulos and Helmis (1999) can be applied to most downslope flows. Observations along the mountain suggested the downslope flow initiates at mid-slope, where the mountain shades the slope effectively decreasing net longwave radiation near the surface, creating a weak downslope circulation. The downslope flow then advects down the mountain slope as a micro-front or density current cooling the surface and initiating the surface inversion. As the inversion strengthens and the solar radiation decreases at all positions along the

slope, downslope flow is continuously maintained throughout the night by thermal imbalance.

Timing of the morning transitional period is closely related to the destruction of the surface inversion, as downslope flow is driven by the negative buoyancy provided by the inversion (Papdopoulos and Helmis, 1999). Whiteman (1982) found the breakup of the morning inversion along a slope begins at sunrise and lasts 3.5 to 5.0 hours depending on ambient conditions and the complexity of the environment. Within wide valleys, the upward growth of the convective boundary layer (CBL) caused by surface heating reaches the top of the inversion, inducing atmospheric mixing (Fig. 2.2a). Over snow covered slopes, the amount of solar radiation at the surface is significantly decreased, limiting the ability of the CBL to grow. Thus the inversion is destroyed by subsidence at the top of the nocturnal inversion as it descends towards the surface (Fig. 2.2b). The final method of inversion destruction, and most common, involves a combination of warming of the CBL and descent of the inversion through subsidence (Fig. 2.2c). Each of these patterns of inversion breakup may contribute to the morning transition and destruction of the downslope flow.

Papdopoulos and Helmis (1999) also analyzed the morning transition along an isolated slope. Similar to the evening transition, they observed the breakup of the downslope flow to first occur along the middle of the slope, due to a weaker inversion. Destruction of the nocturnal inversion along mid-slope was consistent with Whiteman's (1982) first pattern of breakup (Fig. 2.2a), as a growing CBL initiated upslope flow. Near the base of the slope, where cool air had pooled overnight, destruction of the nocturnal inversion is delayed. The cold pool deters the growth of the CBL, so destruction of the

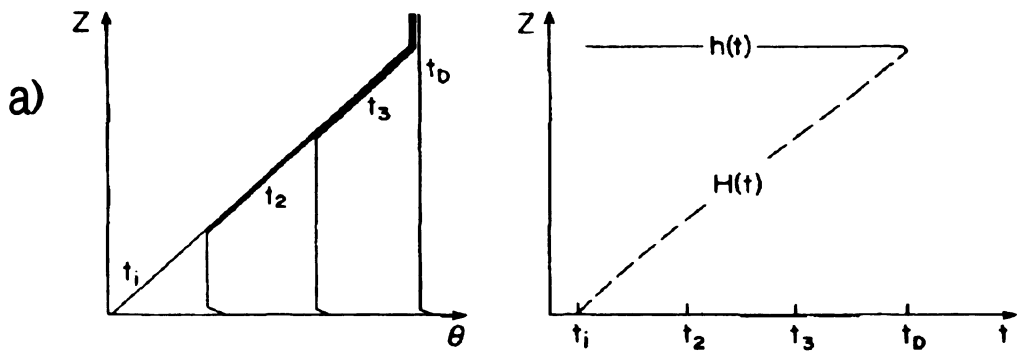

Pattern 1. Growth of CBL.

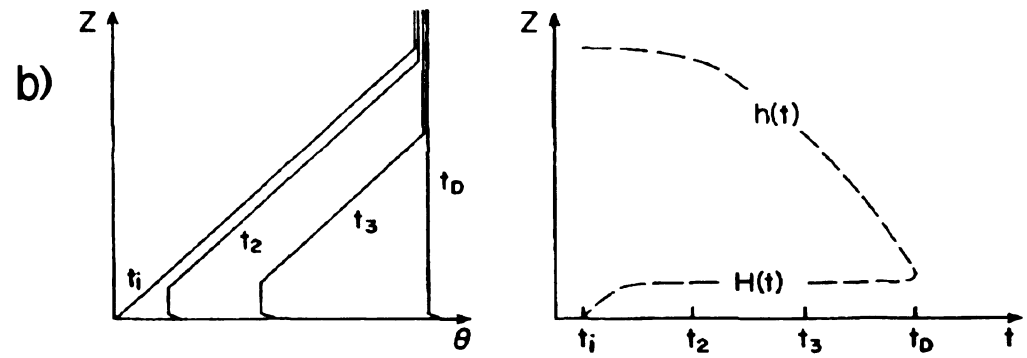

Pattern 2. Descent of inversion top and arrested growth of CBL.

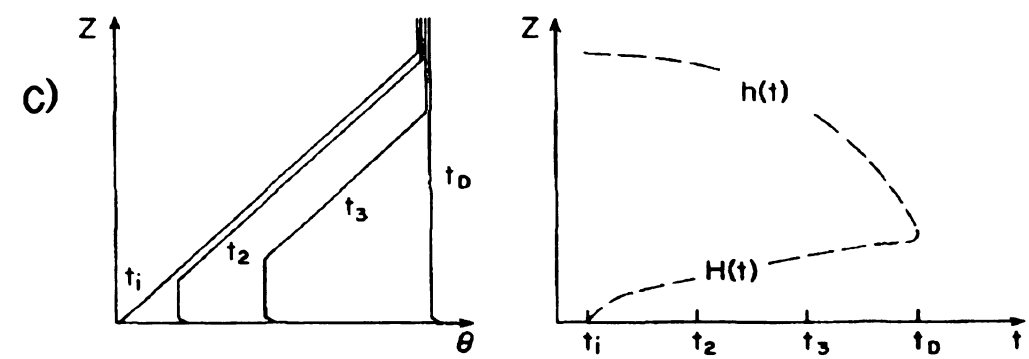

Pattern 3. Descent of inversion top and continuous growth of CBL.

Figure 2.2 Summary of the three different types of inversion breakup observed in Colorado valleys. On the left a vertical profile demonstrates an ideal vertical potential temperature (θ) profile over four time periods (t_i, t_2, t_3, and t_D). On the right the height of the top of the inversion H(t) and the height of the bottom of the inversion h(t) are shown over the four time periods. (a) Pattern 1 is typically seen over wide valleys, (b) pattern 2 occurs along snow covered slopes, and (c) pattern 3 is a combination of the previous patterns and is most common. (Whiteman 1982)

inversion is dependent upon the upslope flow at mid-slope which erodes the top of the inversion through advection (pattern two of Whiteman's inversion breakup).This is just one example of how the morning transition occurs, as Papdopoulos and Helmis (1999) did state the inversion breakup and morning transition are often dependent on the local topography and ambient conditions.

3. Vertical structure of downslope flow

After the evening transition, the downslope flow becomes fully developed and a distinct vertical structure is discernable over the slope. Manins and Sawford (1979b) provided a generalized classification with four vertical layers of a downslope flow over an isolated slope. An idealized sounding is offered in Figure 2.3 illustrating each of the four layers. The skin layer is closest to the sloping surface and is dominated by surface stress reducing the wind speeds. Above the skin layer the surface stress is reduced and the downslope flow is able to reach the maximum wind speed. This layer is typically 40 m in depth and is characterized by strong thermal inversion and little directional shear. Above the main downslope layer is a transitional zone that is variable in depth and involves the interaction between downslope flow and the ambient atmosphere. Finally, the larger scale ambient winds above the transitional layer are unaffected by the downslope flow at about 160 m above the slope. These layer classifications are an idealized conceptualization of a downslope flow and are not representative of every slope. Each layer is influenced by topographic relief and larger scale circulations changing characteristics of the downslope flow.

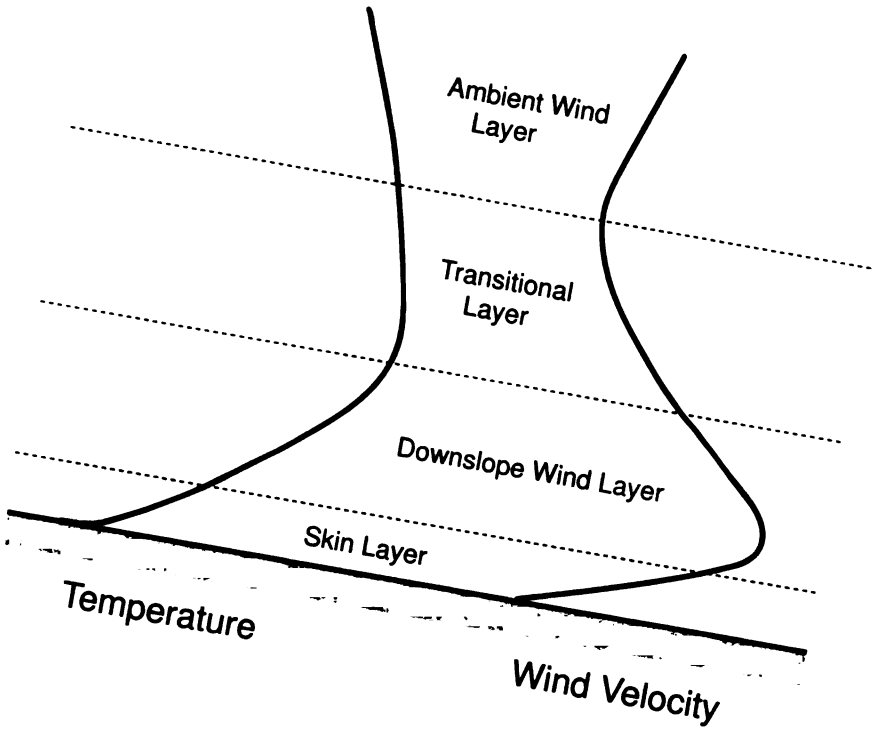

Figure 2.3 An idealized vertical profile of downslope flow based on Manins and Sawford's (1979b) layer classifications.

3.1 Skin layer

As Jeffreys (1920) discovered, the physical mechanisms behind downslope flow are the buoyancy force and surface friction. Papadopoulos et al. (1997) also found this to be the case with surface friction balancing 70 to 80 percent of the buoyancy force driving the downslope flow. The influence of the surface friction is most visible within a few meters of the sloping surface as the wind speeds are noticeably weaker (Fig. 2.3). Without the surface stress, the maximum wind speeds would be located closest to the surface where the pressure gradient force is the strongest (Manins, 1992). Over smooth slopes with little vegetation the effect of surface friction on the downslope flow is less than over steeper more vegetated terrain. In fact, Kondo and Sato (1988) hypothesized that interfacial stress, or the frictional balance caused by the downslope flow's interaction

with the ambient atmosphere, may play a comparable role to surface stress in balancing a thermally-driven downslope flow over smooth terrain. This would limit the impact of the surface friction, effectively shrinking the skin layer and lowering the height of the downslope wind maximum.

3.2 Downslope wind layer

Unlike upslope flows where convection can increase in depth to several hundred meters above ground level, downslope flow is limited to the stable boundary layer near the surface, which is the main concern in dealing with air pollution (Atkinson, 1981). Maximum strength of the downslope flow is within the downslope wind layer because the winds are above the influence of surface friction and the buoyancy term is strongest closest to the slope. The height of the layer is associated with the top of the surface-based inversion, protecting the downslope flow from the stress of the ambient atmosphere allowing winds to reach a maximum strength.

Height of the downslope wind maximum varies with horizontal position along the slope and the time of night. When downslope flow is able to develop in clear conditions, the increase of longwave radiation loss at the surface increases the strength and depth of the inversion. As the stable layer grows, the impact of the surface stress is reduced which allows the height of the downslope wind maximum to increase over time (Whiteman, 1990). Several studies (Horst and Doran, 1986; Whiteman, 1990; Papadopoulos et al., 1996; Poulos et al., 2000) have found the height of the downslope wind maximum to be greater near the base of the slope, because of the pool of cold air that accumulates overnight. The downslope wind maximum is thus forced to rise over the cold pool, increasing the height of the downslope wind maximum and creating a small amount of

vertical motion within the nocturnal inversion (Poulos et al., 2000). Horst and Doran (1986) have observed such changes in the height of the downslope wind maximum over one night, finding the strongest winds between 20 to 50 percent of the nocturnal inversion depth. The height of the downslope wind maximum and nocturnal inversion is also dependent upon the strength and direction of the ambient winds which influence the depth of the transitional layer above.

3.3 Transitional layer

Downslope flow is able to continue above the nocturnal inversion, though the pressure gradient force is reduced due to the weakening thermal gradient. Ambient winds may also impact the downslope flow above the inversion by increasing the interfacial stress caused by turbulent momentum and heat exchange (Manins and Sawford, 1979b). These small scale physical processes are nearly impossible to resolve and predict, thus making it difficult to determine where they occur and how they may affect downslope flow. Attempts to define the depth of observed downslope flow are limited by these constraints, so a general rule of using the depth of the reversal in wind direction from the downslope direction has been applied by Manins and Sawford (1979b) and Poulos et al. (2000). Based on this definition, effects of ambient wind conditions on downslope flow can be investigated within the transitional layer.

Ambient wind direction when observed with downslope flow is not defined by traditional measures, but instead is considered in bidirectional terms as either an opposing or following ambient flow (Arrit and Pielke, 1986; Neff and King, 1987; Mursch-Radlgruber, 1995; Monti et al., 2002). With this distinction, investigators have examined changes of the characteristics of downslope flow caused by both opposing and following

ambient flow. Fitzjarrald (1984) used a one-dimensional model of an idealized downslope flow with opposing ambient winds and found a delay on the timing of the evening transition. His model showed a delay in the onset time of almost eight hours for downslope flows in humid tropical climates. Fitzjarrald attributed this delay to entrainment of the ambient winds near the surface limiting the effectiveness of the slope radiation loss, thus delaying the onset of the downslope flow. Similarly, Neff and King (1987) observed an opposing flow inhibiting the growth of the inversion, delaying the onset, and decreasing the thickness of the downslope flow layer. Entrainment created by the opposing flow increases the depth of the transitional layer, which lowers the height of the downslope flow layer. A closer examination by Arrit and Pielke (1986) showed that the negative shear created by the opposing ambient flow reduces the amount of interfacial stress near the top of the inversion, not influencing the downslope wind speed despite the decrease in height.

A positive shear is created when ambient winds follow the downslope flow direction allowing the exchange of momentum towards the ground (Arrit and Pielke, 1986). This turbulence reduces the strength of the downslope wind maximum which forms immediately after the evening transition, creating longer conditions for the release of longwave radiation and the growth of the nocturnal inversion. As the inversion becomes stronger, the turbulence weakens near the surface and downslope flow is able to develop and grow as well. The strength of the turbulent exchange of momentum impacts the strength of the inversion and is highly dependent on the speed of the ambient winds. Several studies have determined the speed of the ambient winds is the critical factor for the development of downslope flow (Gudiksen et al., 1992; Radlgruber, 1995; Monti et

al., 2002). Whether following or opposing in direction, stronger ambient flow generates shear that deters the development of the inversion at the surface. Without a cold stable airmass downslope flow is not able to develop. Determining a threshold speed of ambient wind conditions that deters the development of downslope flow has been explored by Barr and Orgill (1989). Observations from five nights of downslope flow in variable synoptic conditions provided a mean height of the transition layer based on ambient wind speeds (Fig. 2.4). When ambient wind speeds were higher than 5.0 ms^{-1}, the depth of the downslope flow was noticeably much lower. This general ambient wind speed threshold of 5.0 ms^{-1} was also found by Gudiksen et al. (1992), and is often used for forecasting the development of a downslope flow (Orgill et al., 1992).

3.4 Ambient wind layer

Above the transitional layer is the flow that is driven primarily by large-scale pressure gradient force. This layer often has a more indirect impact upon downslope flow at the surface with the largest effect from overlying precipitation or clouds. Precipitation over a slope can disrupt downslope flow due to an increase in atmospheric moisture (Orgill et al., 1992). Atmospheric water vapor is an excellent absorber of longwave radiation, limiting the effective release of radiation near the surface. Clouds high within the ambient wind layer have a similar effect. As the longwave radiation is emitted from the surface, it can be absorbed by the clouds in the ambient wind layer and released back towards the surface. This limits the ability of the inversion to grow compared to a calm clear night (Derbyshire, 1995). Other large scale systems such as fronts and mountain induced gravity waves also impact the downslope flow due to dynamic pressure effects (Orgill et al., 1992; Poulos et al., 2000). Continued research on the relationship of

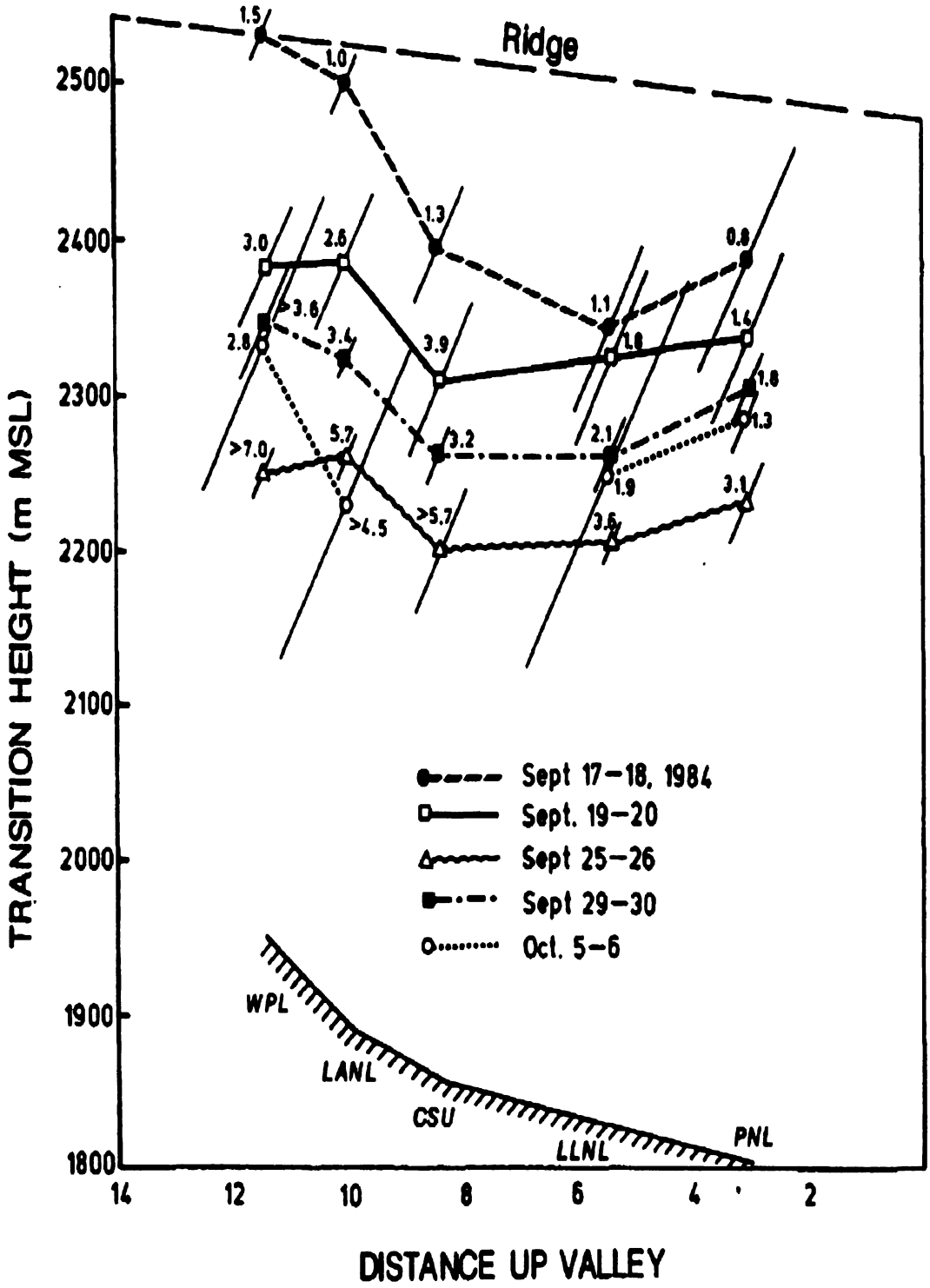

Figure 2.4 Average Bush Creek Valley transitional layer heights + or - one standard deviation (diagonal bar), showing average ridge level wind speeds (ms^{-1}), for five drainage nights during 1984. (Bar and Orgill 1989)

synoptic scale circulations and the downslope flow is necessary.

4. Downslope flow in valleys

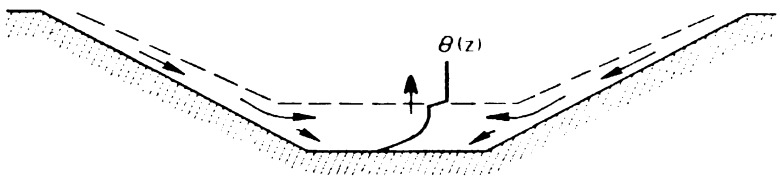

Figure 2.5 Theorized flow of cold pool development and vertical motion within a valley system. Slope flows appear to leave the slope and converge toward the valley center producing compensating rising motion that cool the atmosphere over the valley center. (Whiteman 1990)

Downslope flows may occur on isolated mountain slopes as well as on valley sidewalls. Within a valley system downslope flows are exposed to various thermally driven circulations causing changes to the idealized characterizations described above. Whiteman (1990) attributes the main difference between a valley and an isolated slope to two causes: the increased atmospheric stability within the valley and the ambient winds.

Several investigators have found the nocturnal boundary layer within a valley to be more stable than the atmospheric conditions found around isolated slopes (Whiteman, 1990; Gudiksen et al., 1992; Orgill et al., 1992; Papadopoulos and Helmis, 1999). Within a valley, downslope flows from both sidewalls converge at the center increasing the strength of the cold pool and producing a slight rising motion (Fig. 2.5). As the night progresses, the air on the valley floor continues to pool increasing the stability near the base of the slopes. If stronger ambient winds develop, downslope flow near the top of the valley sidewalls may be disrupted due to the weaker inversion, but the increased stability and topographic shading provided within the valley center maintain the inversion and

downslope flow along the base of the sidewalls (Gudiksen et al., 1992; Orgill et al., 1992).

The cold pool within the center of the valley is influenced by other thermal circulations. As the temperature contrast between the valley and adjacent plain increases, the cold pool begins to drain towards the plain due to the pressure gradient force created by the thermal imbalance (Whiteman, 1990). This so called 'mountain wind' or down-valley jet can create downward mixing of warm air from the inversion, impacting the downslope flow at the base of the valley sidewalls (Pinto et al., 2006). Strong ambient winds and a down-valley jet affecting the base of the sidewalls complicate the characteristics of downslope flow within a valley system. The presence of numerous small-scale circulations is a major reason why valley circulation remains a difficult topic.

b. Inertial Oscillation

The nocturnal low-level jet (LLJ) due to inertial oscillation is in many aspects similar to downslope flows. In fact, early observations (Mahrt et al., 1979) of a nocturnal wind maximum may have been incorrectly identified as a low-level jet resulting from an inertial oscillation, as later analysis identified the winds as a downslope flow (Poulos, 1996). Inertial oscillation was first identified by Blackadar (1957) as a wind maximum which occurs above the nocturnal inversion. The inversion decouples the atmosphere from surface friction which had produced an ageostrophic wind component and constrained the flow during daytime mixing. Without the influence of friction, the winds at the top of the inversion are able to increase towards geostrophic speeds. The large ageostrophic wind component near the surface is then acted on by the Coriolis force,

continuously turning the winds to the right. This creates an oscillating wind vector above the nocturnal inversion with a period based on the Coriolis parameter (Fig. 2.6). Due to the oscillating ageostrophic component, the low-level jet may vary in strength overnight between supergeostrophic or subgeostrophic wind speeds. Zhong et al. (1996) observed low-level jets over the Great Plains, which is believed to play a role in the development of nocturnal convective systems in the region. They found the jet to be a result of inertial oscillation, where the latitude determined the oscillating period of the winds. The inertial oscillation mechanism is a continuing research topic, but is physically different from the mechanisms responsible for downslope flows despite the many common characteristics.

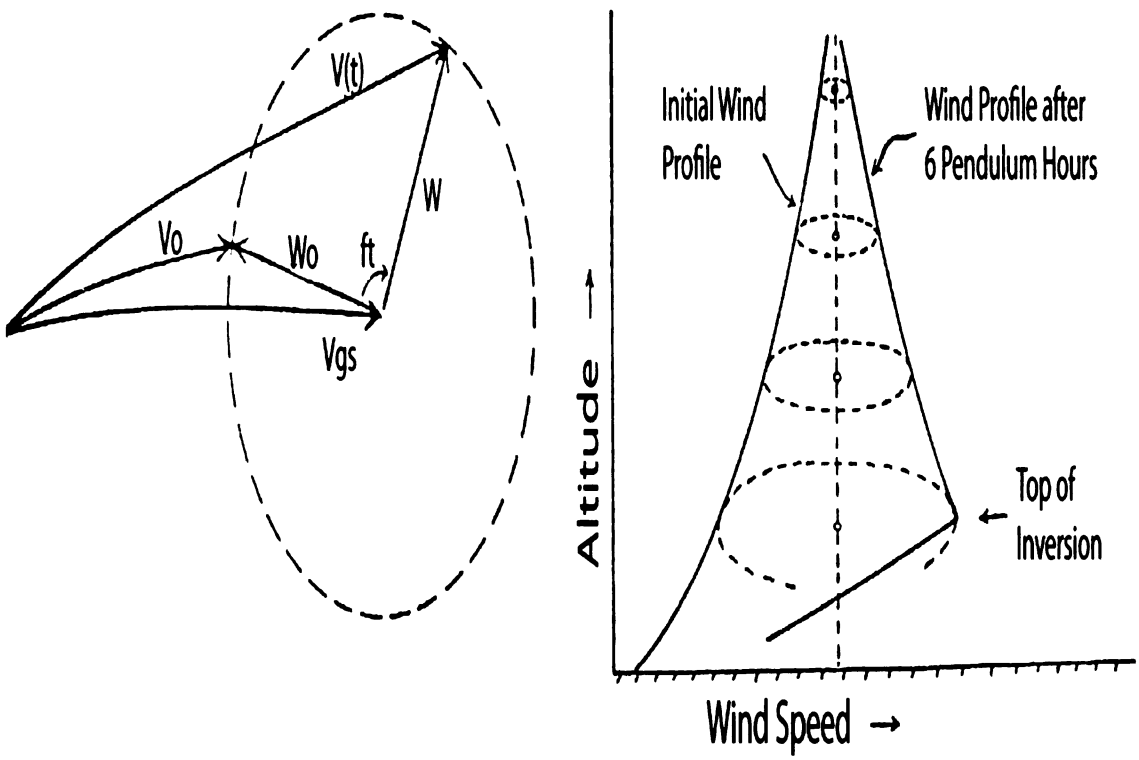

Figure 2.6 (Left) Relation of the ageostrophic wind component (W) and the actual wind vector V(t) to the initial ageostrophic component (W_o) , actual wind (V_o), and the geostrophic wind vector Vgs. (Right) Illustration explaining the evolution of a boundary layer jet profile. (Blackadar 1957)

c. Analytical solutions of downslope flows

Observations have enabled investigators to devise theoretical quantitative models which resolve the basic physical factors behind downslope flow. Beginning with Jeffreys (1922) initial analysis of force balance, downslope flow has been examined using linear analytical models, increasing in complexity as finer scale forces were observed through detailed observations and laboratory experiments (Ball, 1956; Manins and Sawford, 1979a; Kondo and Sato, 1988; Haiden and Whiteman, 2005). Linear models have demonstrated good performance in characterizing downslope flow, but are limited in representing smaller scale features such as turbulence, which is often neglected in idealized analytical solutions (Papadopoulos et al., 1997). Recent trends in studies of downslope flow use observations to validate analytical models and determine the importance of certain parameterizations (Grisogono and Oerlemans, 2001; Haiden and Whiteman, 2005). Basic analytical models of downslope flow are presented within this section to provide a general overview of the important variables utilized to describe downslope flow.

1. Basic equations and assumptions

The main governing equations (conservation of heat, momentum, and mass) have been simplified in theoretical analysis to provide mathematical solutions for downslope flow characteristics. Prandtl (1942) was one of the first to develop a numerical solution for the vertical evolution of slope flows. His analysis assumed equilibrium in both the heat and momentum budgets as a result of stratification near the surface and neglect of the Coriolis parameter due to the small scale of a typical slope flow (Prandtl, 1942).

Neglecting the effect of turbulence does not provide an accurate representation of upslope flow because of the typically strong daytime mixing, but downslope flow is characterized by stable stratification and Prandtl's model has proven to compare reasonably well with observations (Papdopoulos et al., 1997). The model is able to calculate the maximum downslope wind speed,

$$u_{\max} = 0.322 \Delta\theta_{sfc} \sqrt{\frac{g}{\theta_0} \left(\frac{d\theta_0}{dz}\right)^{-1} \frac{K_h}{K_m}} \tag{2.1}$$

and height,

$$z_{\max} = \frac{\pi}{4} l \tag{2.2}$$

where l is equal to the vertical length or depth of the downslope flow,

$$l^4 = \frac{4 K_h K_m}{N^2 \sin^2 \alpha} \tag{2.3}$$

$\Delta\theta_{sfc}$ is the surface potential temperature deficit, θ_0 represents ambient potential temperature, α is the slope angle, g is acceleration due to gravity, N is the Brunt-Väisälä frequency, and K_h, K_m are eddy diffusivities for heat and momentum, respectively. Remarkably, Eq. (2.1) above indicates that the downslope wind maximum strength is independent of the slope angle (α), although the height of the jet is inversely proportional to the slope angle. The height of the maximum downslope wind, as determined by Eq. (2.2), was also found by Prandtl to be approximately a quarter of the total depth of the downslope flow layer. This was tested by Davidson and Rao (1963) who used 214 vertical observations of downslope flow and determined a mean height of the downslope jet at about 0.50 the height of the total depth, which was different from

Prandtl's solution. Despite these inconsistencies, Prandtl's simple analytical downslope flow model continues to be used and improved based on modern observations.

Mahrt (1982) found similar results as Prandtl (1942) using the 'bulk' approach first developed by Ball (1956) and Manins and Sawford (1979a). By using a layer or bulk average of key variables including mass flux, momentum flux, and buoyancy deficit, the bulk approach resolves the larger scale characteristics of downslope flow as opposed to the detailed vertical structure (Haiden and Whiteman, 2005). Mahrt (1982) derived the well-known bulk momentum equation of downslope flow,

$$\frac{\partial}{\partial t}\overline{hu}+\frac{\partial}{\partial x}\overline{hu^2}=\frac{g}{\theta_o}\overline{h\theta}\sin\alpha-\frac{g}{\theta_o}\cos\alpha\frac{\partial}{\partial x}\overline{h^2\theta}+\tau_o-\tau_h \qquad (2.4)$$

where over low-angle slopes hydrostatic equilibrium $g\frac{\theta}{\theta_0}\cos\alpha=-\frac{1}{\rho}\frac{\partial p}{\partial z}$ can be assumed for motion perpendicular to the slope. In Eq. (2.4), u is the downslope wind component, α is the slope angle, h is the downslope flow depth, θ_0 is the horizontally homogeneous basic state potential temperature, θ is the perturbation potential temperature or the heat deficit, and $\tau_0-\tau_h$ is turbulent stress divergence across the slope flow layer, which is typically parameterized by $\tau_0-\tau_h=-(C_D+k)\overline{u}^2$ with C_D being the surface drag coefficient and k the frictional force due to momentum exchange at the interface between the downslope flow layer and the ambient atmosphere (Mahrt, 1982).

Through an extensive scale analysis of the bulk momentum equation, Mahrt (1982) classified downslope flow beyond Jeffreys' (1922) basic antitriptic definition into four ideal solutions for downslope wind speed where the depth is considered constant. Equilibrium flow is the most observed downslope flow, and is the basis for Prandtl's

(1942) ideal solution. Within an equilibrium flow the buoyancy term is assumed to be balanced by turbulent stress, giving a solution for the layer average downslope wind speed,

$$\bar{u} = \sqrt{\frac{g}{\theta_o} h\bar{\theta} \sin\alpha/(C_D + k)} \tag{2.5}$$

A similar solution was found for a shooting flow, where the downslope flow is initiated along a slope with variable topographic relief. The change in topography disrupts equilibrium for a horizontal length scale of

$$L = h/(C_D + k) \tag{2.6}$$

where the return to equilibrium becomes highly dependent upon the drag coefficient C_D of the slope (Mahrt, 1982). A third solution was found when the downslope flow depth is much smaller than the horizontal length of the slope. The advective-gravity flow assumes the downslope flow is driven by the buoyancy term with minimal opposing force by turbulence, both surface friction and interfacial stress. Thus Eq. (2.5) is adjusted to

$$\bar{u} = \sqrt{\frac{g}{\theta_o} \bar{\theta} (\sin\alpha)\mathrm{X}} \tag{2.7}$$

where both the depth (h) and turbulent stress (C_D+k) are neglected, and the mean downslope wind speed increases with X distance down the slope. The final downslope solution offered by Mahrt includes the influence of the Coriolis force. An Ekman-gravity flow is a downslope flow over a large horizontal slope where an air parcel is influenced by katabatic forcing over a sufficient period of time and distance for the impact of the Coriolis force to take effect. These downslope flows are not as well understood due to the lack of observations and the added importance of synoptic scale features. Understanding

the impact of synoptic features on downslope flows has become a challenge of high-resolution numerical models due to the complexity of the relationship and inexpensive cost compared to observations.

d. Numerical modeling of downslope flow

The advancement of computer power has significantly enhanced understanding of atmospheric phenomena through the integration of the basic equations of motion in numerical models. While observational studies of downslope flow have improved our understanding of this phenomenon, the high cost of labor and instrumentation for resolving downslope flow has limited the number of available observations (Pielke et al., 1983). Numerical models have allowed investigators to supplement observations with a higher spatial and temporal resolution of atmospheric parameters to further understand the complex relationships of the external forces surrounding downslope flow. Many of these models began as adaptations to the analytical solutions surveyed above and have since evolved into numerous complex representations of large and small scale features that influence downslope flow.

Thyer (1966) made the first attempt at investigating downslope flow through numerical modeling. He noted that prior to his study downslope flow theories were limited to one or two dimensions and were idealistic linear representation of the downslope flow features, which was unrealistic, especially when simulated over time. This simplicity lead to a more advanced development of a numerical model representation that considered the albedo, specific heat, thermal conductivity, geographical location, topography of the slope, and insolation of the surface calculated

over grid points in three dimensions with the atmospheric parameters integrated over time. A three dimensional model was truly a bold attempt by Thyer due to the limitations of computer power at his time. His model representation of downslope flow was successful, but the model was only able to integrate over four time steps, or two minutes, resolving the initial features of the circulation, but not the evolution of the flow. Poulos (1996) believes Thyer (1966) encountered the Courant-Friedrichs-Lewy (CFL) condition where the grid spacing and timestep of a simulation relate to the maximum allowable wind speed. Still, Thyer's simulations provided a strong base for future development of numerical models and representation of downslope flow.

The initial success of Thyer and others increased research in the 1970s and 1980s in the development of more advanced numerical models. Many of the early higher resolution models were initially designed for wild fire forecasting or long term air quality assessment, and not for specific research of downslope flow features (Ryan, 1977; Pielke et al., 1983). For these real world applications, models required observations of certain atmospheric variables to integrate the initial conditions, which were often limited due to the sparse sampling of observations in complex terrain (Ryan, 1977; Barry, 1992). Investigators were then forced to parameterize several atmospheric features (radiation, ambient wind, sky conditions, lapse rate, etc.) important to resolving downslope flow (Mahrer and Pielke, 1975; Ryan, 1977; Rao and Snodgrass, 1981). As observations and numerical methods improved, the reliance on idealistic atmospheric variables has dwindled, and parameterization of atmospheric phenomena is now limited to sub-grid scale features like cumulus convection and turbulent mixing (Rao and Snodgrass, 1981; Arritt and Pielke, 1986; Nappo and Rao, 1987; Pielke et al., 1992). With the vast

improvement in numerical models, recent studies are now able to test the sensitivity of downslope flow to ambient environmental conditions without the high cost of observations.

1. Idealized numerical simulations

Confidence in numerical models has grown due to the large number of studies that demonstrate good comparison to observations (Bossert and Cotton, 1994a; Castelli et al., 2004). This has prompted several investigators to explore the sensitivity of downslope flow to different parameters through the inexpensive means of numerical modeling. Ye et al., (1989) utilized an idealized numerical model, where the topography and atmospheric parameters are manually initialized to test a specific parameter, and understand the impact of cloud cover on downslope flow development and intensity. They found the depth and strength of the downslope wind maximum were significantly reduced by increased cloud cover and clouds with a low base. Ye et al. (1990) followed with a similar simulation testing the impact of local thermal stabilities on downslope flow. From idealized simulations they concluded that the strength of the downslope flow increased as the local stability increased. While these findings are not groundbreaking, they are excellent examples of how investigators can isolate certain parameters (cloud cover and local stability) to test the sensitivity of downslope flow characteristics using numerical models.

The impact of the sloping terrain has often been tested through idealized models because of the static nature of topography in the real world. Ye et al. (1990) continued their sensitivity analysis of downslope flow by examining the impact of the slope

steepness. They found the strength of the downslope flow increased as slope steepness increased. These findings were later confirmed and expanded upon by Smith and Skyllingstad (2005) who tested the sensitivity of the downslope flow to the shape of the sloping terrain. For concave shaped topography, where a steep upper slope precedes a shallower lower slope, a distinct pattern of strong winds over the upper slope would transition to slower winds at an increased depth over the lower slope. Soil moisture of the sloping topography may also change the dynamics of the downslope flow and was investigated by Banta and Gannon (1995). Two identical idealized simulations were run with varying soil moisture content of 0.25 and 1.0 to represent dry and wet soil respectively. Results indicate a later development and weaker downslope flow over the moist soil due to increased thermal conductivity that allowed warmer soil temperatures to diffuse toward the surface, thus limiting the effect of radiational cooling. Not only are idealized studies important for understanding the sensitivity of downslope flow, they also can identify the importance of certain parameters when modeling within realistic environments.

2. Three-dimensional numerical simulations

Modeling downslope flow within realistic topographic and atmospheric environments is challenging due to the large difference in scale between downslope flow (1~100 km) and synoptic features (300+ km). To adequately represent all of the external and internal forces which may impact the small-scale circulation, a comprehensive dynamic model is required. A model that has been widely used to simulate complex terrain flows including downslope flow is the Regional Atmospheric Modeling System

(RAMS). RAMS was designed to resolve mesoscale features such as downslope flow while also simulating hemispheric scale phenomena by utilizing a two-way interactive grid and message passing interface technology (Pielke et al., 1992; Cotton et al., 2001). RAMS is a non-hydrostatic model, meaning vertical motion is calculated from the vertical equation of motion and small scale features such as tornadoes and turbulence can be resolved (Cotton et al., 2001). Often computational limits restrict the grid spacing required to model turbulence within a downslope flow, so parameterization of sub-grid scale phenomena become very important. RAMS offers a large selection of parameterization schemes designed for improved performance in modeling different atmospheric circulations. A more detailed outline of the parameterization schemes ideal for downslope flow circulations is offered in Appendix A.

The performance of RAMS, particularly within smaller scale simulations, has been tested through comparisons with observations and other high-resolution numerical models. Castelli et al. (2004) compared RAMS output for the Rhine Valley to the TRACT (TRAnsport of pollutants over Complex Terrain) field observations and the hydrostatic ETA model used for operational forecasting. A statistical comparison of the mean variables demonstrated the reliability of both models in forecasting air pollution episodes in fair weather. In contrast, Zhong and Fast (2003) found the RAMS model performed better than the ETA model when compared to observations from the Vertical Transport and Mixing (VTMX) campaign in the Salt Lake Valley. Unlike Castelli et al. (2004), Zhong and Fast (2003) tested the models at a horizontal resolution finer than 1 km enabling the model to resolve the fine-scale boundary layer structure and thermal circulations. While the ETA model consistently underestimated the strength of the

downslope flow, the RAMS model was closer to observations. Despite the better performance by RAMS, errors within the boundary layer temperature structure were still evident. A cold bias from the surface to the top of the valley and a weaker nocturnal inversion with a lower than observed mixed-layer depth often plagued both models. These differences were attributed to sub-grid scale parameterization, specifically resolving turbulence and longwave radiation.

3. Model parameterization and downslope flow

Parameterization of small scale atmospheric features is often required for mesoscale models because the resolution of the model is typically too coarse to realistically resolve the dynamic effects. Representations of longwave radiation flux and turbulent mixing are central to the development and characteristics of downslope flow, but these occur at a sub-grid scale and must be calculated by sometimes oversimplified parameterization schemes (Mahrt, 1998; Pinto et al., 2006). The main source of error in modeling downslope flow creating discrepancies between the model and observations is often a result of these oversimplifications (Hanna and Yang, 2001; Zhong and Fast, 2003).

Turbulence within the surface layer caused by surface friction is difficult to represent because of chaotic and non-linear fluctuations. The parameterization scheme (Louis, 1979) used by RAMS and other mesoscale models is based on the Monin-Obukhov similarity theory, which calculates turbulence within the surface layer using specific parameters. Mahrt (1998) and Pinto (2006) have both found this parameterization to underestimate the turbulence within very stable boundary conditions due to the neglect of non-local turbulence generation, which is compounded over complex terrain and within

downslope flows. An underestimation of turbulence within the surface layer reduces the amount of downward heat flux and increases stabilization and cooling near the surface, which further weakens the turbulence creating a cold bias (Mahrt, 1998). While these errors may obscure comparisons to observations, models are still able to capture the dynamics and characteristics and are considered essential to future understanding of downslope flow (Mahrt, 1998).

Chapter III

An observational and numerical study of a regional scale downslope flow in northern Arizona

Abstract

Boundary layer observations taken during the METCRAX field study in October of 2006 near Winslow in Northern Arizona revealed the frequent presence of a near-surface wind maximum on nights with relatively quiescent synoptic conditions. Data from a sodar, a radar wind profiler, several surface stations, and frequent high-resolution rawinsonde soundings were used to characterize this boundary-layer wind phenomenon and its relation to synoptic conditions and the ambient environment. The data analyses are augmented by high-resolution mesoscale numerical modeling. It is found that the observed nocturnal boundary layer wind maximum is part of a regional-scale downslope flow converging from high terrain of the Colorado Plateau toward the Little Colorado River Valley. The depth of this downslope flow is between 100 and 250 m with a peak speed of 4-6 ms^{-1} occurring usually within the lowest 50 m above ground. Opposing ambient winds lead to a longer evening transition period, shallower slope flows, and a smaller horizontal extent as compared to supporting synoptic winds. A simple analytical solution based on local equilibrium appears to agree fairly well with the observed layer mean downslope wind speed, but the classic Prandtl solution for maximum downslope wind speed fails to match the observations. The properties of the flow appear to be insensitive to changes in soil moisture, land cover, and surface roughness length. The contribution to the low-level wind maximum by inertial oscillation at night is found to be insignificant.

a. Introduction

Terrain-induced local or regional circulations are quite common within the western United States due to the complex topography and the climatologically dry stable conditions of the region. These terrain-induced flows have previously been observed along valley sidewalls (Whiteman, 1982), within basins (Clements et al, 2003), and down mountain slopes (Horst and Doran, 1986). Such observations lead to important discoveries of the characteristics and consequences of downslope flows within all types of topographic environments. Alexandorva et al. (2003) found a striking correlation between the thermally driven slope flow around Salt Lake City, UT and the fluctuation of aerosol particles of diameter less than 10 microns within the city. A similar study in Mexico City found that a nocturnal downslope flow was the main cause of an increase in ozone concentrations within the heavily populated urban area (Raga et al., 1999). Smith et al. (1997) has pointed to the consequences of slope flows as an obstacle in transportation management, land use planning, and air pollution management for determining the environmental and economical impacts upon a region.

Observational studies have shown the characteristics of nocturnal downslope flows vary with slope angle, surface type, ambient winds, and stability. Many investigators have used analytical and numerical models to characterize the structure and evolution of downslope flows and to relate them to the ambient or large scale atmospheric conditions. Prandtl (1942) was one of the first to develop a theoretical model for describing the vertical structure of downslope flow. Prandtl's model gives the height and speed of the downslope jet as a function of the stability, slope angle, and eddy diffusivity. Mahrt (1982) examined the forcing mechanisms behind downslope flows by carefully

evaluating the relative roles of terms in the momentum and thermodynamic equations in a slope following coordinate. These analytical studies have provided a basis for understanding the different observed characteristics of downslope flows in different environments.

Recent studies have focused more on the interaction of downslope flow with dynamical forces at different scales. Idealized numerical simulations have examined the impact of slope shape. Smith and Skyllingstad (2005) found that slopes with a concave shape have a stronger acceleration near the top of the slope which then transitions toward a slower more elevated wind maximum near the base. Uniform slopes, on the other hand, were found to maintain a constant profile of downslope flow along the slope, with stronger accelerations near the base. Other idealized studies have demonstrated the importance of inhomogeneous surface parameters along the slope (Shapiro and Federovich, 2007), and the impact of opposing synoptic scale flow, which affects the depth and strength of the downslope flow (Arritt and Pielke, 1986). Along with these idealized studies, observational and laboratory studies have examined downslope flows over small slopes (Soler et al., 2002), slope discontinuities (Fernando et al, 2006), the impact of downslope flow upon turbulence (Van der Avoird and Duynkerke, 1999; Monti et al., 2002), and the interaction of downslope flows with larger scale phenomena, such as mountain waves (Poulos et al, 2000). While analytical, numerical, and laboratory studies have aided the understanding of downslope flow, field observations have provided a vital validation to theoretical findings. Previous observational studies have been carried out over isolated small-scale slopes only a few kilometers in length (Horst and Doran, 1986; Doran et al, 2002; Haiden and Whiteman, 2005), or at larger scales in the pole regions of

Antarctica (Heinemann and Klein, 2002; Renfrew and Anderson, 2006). This has lead to a limited understanding of downslope flows along larger scale slopes and their interactions with synoptic forcing in mid-latitude regions.

In October 2006, the Meteor Crater Experiment, or METCRAX, was launched to investigate the evolution of the stable boundary layer and the formation of atmospheric seiches in Arizona's Meteor Crater approximately 60 km east southeast of Flagstaff, AZ. Observations were made both inside and outside Meteor Crater to document the interaction of the temperature structure and wind inside the crater with the ambient flows and stability conditions. Observations outside the Meteor Crater suggested frequent near-surface nocturnal wind maxima (4-6 ms^{-1}). These nocturnal near-surface wind maxima were associated with southwesterly winds which, based on the topography at the site, were likely to be downslope flows. Little is known, however, about the horizontal extent or scale of this downslope flow, its evolution with time, its depth, and how its characteristics, such as onset time, peak speed, depth etc., change with synoptic conditions. The METCRAX observations afforded a unique opportunity to answer these questions. This paper combines METCRAX observations with a mesoscale numerical model to characterize this wind phenomenon and its interaction with larger-scale forcing. Section 2 describes in more detail the site and measurements while Section 3 describes the relevant observations. Section 4 introduces numerical model simulations and their results. Finally, conclusions are drawn in section 5.

b. Sites, instrumentation, and measurements

The METCRAX observations were concentrated at the Meteor Crater (35.07 N, 111.03 W) 30 km west of Winslow, Arizona (Fig. 3.1). The site (~1600 m above mean sea level or MSL) is near the Little Colorado River Valley with topography sloping upward to the west-southwest to the higher terrain of the San Francisco Peaks (southeast of Flagstaff and about 2200 m MSL). The approximately 2% slope is more or less homogeneous over a 100 km-long distance (meso-β scale). Vegetation along the sloping terrain changes considerably with elevation. Ponderosa pines and juniper woodlands cover the higher elevations. At lower elevations, an increase in temperature and lack of moisture limit the vegetation to prairie grassland and small desert shrubs. Climate within the region is typical of much of the southwestern United States, which is dominated by subsidence from high pressure ridging more than 70 % of days in both summer and early fall seasons (Wang and Angell, 1999). This climatic pattern of clear, stable conditions makes the region especially susceptible to terrain-induced circulations.

To accurately observe the circulation along the slope, three observational sites were installed at various locations. The first was 5 km north-northwest of Meteor Crater. This site was equipped with the National Center for Atmospheric Research (NCAR)'s Integrated Sounding System (ISS), which consisted of an enhanced surface weather station, a 915-MHz radar wind profiler with Radio Acoustic Sounding System (RASS), and a rawinsonde sounding system. Vaisala RS-92 GPS sondes were launched on seven Intensive Observational Periods (IOPs) during the month-long experiment and the launches would start at 1500 MST and continue until 0900 MST at 3 hourly intervals. This site will hereafter be referred to as the ISS site. A second measurement site

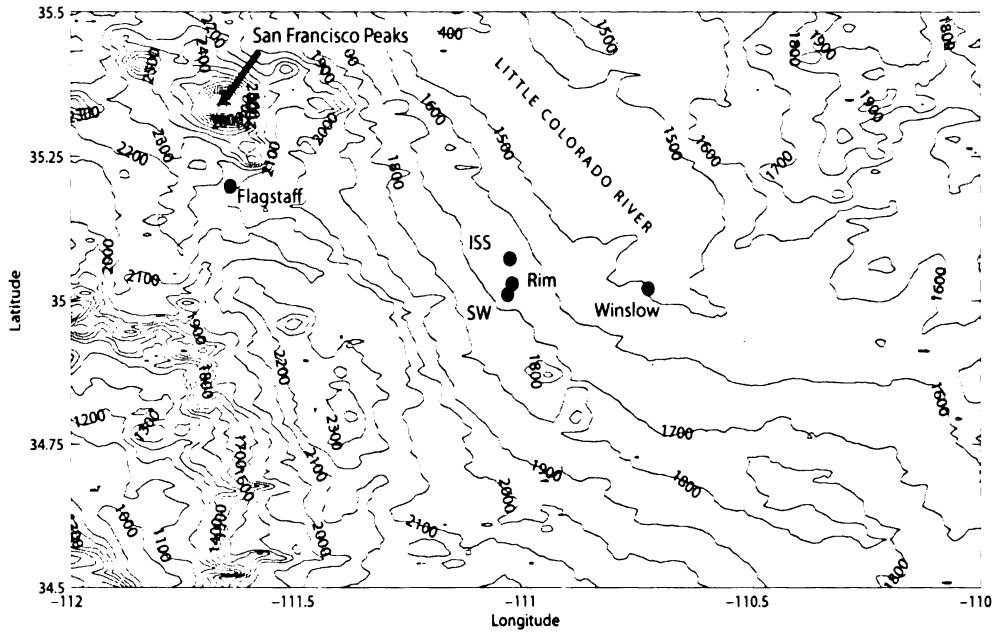

Fig. 3.1 Topographic map of the study region indicating the locations of the observational sites.

(henceforth designated the SW site) was located 2.5 km southwest of Meteor Crater. The site had a 10-m weather tower and a mini Sodar (Metek DSDPA.90-24) with RASS that measured wind speed and direction and temperature continuously from 40 m above ground to about 200 m aloft at 20 m vertical resolution. The third site was on the northwest rim of Meteor Crater (henceforth Rim site) where a 10-m tripod was installed with temperature and humidity sensors (Vaisala 50Y) mounted at two levels (2 m and 10 m) and a R. M. Young propeller vane wind monitor at the 10 m level.

The general behavior of near-surface winds during the month-long experiment can be seen by the wind roses and frequency distribution at the ISS site for the entire month of the experiment in Figures 3.2 and 3.3 for both nighttime and daytime periods. Dominating the nighttime period over fifty percent of the time is a terrain-following southwesterly flow with a frequent speed of 4 to 5 ms^{-1}. The daytime period also shows a

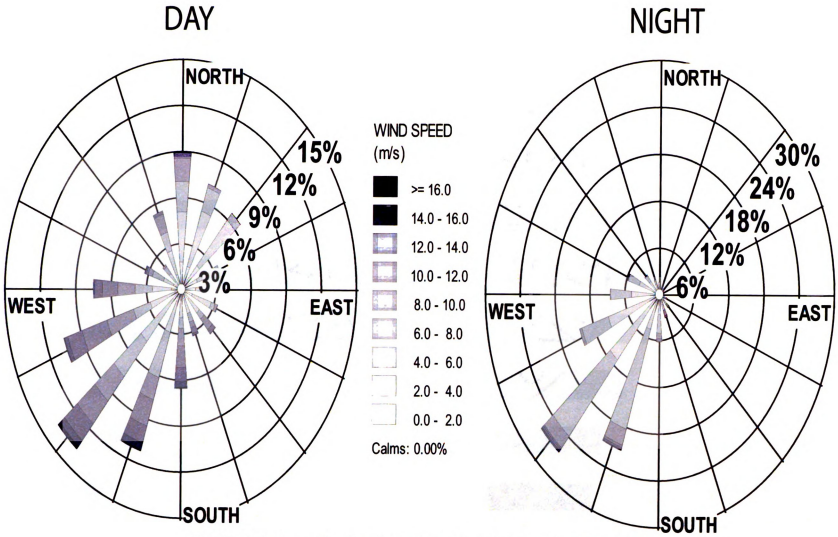

Fig. 3.2 Wind roses for the 10-m wind at the ISS site for October 2006.

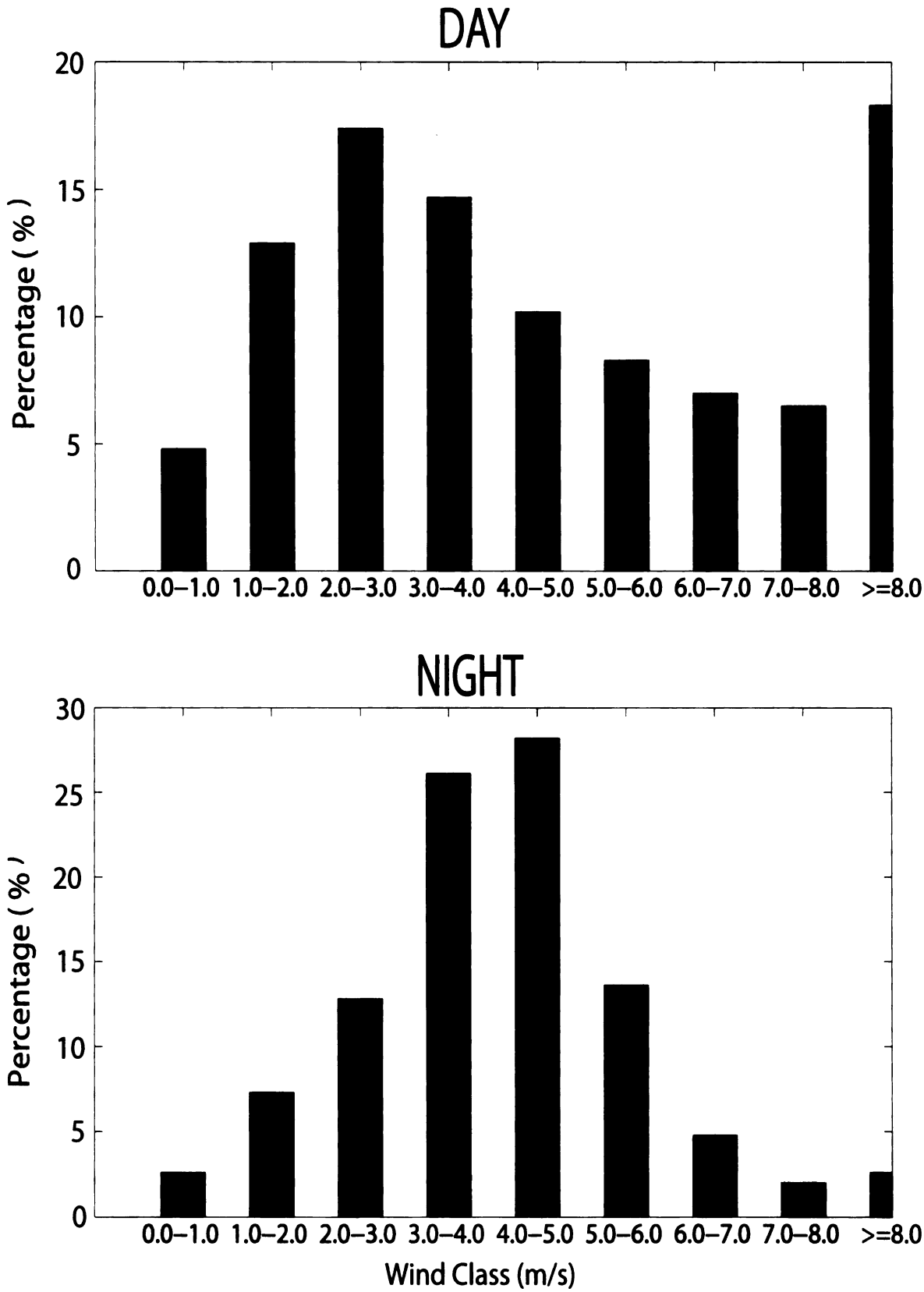

Fig. 3.3 Frequency distributions for the 10-m wind at the ISS site for October 2006.

high frequency from the southwest, though a small peak from the north-northeast possibly exemplifies the effects of a weak upslope component. Strong surface winds exceeding 8 ms^{-1} were caused by downward mixing of strong synoptic winds during daytime.

In this study, surface and upper air observations from three of the seven METCRAX IOPs (IOP 4, 5, 6) are used to investigate the detailed characteristics of the nocturnal downslope flow and its interactions with synoptic conditions. The three IOPs were selected to provide a range of different synoptic wind directions and speeds.

c. Observed downslope flow characteristics

1. Synoptic conditions

The synoptic conditions for the three IOPs are described in this section. IOP 6 (28-29 October) was characterized by weak ambient winds from the southwest, allowing downslope flow to develop over the region. Synoptic conditions were dominated by a ridge of high pressure between a strengthening trough in the Great Plains and a weak cutoff low-pressure system off the coast of California (Fig. 3.4a). This allowed weak winds aloft to develop over northern Arizona through most of the night before giving way the next morning to southerly winds aloft. The weak ambient winds were typical of downslope development throughout the month, though the ambient wind direction was not always from the southwest.

IOP 5 (22-23 October) was characterized by a low-level easterly jet or opposing ambient wind to the southwesterly downslope flow. The easterly flow occurred as a low

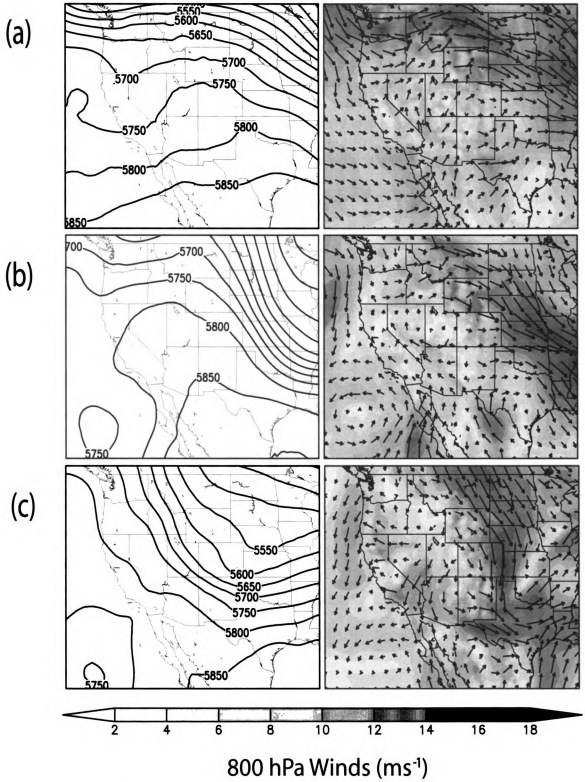

Fig. 3.4 0500 MST 500-hPa geopotential height fields (left) and 800-hPa wind vectors (right) for (a) IOP 6, 29 October, (b) IOP 5, 23 October, and (c) IOP 4, 21 October, based on North American Regional Reanalysis (NARR) data.

level jet between 700 and 900 m above ground level as the cutoff low aloft moved a surface trough into Northern Arizona (Fig. 3.4b). Above the easterly wind layer and similar to IOP 6, the synoptic winds aloft at 500 hPa were relatively weak at 5 to 10 m s^{-1} from the south or southwest (Fig. 3.4b). This easterly low-level jet opposes the southwesterly downslope flow, contributing to the differences in the observed downslope flows between this night and the night of IOP 6 when the mid-level large-scale winds were in the same direction as the downslope flow.

As synoptic conditions aloft strengthened and strong winds began to mix down to the surface, the signatures of terrain-induced circulations became weaker and sometimes disappeared all together. An example of synoptic forcing overpowering local forcing is given in IOP 4 (20-21 October) in Figure 3.4c. On this night, a digging trough developing just to the north of the region brought strong northwesterly winds to the study area. The strong winds began to mix to the surface, which limited the impact of the terrain-induced circulation.

2. Time variations of the downslope flow

Observations taken from the three sites illustrate the downslope flow characteristics (Fig. 3.5). During IOP 6 (Fig. 3.5a), the transition in the evening from northeasterly (i.e., upslope) to southwesterly flow is abrupt and exhibits a continuous anticyclonic turn towards the southwest. Accompanying the hour long transition was a steep drop in temperature of approximately 7 °C, which was a result of near calm wind and clear conditions allowing effective cooling through radiation loss. After the evening transition, surface winds increased to 4 to 5 ms^{-1} and remained steady from the southwest until 0930

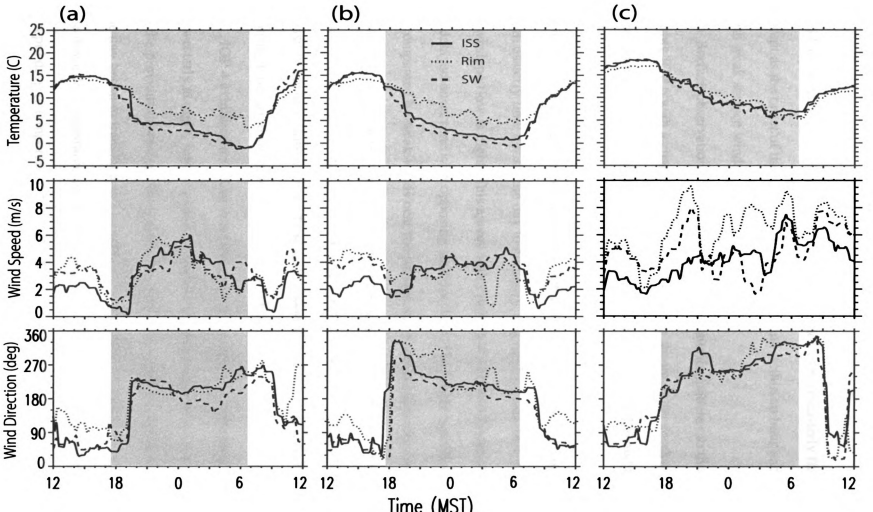

Fig. 3.5 Time series of surface temperature, wind speed, and wind direction at ISS, RIM, and SW sites for (a) IOP 6, 28-29 October, (b) IOP 5, 22-23 October, and (c) IOP 4, 20-21 October. Nighttime period is indicated by the gray shading.

MST the next morning. The morning transition back to northeasterly flow is just as abrupt as the onset of the downslope flow; occurring within an hour and accompanied with weak surface winds.

Surface observations taken from IOP 5 show similar patterns to those observed during IOP 6 with a change in wind direction after sunset to the southwest (Fig. 3.5b). The main difference between the following ambient flow of IOP 6 and the opposing ambient flow of IOP 5 was the evening transition period. The evening transition of IOP 5 took two hours longer than IOP 6 and exhibited a cyclonic shift, turning continuously from easterly flow during the day to northerly, and finally constant as a southwesterly downslope flow at night. This agrees with Fitzjarrald's (1984) theoretical model findings of delayed onset time with opposing ambient flow. The longer transition was also accompanied by weak winds near the surface and a temperature decrease of near 7 °C. Overnight, the surface winds were again characterized by a steady flow from the southwest averaging 4 ms^{-1}. The morning transition back to synoptically driven or possibly upslope flow, exhibited the same characteristics as in IOP 6, though the transition occurred slightly earlier at 0810 MST.

IOP 4 exhibited a shift in wind direction at the surface from easterly during the day to westerly at night, but the characteristics of the transition and flow are not comparable to the previous downslope flow examples (Fig. 3.5c). Instead, the easterly winds during the day began to transition to a southwest direction before sunset. During previous IOPs, the downslope transition was accompanied by a decrease in near-surface wind speed and a rapid drop in temperature, but for IOP 4 the evening transition was characterized by

increasing wind speeds and little temperature change near the surface. As the night progressed, the winds continued to slowly shift more westerly and eventually, after 0300 MST, became northwesterly, which was the same as the ambient flow direction aloft. Surface wind speeds during the period were also stronger and more variable in magnitude ranging from near 4 ms^{-1} to almost 10 ms^{-1}. The strong synoptic forcing is thus driving the surface winds, limiting the impacts of the terrain-induced circulation.

3. The vertical structure of the downslope flow

The vertical structure of the downslope flow was determined from 3-hourly rawinsonde soundings from the ISS site and from one-hour-mean sodar observations at the SW site. Figure 3.6a illustrates the time sequence of the IOP 6 soundings, which were characterized by stable conditions aloft and a strong surface temperature inversion in the lowest 20 to 30 m above ground level (AGL) from 2100 MST on 28 October till 0600 MST the next morning. Accompanying the inversion was a near-surface wind maximum of 4 to 5 ms^{-1}, with wind speed weakening with height up to 200 m AGL. During the morning transition (around 0900 MST) the near-surface wind maximum disappeared as a growing convective boundary layer eroded the overlying temperature inversion and began to exhibit greater influence from larger scale forcing. From the rawinsonde profile, it is difficult to determine the downslope flow layer depth, but the combined hourly sodar and 10-m surface observations taken at the SW site provide a detailed picture of the change in downslope flow depth during the night (Fig. 3.7a). At first, the downslope flow was shallow and weak, but by midnight the depth and strength of the flow was at its peak. Consistent with the 0000 MST sounding, the southwesterly downslope flow extended up

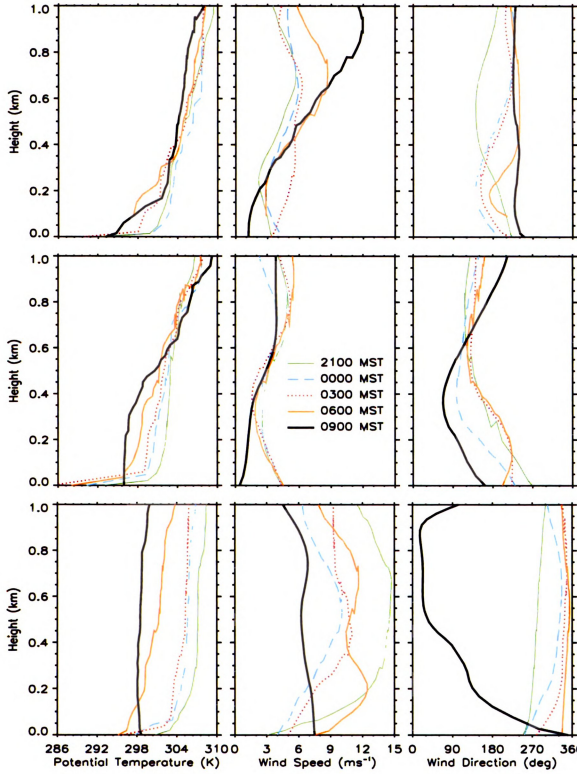

Fig. 3.6 Vertical profiles of potential temperature, wind speed, and wind direction at the ISS site for (a) IOP 6, 28-29 October, (b) IOP 5, 22-23 October, and (c) IOP 4, 20-21 October. Images in this thesis are presented in color.

to 120 m AGL. Later in the night, the depth of the downslope flow began to decrease to below 100 m AGL, and after sunrise was limited to the first 10s of meters AGL. The fluctuation of the depth of the downslope flow throughout the night makes definitive determination of the height of the flow difficult, though a range of 50 to 150 m AGL would best describe the downslope flow depth for IOP 6.

The effect of easterly ambient winds on the downslope flow is illustrated through the series of three-hourly vertical sounding profiles taken during IOP 5 (Fig. 3.6b). The soundings again showed a typical terrain-driven southwesterly flow with maximum speed close to the surface, and a strong inversion of almost 10 K just above the surface. The morning transition around 0900 MST was similar to IOP 6, as the winds near the surface were significantly weaker and increased with height. A closer examination of the sounding and sodar observations for IOP 5 shows a fluctuating depth between 50 and 100 m, with the maximum depth noticeably lower than that in IOP 6 (Fig. 3.7b). Similar to IOP 6, though, is an increase in depth overnight from about 10 m at the beginning of the night, to about 70 m by 0200 MST.

The effects of the strong synoptic northwesterly flow from IOP 4 are seen in the vertical profiles of the 3-hourly soundings (Fig. 3.6c). Unlike the previous IOPs, there was no wind maximum near the surface, but instead the winds increased with height and were predominantly from the northwest. The temperature inversion on this night was also much weaker compared to the other nights. The sodar observations taken from IOP 4 illustrate the strong influence of the synoptic northwest flow, as there is little evidence of terrain-induced drainage flow at any depth throughout the night (Fig. 3.7c).

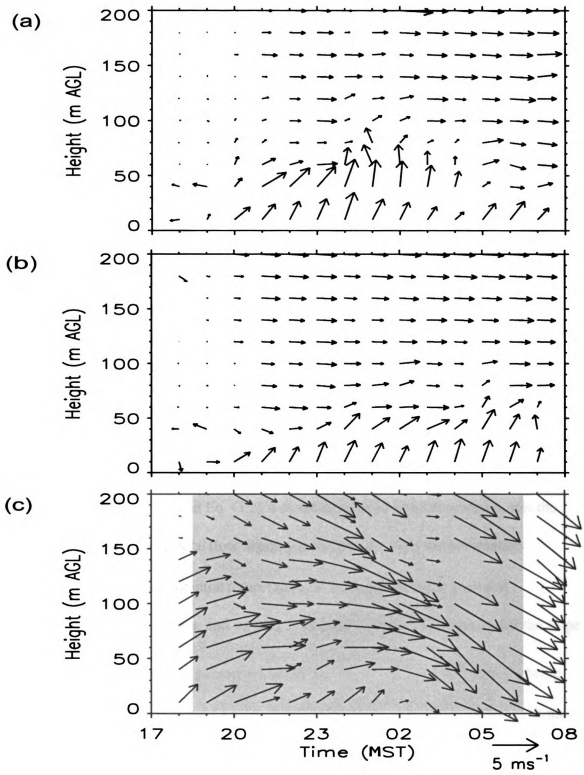

Fig. 3.7 Hourly wind vectors from the Sodar and surface observations at the SW site for (a) IOP 6, 1800 MST 28 Oct. - 0700 MST 29 Oct. (b) IOP 5, 1800 MST 22 Oct. – 0700 MST 23 Oct., and (c) IOP 4, 1800 MST 20 Oct. - 0700 MST 21 Oct. Nighttime period is indicated by the gray shading.

4. Comparison with analytical solutions

A number of analytical solutions have been proposed to describe the characteristics of downslope flows (Mahrt, 1982; Manins and Sawford, 1979; Kondo and Santo, 1988; Nappo and Rao, 1986). Most of these are simplified solutions of the bulk momentum equation for downslope flows

$$\frac{\partial}{\partial t}h\bar{u}+\frac{\partial}{\partial x}h\overline{u^2}=\frac{g}{\theta_o}h\bar{\theta}\sin\alpha-\frac{g}{\theta_o}\cos\alpha\frac{\partial}{\partial x}h^2\bar{\bar{\theta}}+\tau_o-\tau_h \qquad (3.1)$$

Eq. (3.1) is obtained by integrating the momentum equation in a slope-following coordinate system

$$\frac{\partial u}{\partial t}+u\frac{\partial u}{\partial x}+v\frac{\partial u}{\partial y}+w\frac{\partial u}{\partial z}=-\frac{1}{\rho_o}\frac{\partial p}{\partial x}+g\frac{\theta}{\theta_o}\sin\alpha+fv-\frac{\overline{\partial w'u'}}{\partial z} \qquad (3.2)$$

from the ground surface to the top of the slope flow layer with the assumption that hydrostatic equilibrium $g\frac{\theta}{\theta_0}\cos\alpha=-\frac{1}{\rho}\frac{\partial p}{\partial z}$ exists in the direction perpendicular to slope surface. In Eq. (3.1) and Eq. (3.2), u is the downslope wind component, α is the slope angle, h is the downslope flow depth, g is the gravity, θ_0 is the horizontally homogeneous basic state potential temperature, θ is the perturbation potential temperature or the heat deficit, and $\tau_0-\tau_h$ is turbulent stress divergence across the slope flow layer, which is typically parameterized by $\tau_0-\tau_h=-(C_D+k)\bar{u}^2$ with C_D being the surface drag coefficient and k the frictional force due to momentum exchange at the interface between the downslope flow layer and the ambient atmosphere. The overbar in Eq. (3.1) is the layer mean of a variable defined by $\bar{\varphi}=\frac{1}{h}\int_0^h\varphi(z)\,dz$; while the double bar

is the layer mean of an integral from level z in the slope flow layer to the top of the layer,

$$\overline{\overline{\varphi}} = \frac{1}{h^2}\int_0^h dz \int_z^h \varphi(z')dz'.$$

A simple analytical solution for downslope wind speed under the condition of local dynamical equilibrium was proposed by several investigators (Ball, 1956; Mahrt, 1982; Kondo and Sato, 1988). Under local equilibrium, buoyancy is balanced by turbulent stress divergence and Eq. (3.1) is simplified to

$$\frac{g}{\theta_0} h\overline{\theta} \sin\alpha = (C_D + k)\overline{u}^2 \tag{3.3}$$

Solving for layer averaged wind speed gives

$$\overline{u} = \sqrt{\frac{g}{\theta_o} h\overline{\theta} \sin\alpha / (C_D + k)} \tag{3.4}$$

Using nighttime rawinsonde profiles launched from the ISS site during IOPs, the layer-averaged downslope wind speeds are estimated using Eq. (3.4) and the results are compared to those computed directly from the observed downslope wind components (Fig. 3.8). A value of C_D+k = 0.008 is used in the computation to satisfy the assumption for local equilibrium that $F(C_D + k)/\sin\alpha = O(1)$ where F is the Froude number defined as $F = \frac{\overline{u}^2}{g'h}$ with $g' = g\frac{\overline{\theta}}{\theta_0}$ being the reduced gravity indicating the relative importance of transport and Coriolis force terms compared to the buoyancy and thermal wind term. The comparison shows that except for the two disturbed IOPs (IOP 2 and IOP 4) when the ambient winds became relatively strong after midnight, the average downslope wind speeds predicted by the local dynamical equilibrium theory fairly agrees with the

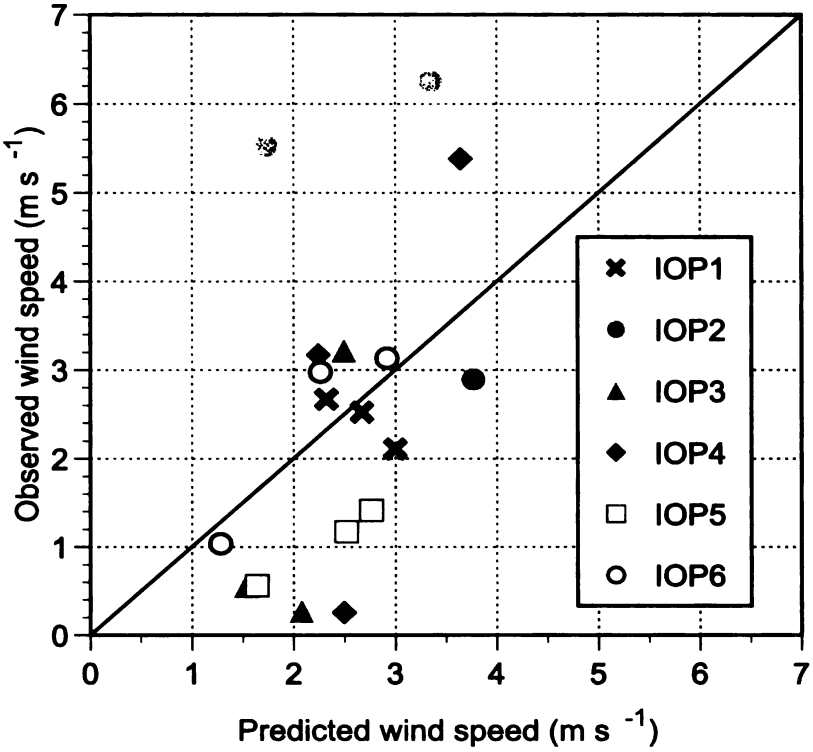

Fig. 3.8 Comparison of observed layer-averaged downslope wind speed by the rawinsonde soundings at the ISS site with those predicted by the analytical equilibrium solution.

observed values. In addition to explaining the differences between IOPs, the analytical solution also captures the variations within IOP 5 and IOP 6, which were the two best IOPs with quiescent synoptic conditions and well-developed downslope flows. The results here indicate that under weak synoptic forcing, the observed downslope flows were governed largely by local equilibrium between the buoyancy force associated with the temperature deficit and turbulent friction. Nocturnal downslope winds observed over a relatively uniform, low-angle slope (~1.6 degree) within the Salt Lake City Valley were also found to be in local equilibrium (Whiteman and Zhong, 2008; Zhong and Whiteman, 2008). Under such circumstances, the simple analytical solution given by Eq. (3.4) may be used to predict the mean downslope wind speed.

The rawinsonde observations were also used to evaluate the well-known Prandtl (1942) equilibrium solution for the maximum wind speed in downslope jets. Prandtl's solution employs eddy diffusivities and a simple thermodynamic equation where diffusion of heat is balanced by temperature advection associated with the basic state stratification. Under such an assumption, the maximum jet speed becomes linearly proportional to the temperature deficit at the surface, i.e.,

$$u_{\max} = 0.322 \Delta\theta_{sfc} \sqrt{\frac{g}{\theta_0} \left(\frac{d\theta_0}{dz}\right)^{-1} \frac{K_h}{K_m}} \qquad (3.5)$$

where $\Delta\theta_{sfc}$ is the surface potential temperature deficit, θ_0 represents ambient potential temperature, and K_h, K_m are eddy diffusivities for heat and momentum. Eq. (3.5) indicates that the speed of the downslope jet increases linearly with increasing temperature deficit at the surface and increases with weakening ambient stratification.

Figure 3.9 shows a comparison of the observed maximum downslope wind speed and the estimated maximum wind speed using the Prandtl solution described by Eq. (3.5) based on the nighttime rawinsonde soundings for IOPs 1-6. The calculation assumes that $K_h = K_m$ in Eq. (3.5). The plot shows relatively large scatter, suggesting that the Prandtl solution is not very accurate in predicting the observed downslope jet. It is interesting to note that the Prandtl solution appears to be in better agreement with observations during the disturbed IOP 4 than with the quiescent IOPs 5 and 6. For IOPs 5 and 6, the analytical values are consistently higher than the observed values. Detailed analyses indicate that the clear sky and near calm conditions during the nights of IOPs 5 and 6 allowed for strong radiational cooling on the ground and the lack of mixing limited the cooling to a very shallow layer. Consequently, the potential temperature deficit

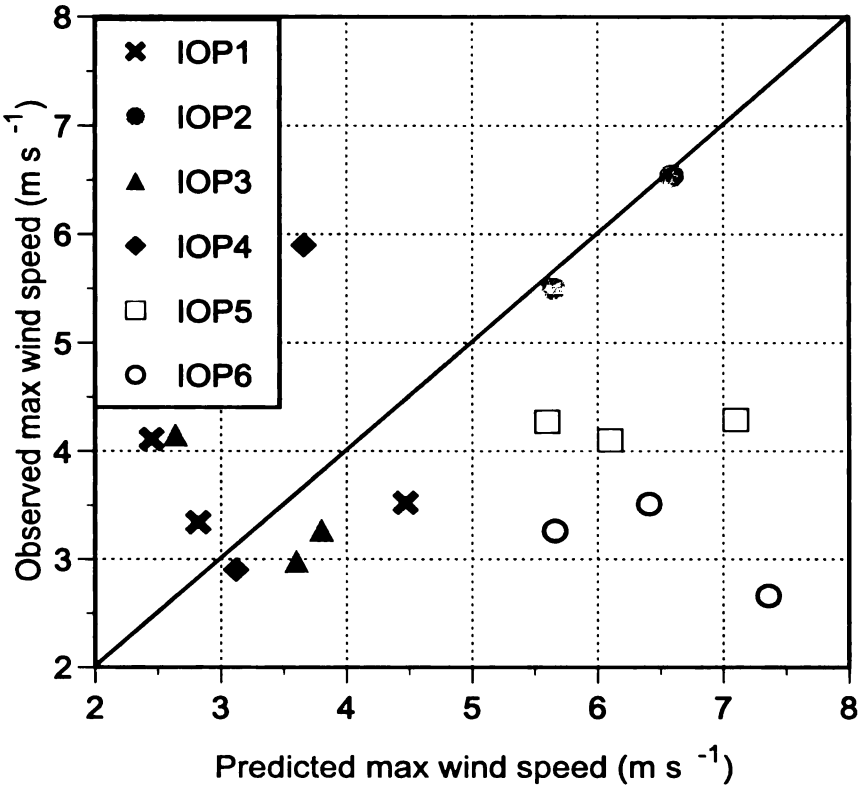

Fig. 3.9 Comparison of observed maximum downslope wind speed observed by the 3-hourly rawinsonde soundings at the ISS site with those predicted by the Prandtl solution.

at the surface $\Delta\theta_{sfc}$ is very large, which leads to a much larger $u_{\max}$ than the actual observed jet maximum. A better agreement may be achieved by replacing the surface potential temperature deficit with an average value across a shallow near-surface layer.

d. Numerical modeling

1. Model setup

The observations captured the temporal variation and the vertical structure of the downslope flows. Unfortunately, the observations were limited to a few closely located sites and were unable to document the spatial extent of this downslope flow. To better examine the extent of the downslope flow beyond the limited observational sites, the

Regional Atmospheric Modeling System (RAMS; Pielke et al., 1992), a non-hydrostatic primitive equation mesoscale model in a terrain-following coordinate system, was employed to simulate these IOPs. Subgrid-scale turbulent diffusion is parameterized using a level-2.5 scheme (Mellor and Yamada, 1982), which allows a turbulent exchange across the jet maximum and a smooth transition between stable and unstable regimes. Turbulent sensible and latent heat fluxes and momentum fluxes in the surface layer are evaluated based on Louis's (1979) formulation. Radiative heating and cooling were represented by the Chen and Cotton (1983) short- and long-wave radiation schemes, which consider the effect of clouds but do not include the effects of aerosols on radiation.

To accurately represent both the synoptic forcing and local forcing within the region, three two-way interactive nested grids with horizontal grid spacing of 32 km, 8 km, and 2 km were used. The outer grid contained most of the western United States and portions of Mexico and the Pacific Ocean, the second grid consisted of most of Arizona and the western part of New Mexico, and finally, the innermost grid covers north-central Arizona including the Little Colorado River Valley and the 3800 m San Francisco Peaks (Fig. 3.10). Each grid had 35 vertical levels, stretching from 20 m near the surface to 1000 m above 10 km. The simulations were initialized at 1200 UTC (0500 MST) using output from the National Center for Environmental Prediction (NCEP)'s North American Model (NAM) and each simulation ran for 31 hours to end at 1900 UTC (1200 MST) the following day.

The goal of the model simulations was to provide a more detailed look at the horizontal and vertical extent of the downslope flow and how its characteristics change from one day to the next. For this reason simulations were performed for the two best

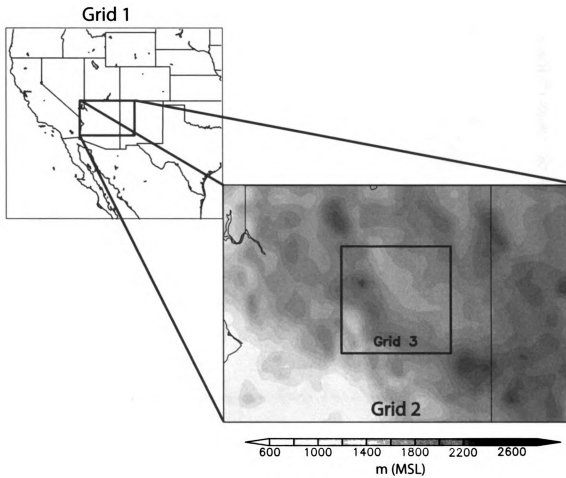

Fig. 3.10 Location of the RAMS grids and the topography in the inner two grids.

IOP nights, IOP 5 (22-23 October) and IOP 6 (28-29 October), when synoptic forcing was weak and the downslope flows were well developed.

2 Simulation results and discussion

The simulated downslope flow characteristics were first compared with the observations for the two IOPs. As shown in Fig. 3.11, the model was able to capture the major observed differences between the two IOPs. For IOP 6, the simulated evening and morning transitions occurred at the same time as observed and the simulated anti-

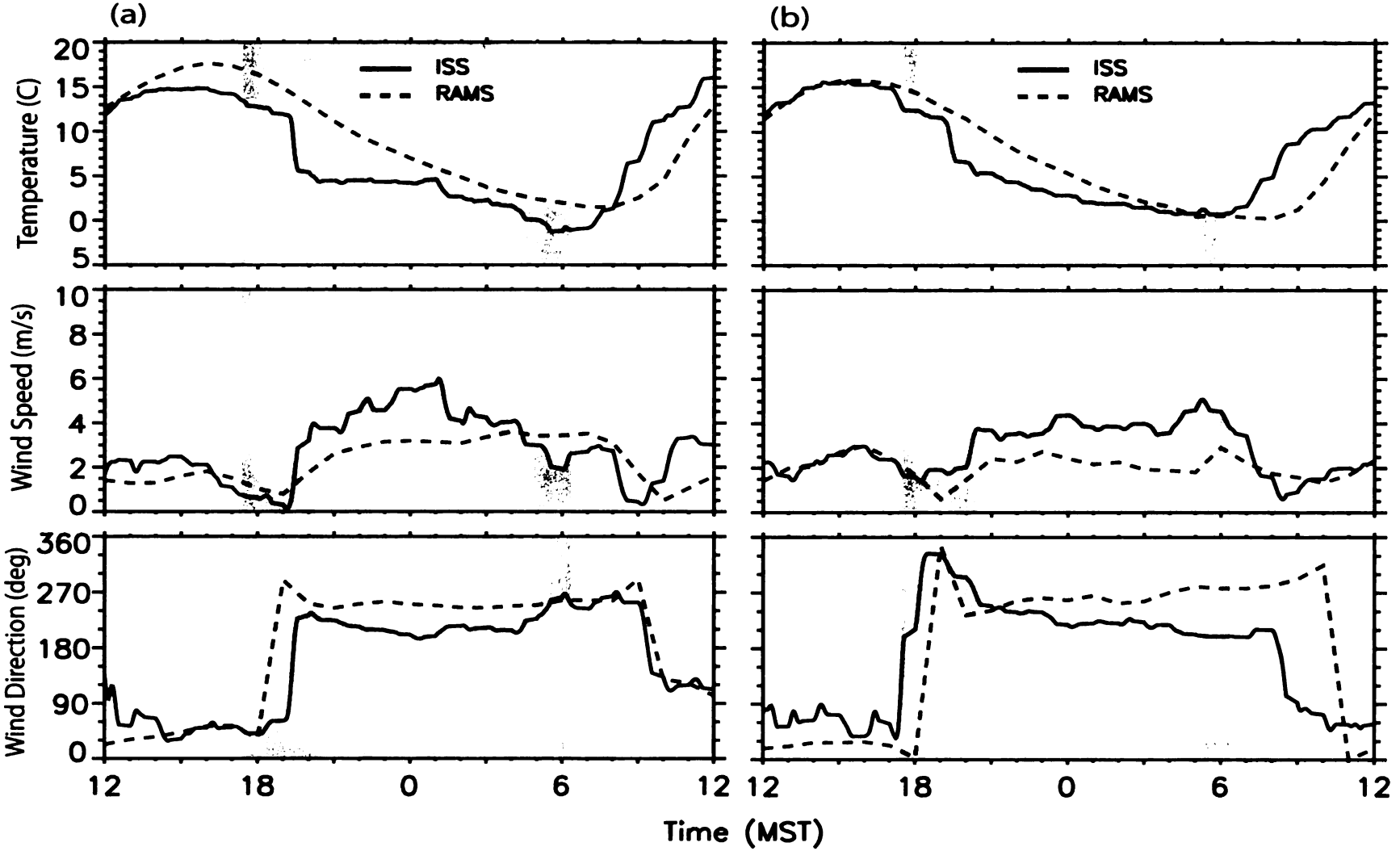

Fig. 3.11 Comparison of simulated and observed surface temperature, wind speed and wind direction at the ISS site for (a) IOP 5, 22-23 Oct. and (b) IOP 6, 28-29 Oct. Nighttime period is indicated by the gray shading.

cyclonic shift also occurred within an hour, as it did in the observations. The evening transition of IOP 5 is also well simulated by the model, as the transitional period to downslope flow takes longer than IOP 6 and exhibits more of a cyclonic shift. The simulations also adequately captured the drop in wind speed at the surface at the time of transition to downslope for both IOPs, though the simulated near surface temperature was warmer than observed. After the transition the simulated wind speeds increased overnight, as observed, but were 1 ms^{-1} less than observations. The discrepancy between the simulated wind direction that was more westerly and the observed direction that was southwesterly may be attributed to the relatively coarse 30' DEM topography data set used by the simulations as well as the relatively coarse model grid resolution.

Soundings taken from the two simulations are comparable to their observed counterparts at the ISS site (Fig. 3.12). The simulated vertical structure and evolution of potential temperature are in good agreement with observations, although the simulated surface-based inversion is weaker in the model. Both the simulation and the observations show a low-level wind maximum with wind speed decreasing with height between 200 and 400 m and increasing above, but the observed wind maximum is near the ground while the simulated winds peak around 50 m above the ground. The discrepancy between the observed and simulated height of the wind maximum can be attributed partially to relatively poor vertical resolution and partially to the tendency of RAMS to produce stronger mixing near the surface during nighttime (Fast and Zhong, 1998; Zhong and Fast, 2003; Berg and Zhong, 2005). The vertical wind direction profiles are quite similar to the observations, though slight variations occur near changes of wind direction. IOP 6 is 100 m higher in representing the weak southerly wind seen at 200 m in the

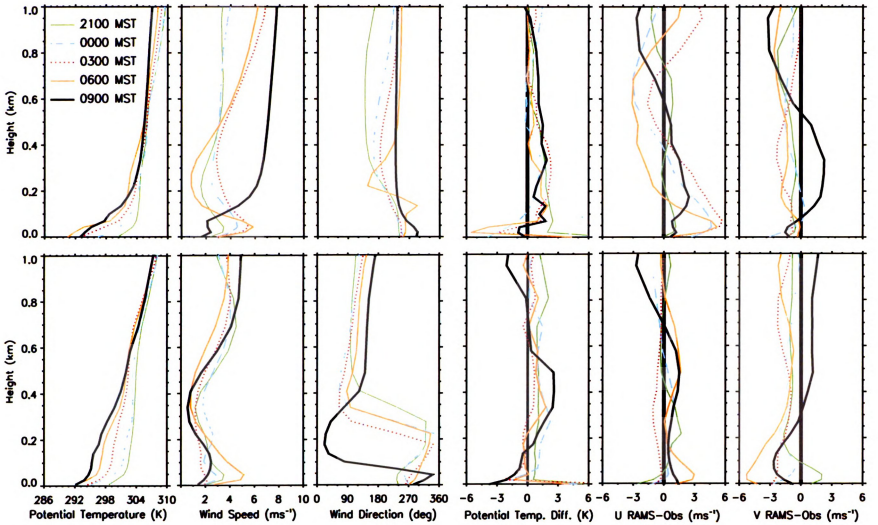

Fig. 3.12 Simulated vertical profiles (left) of potential temperature, wind speed, and wind direction at the ISS site and difference (right) from observations of potential temperature, u wind, and v wind for (a) IOP 6, 28-29 October, (b) IOP 5, 22-23 October

observations. IOP 5 has a better handle on the height of the change in wind direction, but the simulated results show a northern turn in wind direction with height as opposed to the more southerly turn that was actually observed.

Figure 3.13 shows the simulated near-surface wind vectors in the innermost model domain at 0000 MST when the observations indicated fully developed downslope flows for both IOPs. The simulations also exhibit well-developed downslope flows at the observational sites and it is clear that this observed downslope flow is part of regional-scale, diurnally varying terrain-induced circulation that converges from high terrains into the Little Colorado River Valley region at night and diverges out of the valley towards high terrain during daytime (not shown). The downslope flow in IOP 6 is noticeably stronger and extends further into the Little Colorado River Valley than IOP 5, which is hampered by stronger ambient flow and the easterly jet aloft. Also noticeable are the increased wind speeds on the other side of the valley, which may be enhanced by the easterly jet and may play a role in producing a smaller horizontal extent of southwesterly downslope flow for IOP 5.

The simulated u-components on an east-west vertical cross section through the ISS site are shown in Figs. 3.14-3.15 for four different times during the nights of IOPs 5 and 6. These cross sections clearly illustrate the vertical structure and the time variation of the downslope flows. There are significant differences in the vertical and horizontal extent of the downslope flows between IOP 5 and IOP 6, due primarily to the differences in the background wind direction. In the case of IOP 6 where the large-scale winds are west-southwesterly, the westerly downslope winds have a larger horizontal and vertical extent compared to IOP 5 when the mid-level background winds were easterly. The

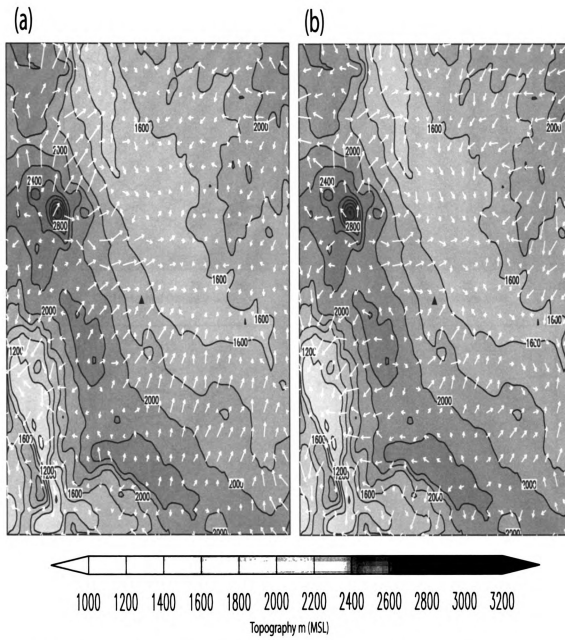

Fig. 3.13 Simulated near-surface wind vectors and topography contours in the innermost grid for (a) IOP 6, 28-29 Oct. (b) IOP 5, 22-23 Oct. The triangle indicates the location of the ISS site.

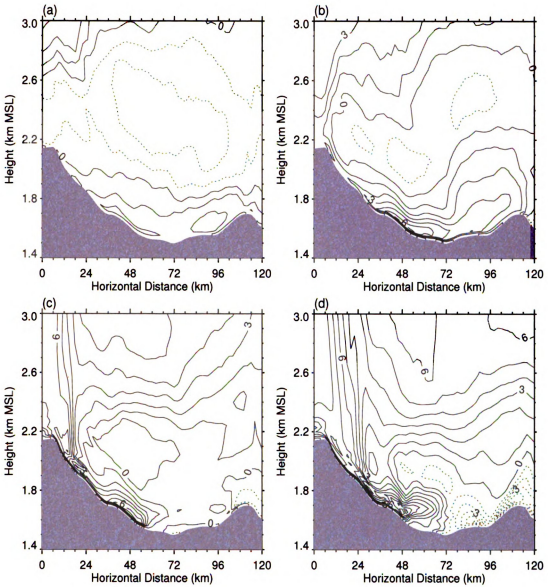

Fig. 3.14 Simulated u wind components on an east-west vertical cross section through the ISS site at (a) 2100 MST, (b) 0000 MST, (c) 0300 MST, and (d) 0600 MST for IOP 6, 28-29 Oct. Solid lines represent positive values and dotted lines represent negative values.

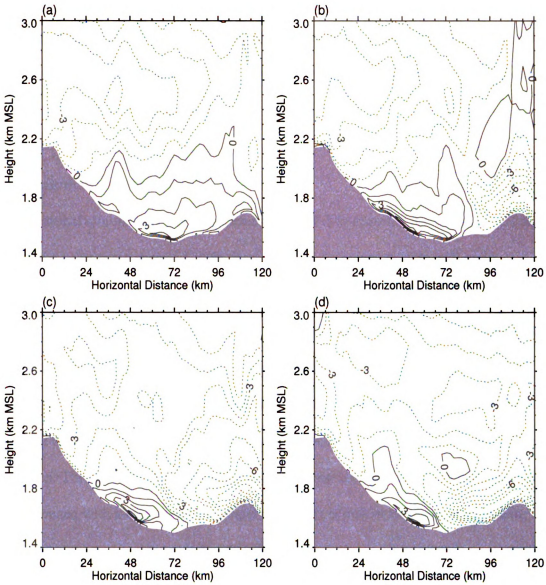

Fig. 3.15 Simulated u wind components on an east-west vertical cross section through the ISS site at (a) 2100 MST, (b) 0000 MST, (c) 0300 MST, and (d) 0600 MST for IOP 5, 22-23 Oct. Solid lines represent positive values and dotted lines represent negative values.

development of the downslope flow on the east side slopes of the Little Colorado River Valley is significantly delayed in IOP 6 and did not occur until early morning. In IOP 5, the easterly background winds allowed the downslope flow on the lower east side slope

to develop at midnight and suppressed the advance of the downslope flows from the steeper west side slope. In addition to the differences in the structure of the winds, the stratification also appears to be stronger in the lower atmosphere over the sloping terrain in IOP 6 than in IOP 5 (not shown).

3. Sensitivity experiments

Additional simulations were performed for IOP 5 to examine the sensitivity of the characteristics of these regional scale downslope flows to several physical and environmental factors. The first factor is soil moisture, which has been shown to impact katabatic flows and is variable in Northern Arizona from seasonal rains (McCumber and Pielke, 1981; Banta and Gannon, 1995). Two additional simulations were performed assuming drier (relative soil moisture 0.1) and wetter (relative soil moisture 0.35) soil compared to the moderate relative soil moisture value (0.2) used in the control simulation. The second factor is land cover. In the control simulation, the land cover is heterogeneous with a mixture of grassland and small shrubs at lower elevations and ponderosa pines and juniper woodlands at higher elevations. Variations in vegetation type or land cover have been found to change the strength of downslope flows (Sun et al., 2006), and so an additional numerical experiment was performed using homogeneous land cover with semi-desert in the middle and inner grids. Potential impact of surface friction on the downslope flow was examined by changing the surface roughness from the control simulation of z_0=0.01 m to z_0=0.05 m. An experiment was designed to investigate the effect of Coriolis force on the current regional-scale (~100 km) downslope flows. Coriolis force is typically neglected in analytical studies, because downslope flows

frequently occur at a local scale (~10 km). In the control simulation, Coriolis force was included throughout the simulation. In the sensitivity run, the Coriolis force was turned off just before sunset at 1800 MST to allow the nighttime phase to develop without the influence of the Coriolis force. One goal of this experiment was to determine to what degree the nocturnal near-surface wind maximum could be attributed to inertial oscillations that produce nocturnal low-level jets.

Figure 3.16 shows time series of near-surface properties at the ISS site for different soil moisture, land cover, surface roughness, and both with and without the Coriolis force. There are noticeable differences in the simulated near-surface temperatures when wet and dry soil moisture values were used, with a larger temperature drop at night in the dry case than in the wet case, as expected. The differences in simulated near surface wind, however, are very small. The downslope winds for each simulation remain 1 ms^{-1} smaller than observations and the morning and evening transition occurred at nearly the same time in all three cases. Figure 3.17 illustrates the impact of soil moisture on the thermodynamics of the region by showing the vertical profile difference between the wet and dry simulations. As to be expected, the main variation between the cases occurs in the strength of the surface inversion, where the dry case is stronger than the wet case. When semi-desert land use is applied to the entire study region, the differences in wind direction are noticeable, but differences in temperature are smaller than those due to soil moisture change. The small temperature change at the ISS site may be because the changes in land use between the sensitivity and the control simulations are mostly over higher elevations; at the ISS site, the land use change is very small. The rougher surface provided little change from the control simulation. Wind speeds throughout the night

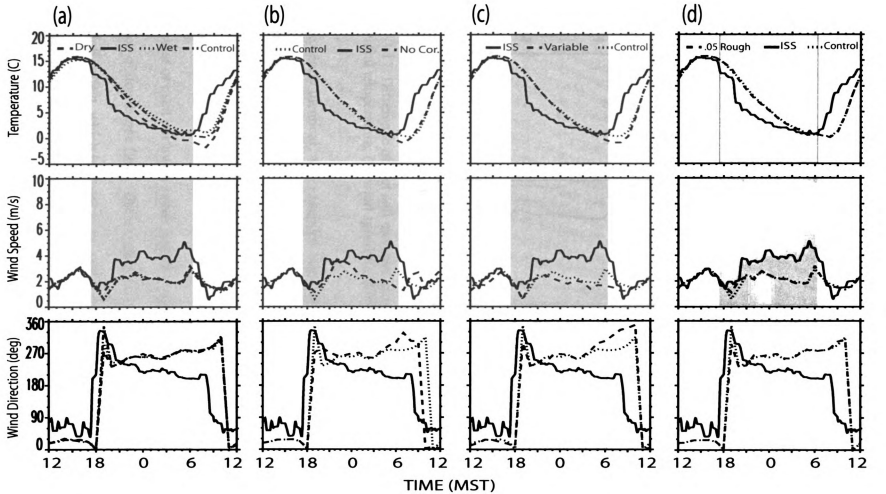

Fig. 3.16 Simulated near surface temperature, wind speed, and direction for simulations with (a) change in soil moisture content, (b) Coriolis and no Coriolis, (c) change in land cover, (d) change in surface roughness for IOP 5 22-23 October. Nighttime period is indicated by the gray shading.

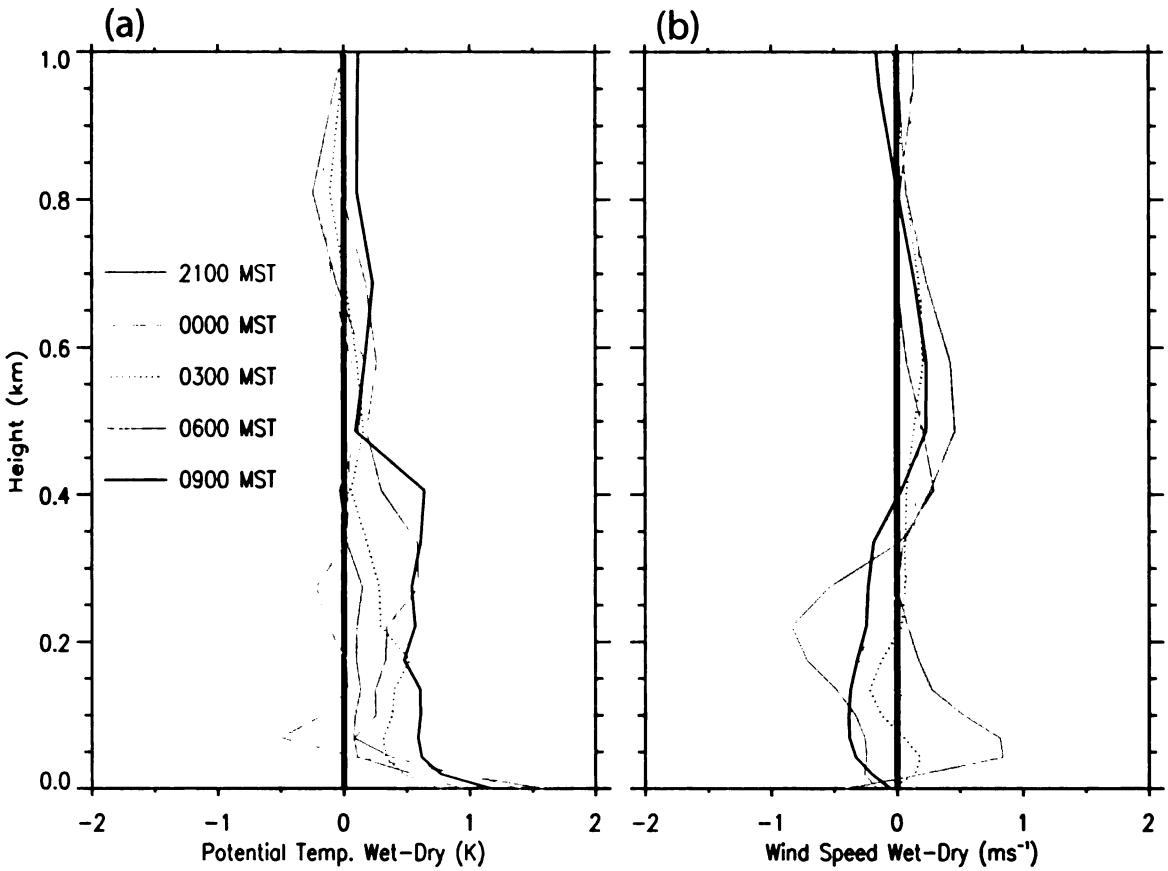

Fig. 3.17 Difference of wet soil moisture case – dry soil moisture case for simulated (a) potential temperature, (b) wind speed for IOP 5 22-23 October. Images

were nearly identical, with exception to the afternoon transition periods, where the winds were slightly lower for the higher roughness simulation. Timing of the two transitional periods remained the same. Without Coriolis force, the downslope wind speeds are noticeably stronger and more variable throughout the nighttime period, and turn more to the west or even northwest rather than the southwestern direction observed during the period of downslope flow. The morning transition occurs one hour earlier without the Coriolis effect, which is closer to the observed transition. While there are more noticeable variations in the coriolis sensitivity study than the other studies, the differences are negligible, further suggesting that the observed low-level wind maximum is primarily a

drainage flow, rather than the a low-level jet due to inertial oscillation of an ageostrophic wind component at the time of decoupling of the layer from the surface friction by the build up of the nocturnal inversion (Blackadar, 1957).

e. Conclusions

Surface observations and frequent, high resolution upper air observations taken during the METCRAX field campaign in northern Arizona approximately 60 km east-southeast of Flagstaff, AZ were analyzed to characterize a regional-scale downslope flow and its relation to synoptic conditions and the ambient environment. The depth of this downslope flow is typically between 100 and 250 m with a peak speed of 4-6 ms^{-1} occurring usually within the lowest 50 m above ground. Varying synoptic wind directions and speeds have large impacts on the downslope flow. Opposing ambient winds lead to longer period of evening transition, a shallower slope flow layer, and a smaller horizontal extent when compared to supporting synoptic winds. A simple analytical solution assuming local equilibrium appears to agree reasonably well with the observed average wind speed across the downslope flow layer, but the Prandtl solution for maximum downslope wind speed exhibits poor agreement with the observed maximum wind speed, especially in the case of quiescent conditions when local radiational cooling produces very large near-surface temperature deficits.

The data analyses were augmented by high-resolution mesoscale numerical simulations using the RAMS model. The model simulations agree reasonably well with the slope flow observations. The simulation results suggest that the observed downslope wind is part of a regional-scale circulation that converges from high terrain of the

Colorado Plateau towards the Little Colorado River Valley at night and diverges out of the river valley towards higher terrain during the day. Sensitivity simulations were performed to examine the effect of soil moisture, land use, surface roughness, and Coriolis force on the properties of the downslope flow in the region. Changes in soil moisture had little impact on simulated downslope wind properties, although relatively large difference in near-surface temperature was produced. The land cover change, which was mostly limited to high elevation, exhibited small effect on downslope wind direction. Surface roughness also exhibited negligible effects, with weaker winds during the afternoon transition of the higher surface roughness (z_0=0.05 m) simulation. Neglecting Coriolis force, as is typically done in idealized studies of small scale slope flows, had a more noticeable effect on the speed, direction, and transition of this regional scale downslope flow, but was still insignificant in the change of characteristics indicating the observations are from a drainage flow.

Chapter IV – Extended Conclusions

A thorough investigation of historical and current research has been offered to identify the important parameters vital to understanding downslope flow. With this knowledge, a detailed observational and numerical modeling study of a downslope flow on a gentle isolated slope at meso-β scale (~100 km) in northern Arizona is presented. The specific objectives of this study were to 1) determine the characteristics of the downslope flow (depths, strengths, evening and morning transition etc.) using special field observations, 2) investigate the influence of the ambient wind conditions on the properties of the flow, 3) evaluate the usefulness of analytical downslope flow models in a realistic environment over a relatively large uniform slope, 4) document the horizontal extension and the three dimensional structure and evolution of the downslope flows using a mesoscale numerical model validated by observations, and 5) understand the sensitivity of the slope flow characteristics to the physical properties of the slope surfaces (e.g., soil moisture, land cover, surface roughness), and to the Coriolis parameter. While the main conclusions are given in Chapter III, further discussion is presented here for increased understanding of the downslope flow sensitivity, the limitations encountered during the study, and possibilities for future research.

a. Additional discussion of the sensitivity simulations

1. Soil moisture

The model simulation testing the sensitivity of the soil moisture found a greater affect on the strength of the surface inversion than the characteristics of the downslope flow. This is in contrast to an idealized study by Banta and Gannon (1995) that found a

delayed onset of the downslope flow and a weaker maximum wind speed over moist soil surfaces due to increased thermal conductivity. Figure 4.1 shows the vertical cross section of the differences in potential temperature between the wet (0.35) and dry (0.10) relative soil moisture cases. The slightly warmer (1 to 2 K) temperatures near the base of the slope are most likely a result of increased thermal conductivity, specifically over the

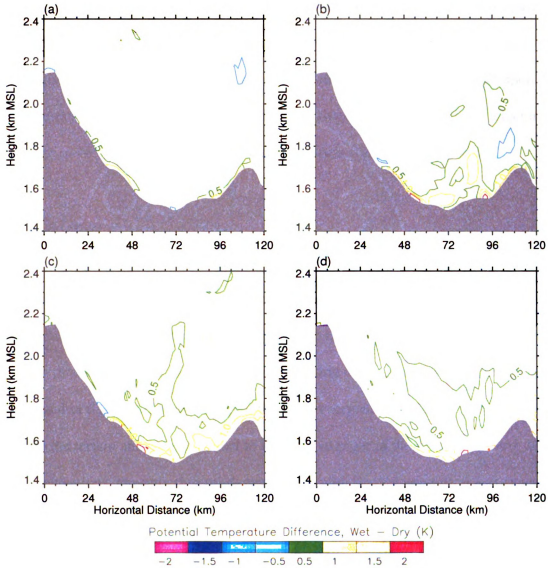

Fig. 4.1 Simulated difference of the potential temperature between the Wet and Dry soil moisture cases on an east-west vertical cross section through the ISS site at (a) 2100 MST, (b) 0000 MST, (c) 0300 MST, and (d) 0600 MST for IOP 5, 22-23 Oct. Images in this thesis are presented in color.

semi-desert portion of the slope which is more sensitive to slight variations in soil moisture. Over the upper portion of the slope warming from thermal conductivity was reduced allowing the downslope flow to develop with little delay or reduction in strength. It is suspected that a larger relative soil moisture value for the wet case, such as 1.0 as was tested by Banta and Gannon (1995), may increase the warming along the upper slope disrupting the downslope flow. This test was not considered because the soil moisture is unlikely to reach such values in the climatologically dry region of northern Arizona. Results from this sensitivity study indicate that soil moisture has limited impact upon the characteristics of a large scale downslope flow and should only be considered a factor in desert regions or where large variations in soil moisture content are observed.

2. Land cover

The sloping terrain in northern Arizona is unique because of its large horizontal length and variation of vegetation along the slope as a result of difference in altitudes. Such a drastic change in land cover was expected to have an impact on the downslope flow. The innermost grid of the model's representation of the land cover along the slope is illustrated in figure 4.2. Near the top of the slope evergreen needle leaf trees and shrubs dominate the terrain and were expected to limit the strength of the downslope flow, while at lower elevations, the smooth semi-desert surface with limited vegetation was expected to increase the strength of the downslope flow. To test this theory a homogeneous land cover of semi-desert was used to replace the woodlands at the top of the slope. Figure 4.3 shows the difference between the constant semi-desert land cover simulation and the

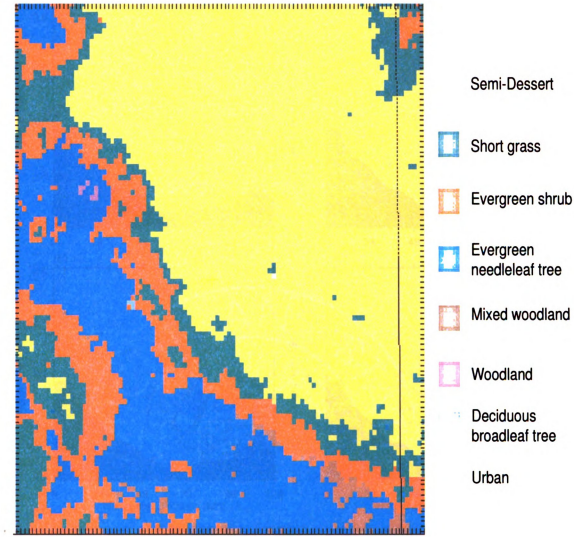

Fig. 4.2. Land cover classifications for the innermost grid of the variable land cover simulation. Images in this thesis are presented in color.

control case of variable land cover. A slight increase near 0.5 ms^{-1} in the strength of the downslope flow was observed near the top of the slope, and slight differences in the wind direction occurred at the ISS site near the base. These results indicate the downslope flow is not directly impacted by the drastic change in land cover, and the woodlands along the upper portion of the slope may reduce the strength of the downslope flow, but not significantly.

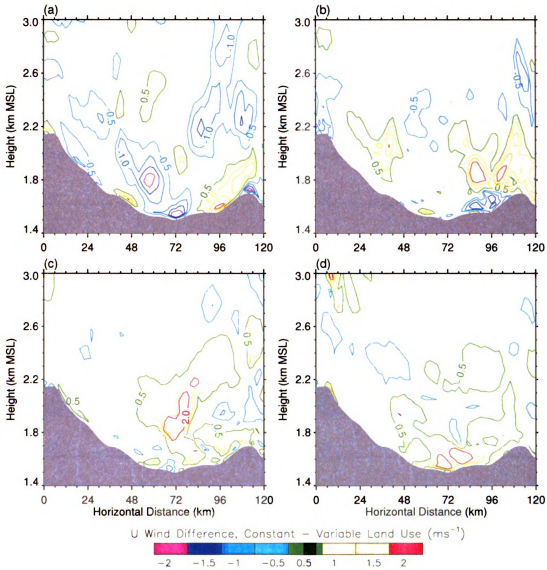

Fig. 4.3 Simulated difference of the U wind components between the constant semi-desert land cover and variable land cover cases on an east-west vertical cross section through the ISS site at (a) 2100 MST, (b) 0000 MST, (c) 0300 MST, and (d) 0600 MST for IOP 5, 22-23 Oct. Images in this thesis are presented in color.

3. Surface roughness

As Jeffreys (1922) discovered, surface friction and the pressure gradient force are the main balancing forces that drive downslope flow. It is thus expected that the model's representation of the surface roughness would have a large impact upon the

characteristics of the flow. A sensitivity simulation was run with a surface roughness value of z_0=0.05 m and the results are compared with the smoother surface roughness of z_0=0.01 m in the control case. It was expected that an increase in surface friction would reduce the strength of the downslope flow. Figure 4.4 shows the difference between the smoother control simulation and the larger roughness simulation. Very small changes

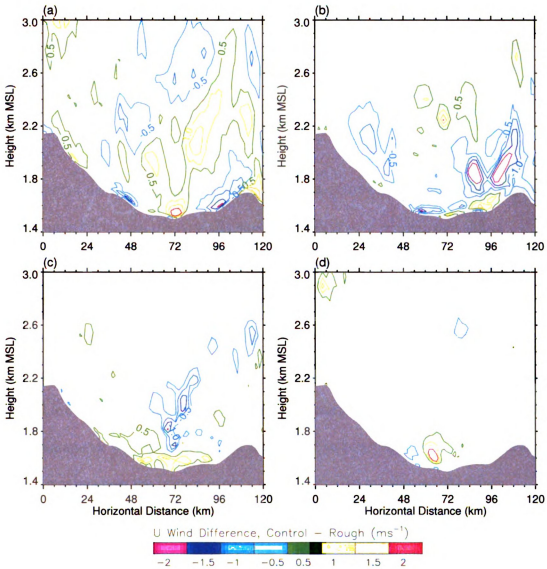

Fig. 4.4 Simulated difference of the U wind components between the Control surface roughness (.01) and Rough (.05) cases on an east-west vertical cross section through the ISS site at (a) 2100 MST, (b) 0000 MST, (c) 0300 MST, and (d) 0600 MST for IOP 5, 22-23 Oct. Images in this thesis are presented in color.

seem to occur away from the slope, signifying that the downslope flow is weakly sensitive to the increase in surface roughness. Similar results were found at the ISS site where the afternoon transition showed weaker winds for the increased roughness simulation, but after the development of the downslope flow the wind speeds and direction became identical (Fig. 3.15). This may support Kondo and Sato's (1988) theory of reduced importance of the surface friction term along smooth slopes. The downslope flow was also proven not to be strongly sensitive to the model's representation of the surface roughness.

4. Coriolis effect

Neglect of the Coriolis parameter within analytical solutions of downslope flow has been common because of the typically small horizontal scale of mountain slopes (Jeffreys, 1922; Prandtl, 1942; Mahrt, 1982). The slope in northern Arizona has a horizontal length of nearly 100 km, much larger than an average slope, potentially increasing the impact of the Coriolis effect on the downslope flow. The Coriolis force is also important in development of an inertial oscillation, which may also lead to a nocturnal low-level wind maximum similar to downslope flow. A sensitivity test of the Coriolis parameter was run to determine the impact on downslope flow and ensure that the wind maxima near the surface is not a result of inertial oscillation. The model simulations indicate that turning off the Coriolis force at night resulted in winds along the slope being slightly more variable in strength and direction throughout the night. Figure 4.5 shows the wind vectors near the surface at 0000 MST for the two simulations. While there is a larger variation in direction and speed than the other sensitivity tests (soil

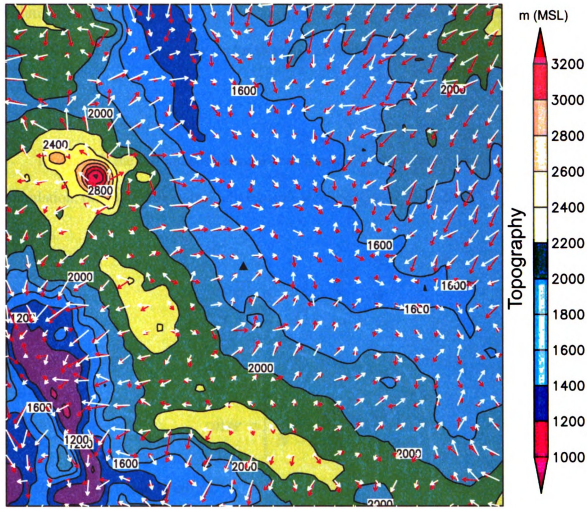

Fig. 4.5 Simulated near-surface wind vectors and topography contours in the innermost grid for the Coriolis case (white arrows) and No Coriolis case (red arrows) for IOP 5, 0000 MST, 22-23 Oct. The triangle indicates the location of the ISS site. Images in this thesis are presented in color.

moisture, land cover, surface roughness), the wind direction continues to flow downslope and the strength is maximized near the surface. This proves the circulation is the result of increased pressure gradient force by radiational cooling, and not a low-level wind maximum due to inertial oscillation associated with Coriolis force. The impact of the Coriolis parameter on the downslope flow was minimal, indicating the analytical

solutions may still neglect the Coriolis force for slopes of ~100 km in horizontal length within the mid-latitudes as they do for slopes of smaller scale.

5. Statistical comparison

To quantify the differences between each sensitivity simulation and the control simulation, the following statistical measures were computed, including the bias,

$$\overline{\phi}' = \frac{1}{N}\sum_{i=1}^{N} \phi' \tag{4.1}$$

root-mean-square error,

$$rmse = \left[\frac{1}{N-1}\sum_{i=1}^{N}(\phi_i')^2\right]^{1/2} \tag{4.2}$$

and standard deviation of errors,

$$sde = \left[\frac{1}{N-1}\sum_{i=1}^{N}(\phi_i' - \overline{\phi}')^2\right]^{1/2} \tag{4.3}$$

where ϕ' is the difference between the sensitivity simulation and the control simulation at each grid point. These statistical measures were computed over 6 hours from 2100 MST to 0300 MST the next day at the surface and 1 km above ground level (AGL) for the inner most grid with N equaling 62,424.

Table 4.1 summarizes the results of the statistical comparisons for each sensitivity study for IOP 5. As expected, the wet soil moisture produced a slight warm bias while the

Potential Temperature (K)

Vertical Level	Statistics	Wet Soil Moisture	Dry Soil Moisture	Semi-Desert	Surface Roughness	No Coriolis
Surface	Bias	0.376	-0.542	1.614	-0.028	0.317
	Rmse	0.846	0.737	2.618	0.444	2.360
	Error std dev	0.758	0.499	2.061	0.443	2.338
1 km AGL	Bias	-0.034	0.003	-0.061	-0.011	-0.323
	Rmse	0.191	0.055	0.166	0.181	0.712
	Error std dev	0.188	0.055	0.154	0.181	0.634

Wind Speed (ms^{-1})

Surface	Bias	-0.033	0.043	-0.008	-0.013	0.123
	Rmse	0.370	0.195	0.738	0.233	0.999
	Error std dev	0.368	0.190	0.738	0.233	0.991
1 km AGL	Bias	-0.016	-0.001	-0.014	-0.015	0.848
	Rmse	0.367	0.099	0.320	0.224	2.355
	Error std dev	0.367	0.099	0.320	0.223	2.197

Table 4.1. Model bias, rmse, and standard deviation (std dev) of the errors for (top) potential temperature, (middle) wind speed, and (bottom) wind direction based on grid 3 comparison between the control simulation and sensitivity studies between 2100 MST and 0300 MST for IOP 5 at the surface and 1 km above ground level (AGL).

dry soil moisture case yielded a -0.5 K cold bias. This slight variation of potential temperature may impact the strength of the surface inversion, but the differences in soil moisture showed minimal influence on the downslope wind speeds. Surprisingly, the semi-desert land cover simulation exhibited the largest potential temperature change near the surface with a 1.61 K warm bias. While surface wind speeds were not affected by the weakened inversion near the surface, it is interesting to note a warm bias for the overnight period when evergreen trees at the top of the slope are replaced with semi-desert land cover. It is not surprising that the influence of the soil moisture, vegetation, and roughness lengths are stronger at the surface than at 1 km above ground level. The largest influence on the strength of the downslope flow resulted from the neglect of the

Coriolis force, because Coriolis force affects the momentum budget of flows in the entire depths of the atmosphere and is proportional to wind speed. The resulting differences with and without Coriolis force are larger at 1 km where winds are stronger than at the surface. Although Coriolis force does not directly affect wind speed, the impact on wind direction would affect distribution of pressure resulting in increase or decrease in local pressure gradients and therefore changes in wind speed.

b. Limitations

While this study provides detailed analysis of the variations of characteristics of downslope flow observed over large uniform slopes, constraints within the observations and numerical model were encountered. These limitations are not deemed significant in achieving the objectives of the study, but are noteworthy for their role in designing an effective framework. Future research may be able to resolve these issues.

1. Experimental design

The Meteor Crater Experiment, or METCRAX, was not originally designed to investigate downslope flow over the sloping terrain in northern Arizona. Instead, the main objectives were to characterize the development and destruction of cold pools within the small scale, nearly symmetric Barringer Meteor Crater. Deployment of the meteorological towers and tethersondes were thus concentrated within the meteor crater. Observational sites outside the crater (ISS, SW Site, and Rim Site) were implemented to determine the impact of the background atmospheric conditions on the cold pool development. The locations of the three sites were chosen to best represent the

atmospheric conditions upwind of the crater, both near the surface and aloft, and not for detailed examination of the horizontal structure of the downslope flow. Although climatological analysis prior to the field campaign suggested possible influence of downslope flows at the experiment site, the frequency and strength of the downslope flow observed at the site were unexpected.

Ideal deployment of the observational sites to observe the downslope flow would have been equally spaced along the 100 km slope, similar to an earlier study by Haiden and Whiteman (2005) on a 12-km slope. Instead, the observations describing the downslope flow were all centrally located at mid-slope within a 5 km radius (Fig. 3.1). The high vertical resolution of the Sodar, rawinsondes, and meteorological towers enabled the study to effectively describe characteristics, especially the vertical structure, of the large scale downslope flow, despite limitations in describing the along-slope variation. To supplement the lack of horizontally indifferent observations, a three-dimensional numerical model was employed within this study to provide clues as to the horizontal extent of the downslope flow and its sensitivity to ambient conditions. Although the model results are validated against observations, the lack of sites at upper or lower segment of the slope limited the validation. Future research may resolve this issue through a detailed observational framework specifically designed for investigating the large scale downslope flow.

2. Period of observations

The temporal scale of cold pool development within the meteor crater is based on the diurnal cycle and ambient atmospheric conditions. As stated above, the main goal of

METCRAX was to observe the small scale physical mechanisms that impact cold pool development and destruction, and so an observational period of one month was determined to be an adequate time to capture five to ten quality nights of weak ambient winds needed for cold pool development. Over the month of October 2006, continuous observations from the meteorological towers and Sodar outside the meteor crater provided insight of the frequency and strength of the downslope flow (Fig. 3.2). Because these observations were restricted to 31 nights of one month, a more thorough climatological study of the downslope flow was not possible. A more descriptive framework was thus designed to achieve the main objectives of this study utilizing the enhanced observations and weak ambient wind conditions of the seven IOPs.

3. Vertical resolution of RAMS

Observations of the downslope flow have shown that the wind maximum and surface inversion typically occur within 50 to 100 m above the ground (Fig. 3.5). Vertical resolution of the RAMS model for each of the simulations, however, was limited to 20 m near the surface, where only a few grid points were within the observed downslope layer. This was expected to contribute to the higher depth of the wind maximum in the model simulation and the lower than observed wind speeds near the surface (Fig. 3.10). Attempts to increase vertical resolution to 10 or 15 m resulted in numerical instability. Despite this limitation the model was able to effectively resolve the transitional periods and the general characteristics of the downslope flow while also simulating the influence of synoptic scale features. Increased computer power may be able to enhance vertical and horizontal resolution of the model.

c. Future research

This study provides a detailed observational and numerical account of a large-scale downslope flow that occurs in northern Arizona. While the characteristics and sensitivities of the flow are well understood, the climatology of the circulation remains an unknown. Observations taken during the METCRAX campaign were limited to the fall season, and thus may not be representative of the flow observed in the winter, summer, or spring seasons. It is expected that the downslope flow will become stronger during the winter months due to increased efficiency of longwave radiation loss, but further observations are required to confirm this hypothesis. This may be achieved by correlating the observations taken during METCRAX with the year round hourly observations of the Automated Surface Observing Station (ASOS) located in Winslow, AZ (KINW) at the base of the slope. If the observations indicate a significant relationship in describing the strong southwesterly winds of the downslope flow, Winslow (KINW) may indicate how the downslope flow reacts to the changing seasons and provide validation for future model simulations.

Turbulence has proven to play a significant role in the impact of the ambient winds upon the downslope flow. The high vertical resolution of the observations taken during the METCRAX campaign may be able to observe the shear generated turbulence within the transitional layer and the various effects near the surface on the downslope flow. A thorough test of the bulk Richardson number utilizing these observations may also provide insight on the effectiveness of the parameter which is widely used to indicate mixing within a stable environment (Monti et al., 2002; Soler et al., 2002; Komatsu et al,

2005). This may lead to improved understanding of the turbulence parameterization scheme that best represents downslope flow over large horizontal slopes.

Future research of regional scale downslope flow will undoubtedly be driven by high resolution observations and complex numerical models representative of several atmospheric features. As resolutions become finer, understanding and predictability of downslope flow becomes easier and more applicable, benefiting society. Continued research and advancements in computer power will further knowledge of the thermal driven circulations which impact millions of people each day.

Appendix A – RAMS Options

Parameterization within the RAMS model can have a major impact on the resulting simulation. RAMS was designed to model several atmospheric circulations at varying scales, and thus offers a large selection of parameterization schemes. This section outlines the optimal parameterization schemes utilized to successfully model the downslope flow in northern Arizona. The RAMSIN file listed below details the options used for the control case of IOP 5. These options remained constant for the simulation of IOP 6 and the sensitivity studies, where only the aforementioned parameters were changed (soil moisture, land cover, surface roughness, and the coriolis parameter).

a. RAMSIN – IOP 5

```
!namelist
!#########################################################################
! 4.4.0
!
!#########################################################################

 $MODEL_GRIDS

! Simulation title (64 chars)

  EXPNME  = 'METCRAX – IOP5',
  VTABCUST = 'standard',

! RUNTYPE  = 'MAKESFC',      ! Type of run: MEMORY,   MAKESFC, MAKESST,
! RUNTYPE  = 'MAKEVFILE',
  RUNTYPE  = 'INITIAL',

  TIMEUNIT = 'h',          ! 'h','m','s' - Time units of TIMMAX, TIMSTR

  TIMMAX   = 29.,          ! Final time of simulation

! Start of simulation or ISAN processing
```

```
  IMONTH1 = 10,        ! Month
  IDATE1  = 22,        ! Day
  IYEAR1  = 2006,      ! Year
  ITIME1  = 1200,      ! GMT of model TIME = 0.

! Grid specifications

  NGRIDS  = 3,         ! Number of grids to run

  NNXP    = 80,86,102,     ! Number of x gridpoints
  NNYP    = 80,58,102,     ! Number of y gridpoints
  NNZP    = 35,35,35,      ! Number of z gridpoints
  NZG     = 11,            ! Number of soil layers
  NZS     = 1,             ! Maximum number of snow layers

  NXTNEST = 0,1,2,         ! Grid number which is the next coarser grid

! Coarse grid specifications

  IHTRAN  = 1,             ! 0-Cartesian, 1-Polar stereo
  DELTAX  = 32000.,
  DELTAY  = 32000.,        ! X and Y grid spacing

  DELTAZ  = 20.,           ! Z grid spacing (set to 0. to use ZZ)
  DZRAT   = 1.15,          ! Vertical grid stretch ratio
  DZMAX   = 1000.,         ! Maximum delta Z for vertical stretch

  ZZ      = 0.0,       ! Vertical levels if DELTAZ = 0
   30.0,    60.0,    90.0,   120.0,   150.0,
  180.0,   210.0,   240.0,   270.0,   300.0,
  330.0,   360.0,   390.0,   420.0,   450.0,
  480.0,   510.0,   540.0,   570.0,   600.0,
  630.0,   660.0,   690.0,   720.0,   750.0,
  780.0,   810.0,   840.0,   870.0,   900.0,
  930.0,   960.0,   990.0,  1020.0,  1050.0,
 1080.0,  1110.0,  1140.0,  1170.0,  1200.0,
 1230.0,  1260.0,  1290.0,  1320.0,  1350.0,
 1380.0,  1410.0,  1440.0,  1470.0,  1500.0,
 1533.0,  1569.3,  1609.2,  1653.2,  1701.5,
 1754.6,  1813.1,  1877.4,  1948.1,  2025.9,
 2111.5,  2205.7,  2309.3,

  DTLONG  = 4.,            ! Coarse grid long timestep
  NACOUST = 4,             ! Small timestep ratio
  IDELTAT = 0,             ! Timestep adjustment
                           !  =0 - constant timesteps
```

```
                        !  >0 - initial computation <0 - variable

                        ! Nest ratios between this grid and the next
                        !  coarser grid.
 NSTRATX = 1,4,4,       ! x-direction
 NSTRATY = 1,4,4,       ! y-direction
 NNDTRAT = 1,4,4,       ! Time

 NESTZ1  = 0,           ! Contort coarser grids if negative
 NSTRATZ1 = 3,2,2,1,
 NESTZ2  = 0,           ! Contort coarser grids if negative
 NSTRATZ2 = 3,3,3,2,2,1,


 POLELAT  =  35.03,      ! Latitude of pole point
 POLELON  = -111.01,     ! Longitude of pole point

 CENTLAT =  35.03,35.03,35.03,          ! Center lat/lon of grids, may or
 CENTLON = -111.01,-111.01,-111.01,     !  may not be same as pole point.

              ! Grid point on the next coarser
              !  nest where the lower southwest
              !  corner of this nest will start.
              !  If NINEST or NJNEST = 0, use CENTLAT/LON

 NINEST  = 1,0,0,       ! i-point
 NJNEST  = 1,0,0,       ! j-point
 NKNEST  = 1,1,1,       ! k-point

 NNSTTOP = 1,1,1,       ! Flag (0-no or 1-yes) if this
 NNSTBOT = 1,1,1,       ! Nest goes the top or bottom of the
                        !  coarsest nest.

 GRIDU   = 0.,0.,       ! u-component for moving grids
 GRIDV   = 0.,0.,       ! v-component for moving grids
                        !  (still not working!)

$END

$MODEL_FILE_INFO

! Variable initialization input

 INITIAL = 2,           ! Initial fields - 1=horiz.homogeneous, 2=variable
 VARFPFX = 'isan/a',    ! Varfile initialization file prefix
 VWAIT1  = 0.,          ! Wait between each VFILE check (s)
```

```
 VWAITTOT = 0.,          ! Total wait befor giving up on a VFILE (s)

 NUDLAT  = 5,            ! Number of points in lateral bnd region
 TNUDLAT  = 900.,        ! Nudging time scale(s) at lateral boundary
 TNUDCENT = 14400.,      ! Nudging time scale(s) in center of domain
 TNUDTOP  = 0.,          ! Nudging time scale (s) at top of domain
 ZNUDTOP  = 0.,          ! Nudging at top of domain above height(m)
```

! History file input

```
 TIMSTR  = 6.,           ! Time of history start (see TIMEUNIT)
 HFILIN  = 'hist/a-H-2000-07-30-180000.vfm',
                         ! Input history file name
```

! Analysis file input for assimilation (currently LEAF variables)

```
 IPASTIN  = 0,           ! Initialize various fields from analysis file?
                         !  1=yes, 0=no
 PASTFN   = 'anal/a-A-2000-01-09-000000-head.txt',
                         ! Input analysis file name
```

```
! History/analysis file output

 IOUTPUT  = 2,           ! 0-no files, 1-save ASCII, 2-save binary
 HFILOUT  = 'hist/a',    ! History file prefix
 AFILOUT  = 'anal/a',    ! Analysis file prefix
 ICLOBBER = 1,           ! 0=stop if files exist, 1=overwite files
 IHISTDEL = 1,           ! 0=keep all hist files, 1=delete previous
 FRQHIS   = 46800.,      ! History file frequency
 FRQANL   = 3600.,       ! Analysis file frequency
 FRQLITE  = 0.,          ! Analysis freq. for "lite" variables
                         !  = 0 : no lite files
 XLITE    = '/0:0/',     ! nums>0 are absolute grid indexes
 YLITE    = '/0:0/',     ! nums<0 count in from the domain edges
 ZLITE    = '/0:0/',     ! nums=0 are domain edges
 AVGTIM   = -300.,       ! Averaging time for analysis variables
                         !  must be abs(AVGTIM) <= FRQANL
                         !  > 0 : averaging is centered at FRQANL
                         !  < 0 : averaging ends at FRQANL
                         !  = 0 : no averaged files
 FRQMEAN  = 0.,          ! Analysis freq. for "averaged" variables
 FRQBOTH  = 0.,          ! Analysis freq. for both "averaged" and
                         !  "lite" variables
 KWRITE   = 1,           ! 1-write,0-don't write scalar K's to anal.
```

```
! Printed output controls

 FRQPRT  = 3600.,        ! Printout frequency
 INITFLD = 1,            ! Initial field print flag 0=no prnt,1=prnt

! Input topography variables

 SFCFILES = 'sfc/sfc',   ! File path and prefix for surface files.
 SSTFPFX  = 'sst/sst',   ! Path and prefix for sst files

 ITOPTFLG = 1,1,1,       ! 2 - Fill data in "rsurf"
 ISSTFLG  = 1,1,0,       ! 0 - Interpolate from coarser grid
 IVEGTFLG = 1,1,1,       ! 1 - Read from standard Lat/Lon data file
 ISOILFLG = 2,2,2,       ! Soil files not yet available: avoid isoilflg=1

 NOFILFLG = 1,1,1,       ! 2 - Fill data in "rsurf"
                         ! 0 - Interpolate from coarser grid

 IUPDSST  = 0,           ! 0 - No update of SST values during run
                         ! 1 - Update SST values during run

       ! The following only apply for IxxxxFLG=1
 ITOPTFN  = 'geodata/DEM30s/EL', 'geodata/DEM30s/EL', 'geodata/DEM30s/EL',
 ISSTFN   = 'geodata/sst/S', 'geodata/sst/S', 'geodata/sst/S',
 IVEGTFN  = 'geodata/ogedata/GE', 'geodata/ogedata/GE', 'geodata/ogedata/GE',
 ISOILFN  = ' ',             ! Soil files not yet available

! Topography scheme

 ITOPSFLG = 1,1,1,       ! 0 = Average Orography
                         ! 1 = Silhouette Orography
                         ! 2 = Envelope Orography
                         ! 3 = Reflected Envelope Orography
 TOPTENH  = 1.,1.,1.,    ! For ITOPSFLG=1, Weighting of topo
                         !   silhouette averaging
                         ! For ITOPSFLG=2 or 3, Reflected Envelope
                         !   and Envelope Orography enhancement factor
 TOPTWVL  = 4.,4.,4.,    ! Topo wavelength cutoff in filter

! Surface Roughness scheme

 IZ0FLG   = 0,0,0,       ! 0 = Based of vege, bare soil and water surface
                         ! 1 = Subgrid scale orograhic roughness
 Z0MAX    = 2.,2.,2.,    ! Max zo for IZ0FLG=1
 Z0FACT   = 0.005,       ! Subgrid scale orograhic roughness factor
```

```
! Microphysics collection tables

  MKCOLTAB = 0,              ! Make table: 0 = no, 1 = yes
  COLTABFN = '/scratch/savagelo/rams/test/geodata/micro/ct2.0',
                             ! Filename to read or write

$END

$MODEL_OPTIONS

  NADDSC  = 0,               ! Number of additional scalar species

! Numerical schemes

  ICORFLG = 1,               ! Coriolis flag/2D v-component - 0 = off, 1 = on

  IBND    = 1,               ! Lateral boundary condition flags
  JBND    = 1,               !  1-Klemp/Wilhelmson, 2-Klemp/Lilly,
                             !  3-Orlanski,       4-cyclic
  CPHAS   = 20.,             ! Phase speed if IBND or JBND = 1
  LSFLG   = 0,               ! Large-scale gradient flag for variables other than
                             !  normal velocity:
                             !  0 = zero gradient inflow and outflow
                             !  1 = zero gradient inflow, radiative b.c. outflow
                             !  2 = constant inflow, radiative b.c. outflow
                             !  3 = constant inflow and outflow
  NFPT    = 0,               ! Rayleigh friction - number of points from the top
  DISTIM  = 60.,             !                   - dissipation time scale

! Radiation parameters

  ISWRTYP = 1,               ! Shortwave radiation type
  ILWRTYP = 1,               ! Longwave radiation type
                             !  0-none, 2-Mahrer/Pielke, 1-Chen
  RADFRQ  = 300.,            ! Freq. of radiation tendency update (s)
  LONRAD  = 1,               ! Longitudinal variation of shortwave
                             !  (0-no, 1-yes)

! Cumulus parameterization parameters

  NNQPARM = 0,0,0,           ! Convective param. flag (0-off, 1-on)
  CONFRQ  = 1200.,           ! Frequency of conv param. updates (s)
  WCLDBS  = .001,            ! Vertical motion needed at cloud base for
                             !  to trigger convection
```

! Surface layer and soil parameterization

```
 NPATCH  = 3,          ! Number of patches per grid cell (min=2)

 NVEGPAT = 2,          ! Number of patches per grid cell to be filled from
                       !  vegetation files (min of 1, max of NPATCH-1)

 ISFCL   = 1,          ! Surface layer/soil/veg model
                       !  0 - specified surface layer gradients
                       !  1 - soil/vegetation model

 NVGCON  = 11,         ! Vegetation type (see below)

 !  0 – Ocean                          1 – Lakes, rivers, streams
 !  2 – Ice cap/glacier                3 – Evergreen needleleaf tree
 !  4 – Deciduous needleleaf tree      5 – Deciduous broadleaf tree
 !  6 – Evergreen broadleaf tree       7 – Short grass
 !  8 – Tall grass                     9 – Desert
 ! 10 – Semi-desert                   11 – Tundra
 ! 12 – Evergreen shrub               13 – Deciduous shrub
 ! 14 – Mixed woodland                15 – Crop/mixed farming
 ! 16 – Irrigated crop                17 – Bog or marsh
 ! 18 – Evergreen needleleaf forest   19 – Evergreen broadleaf forest
 ! 20 – Deciduous needleleaf forest   21 – Deciduous broadleaf forest
 ! 22 – Mixed cover                   23 – Woodland
 ! 24 – Wooded grassland              25 – Closed shrubland
 ! 26 – Open shrubland                27 – Grassland
 ! 28 – Cropland                      29 – Bare ground
 ! 30 – Urban and built up

 PCTLCON = 1.,         ! Constant land % if for all domain
 NSLCON  = 6,          ! Constant soil type if for all domain

 !  1 -- sand          2 -- loamy sand     3 -- sandy loam
 !  4 -- silt loam     5 -- loam           6 -- sandy clay loam
 !  7 -- silty clay loam  8 -- clay loam   9 -- sandy clay
 ! 10 -- silty clay    11 -- clay          12 -- peat

 ZROUGH  = .01,        ! Constant roughness if for all domain
 ALBEDO  = .2,         ! Constant albedo if not running soil model
 SEATMP  = 280.,       ! Constant water surface temperature

 DTHCON  = 0.,         ! Constant sfc layer  temp grad for no soil
 DRTCON  = 0.,         ! Constant sfc layer moist grad for no soil
```

```
 SLZ     = -.50,-.40,-.30,-.25,-.20,-.16,-.12,-.09,-.06,-.03,-.01,
                                ! Soil grid levels

 SLMSTR  = 0.20,0.20,0.20,0.20,0.20,0.20,0.20,0.20,0.20,0.20,0.20,
                                ! Initial soil moisture

 STGOFF  = 5.,5.,5.,5.,3.5,2.,.5,-1.,-1.5,-1.8,-2.,
                                ! Initial soil temperature offset
                                !  from lowest atmospheric level
```

! Eddy diffusion coefficient parameters

```
 IDIFFK  = 1,1,1,               ! K flag:
                                ! 1 - Horiz deform/Vert Mellor-Yamada
                                ! 2 - Anisotropic deformormation
                                !     (horiz & vert differ)
                                ! 3 - Isotropic deformation
                                !     (horiz and vert same)
                                ! 4 - Deardorff TKE (horiz and vert same)
 IHORGRAD = 1,                  ! 1 - horiz grad frm decomposed sigma grad
                                ! 2 - true horizontal gradient.
                                !     Non-conserving, but allows small DZ
 CSX     = .2,.2,.2,            ! Deformation horiz. K's coefficient
 CSZ     = .2,.2,.2,            ! Deformation vert. K's coefficient
 XKHKM   = 3.,3.,3.,            ! Ratio of horiz K_h to K_m for deformation
 ZKHKM   = 3.,3.,3.,            ! Ratio of vert K_h to K_m for deformation
 AKMIN   = .2,.2,.2,            ! Ratio of minimum horizontal eddy
                                !  viscosity coefficientto typical value
                                !  from deformation K
```

! Microphysics

```
 LEVEL   = 1,                   ! Moisture complexity level

 ICLOUD  = 4,                   ! Microphysics flags
 IRAIN   = 2,                   !-------------------
 IPRIS   = 5,                   !  1 - diagnostic concen.
 ISNOW   = 2,                   !  2 - specified mean diameter
 IAGGR   = 2,                   !  3 - specified y-intercept
 IGRAUP  = 2,                   !  4 - specified concentration
 IHAIL   = 2,                   !  5 - prognostic concentration

 CPARM   = .3e9,                ! Microphysics parameters
 RPARM   = 1e-3,                !------------------------
 PPARM   = 0.,                  ! Characteristic diameter, # concentration
```

```
 SPARM  = 1e-3,          !   or y-intercept
 APARM  = 1e-3,
 GPARM  = 1e-3,
 HPARM  = 3e-3,

 GNU    = 2.,2.,2.,2.,2.,2.,          ! Gamma shape parms for
                                      ! cld rain pris snow aggr graup hail

$END

$MODEL_SOUND

! Sounding specification

! Flags for how sounding is specified

 IPSFLG  = 1,                    ! Specifies what is in PS array
                                 !  0-pressure(mb) 1-heights(m)
                                 !  PS(1)=sfc press(mb)

 ITSFLG  = 0,                    ! Specifies what is in TS array
                                 ! 0-temp(C) 1-temp(K) 2-pot. temp(K)

 IRTSFLG = 3,                    ! Specifies what is in RTS array
                                 !  0-dew pnt.(C) 1-dew pnt.(K)
                                 !  2-mix rat(g/kg)
                                 !  3-relative humidity in %,
                                 !  4-dew pnt depression(K)

 IUSFLG  = 1,                    ! Specifies what is in US and VS arrays
                                 !  0-u,v component(m/s)
                                 !  1-umoms-direction, vmoms-speed

 HS     = 0.,
 PS     =
 TS     =
 RTS    =
 US     =
 VS     =

$END
```

```
$MODEL_PRINT

! Specifies the fields to be printed during the simulation

  NPLT    = 1,              ! Number of fields printed at each time
                            !  for various cross-sections (limit of 50)

  IPLFLD  = 'WP',           ! Field names - see table below

  PLFMT(1) = '0PF7.3',      ! Format spec. if default is unacceptable

  IXSCTN  = 3,3,3,3,        ! Cross-section type (1=XZ, 2=YZ, 3=XY)

  ISBVAL  = 10,10,10,10,    ! Grid-point slab value for third direction

$END

$ISAN_CONTROL

! Isentropic control

  ISZSTAGE = 1,             ! Main switches for isentropic-sigz
  IVRSTAGE = 1,             !  "varfile" processing

  ISAN_INC = 0300,          ! ISAN processing increment (hhmm)
                            !  range controlled by TIMMAX,
                            !  IYEAR1,...,ITIME1

  GUESS1ST = 'PRESS',       ! Type of first guess input- 'PRESS', 'RAMS'

  I1ST_FLG = 1,             ! What to do if first guess file should be used,
                            !  but does not exist.
                            !    1 = I know it may not be there,
                            !       skip this data time
                            !    2 = I screwed up, stop the run
                            !    3 = interpolate first guess file from nearest
                            !       surrounding times, stop if unable
                            !       (not yet available)

  IUPA_FLG = 3,             ! UPA-upper air, SFC-surface
  ISFC_FLG = 3,             ! What to do if other data files should be used,
                            !  but does not exist.
                            !    1 = I know it may not be there,
                            !       skip this data time
                            !    2 = I screwed up, stop the run
```

```
                                    !    3 = Try to continue processing anyway

! Input data file prefixes

  IAPR    = 'data/edas40.',         ! Input press level dataset
  IARAWI  =' ',                     ! Archived rawindsonde file name
  IASRFCE = ' ',                    ! Archived surface obs file name

! File names and dispose flags

  VARPFX   = 'isan/a',              ! isan file names prefix
  IOFLGISZ = 0,                     ! Isen-sigz file flag: 0 = no write, 1 = write
  IOFLGVAR = 1,                     ! Var file flag:       0 = no write, 1 = write

$END

$ISAN_ISENTROPIC


! Specify isentropic levels

  NISN   = 43,                      ! Number of isentropic levels
  LEVTH  = 280,282,284,286,288,290,292,294,296,298,300,303,306,309,312,
           315,318,321,324,327,330,335,340,345,350,355,360,380,400,420,
           440,460,480,500,520,540,570,600,630,670,700,750,800,

! Analyzed grid information:

  NIGRIDS = 1,                      ! Number of RAMS grids to analyze

  TOPSIGZ = 4000.,                  ! Sigma-z coordinates to about this height

  HYBBOT  = 4000.,                  ! Bottom (m) of blended sigma-z/isentropic
                                    !  layer in varfiles
  HYBTOP  = 6000.,                  ! Top (m) of blended sigma-z/isentropic layr

  SFCINF  = 1000.,                  ! Vert influence of sfc observation analysis

  SIGZWT  = 1.,                     ! Weight for sigma-z data in varfile:
                                    !  0. = no sigz data,
                                    !  1. = full weight from surface to HYBBOT

  NFEEDVAR = 1,                     ! 1 = feed back nested grid varfile, 0 = not

! Observation number limits:
```

```
MAXSTA  = 500,          ! maximum number of rawindsondes
                        !   (archived + special)
MAXSFC  = 5000,         ! maximum number of surface observations

NONLYS  = 0,            ! Number of stations only to be used
IDONLYS = '76458',      ! Station IDs used

NOTSTA  = 0,            ! Number of stations to be excluded
NOTID   = 'r76458',     ! Station IDs to be excluded
                        !  Prefix with 'r' for rawindsonde,
                        !          's' for surface

IOBSWIN = 7200,         ! Observation acceptance time window
                        !  Obs are accepted at the analysis time T if
                        !  for IOBSWIN > 0: T-IOBSWIN < obs_time <
                        !         T+IOBSWIN
                        !  for IOBSWIN = 0: T = obs_time
                        !  for IOBSWIN < 0: T-|IOBSWIN| < obs_time

STASEP  = .1,           ! Minimum sfc station separation in degrees.
                        !  Any surface obs within this distance
                        !  of another obs will be thrown out
                        !  unless it has less missing data,
                        !  in which case the other obs will be
                        !  thrown out.

ISTAPLT = 0,            ! If ISTAPLT = 1, soundings are plotted;
ISTAREP = 0,            ! If ISTAREP = 1, soundings are listed;
                        !  no objective analysis is done.
                        ! If ISTAREP/ISTAPLT = 0, normal processing
                        !  is done

IGRIDFL = 3,            ! Grid flag=0 if no grid point, only obs
                        !         1 if all grid point data and obs
                        !         2 if partial grid point and obs
                        !         3 if only grid data
                        !         4 all data... fast

GRIDWT  = .1,.1,.1,.1,  ! Relative weight for the gridded press data
                        !  compared to the observational data in
                        !  the objective analysis

GOBSEP  = 5.,           ! Grid-observation separation (degrees)
GOBRAD  = 5.,           ! Grid-obs proximity radius (degrees)
```

```
 WVLNTH  = 1200.,1200.,1200.,1200.,    ! Used in S. Barnes objective analysis.
                                       !  Wavelength in km to be retained to the
                                       ! RESPON % from the data to the upper air
                                       !  grids.
 SWVLNTH = 750.,750.,750.,750.,        ! Wavelength for surface objective analysis

 RESPON  = .90,.90,.90,.90,            ! Percentage of amplitude to be retained.

$END
```

b. Discussion of important RAMS options

1. Model integration

The RAMS model is able to initialize and integrate the model fields utilizing three dimensional atmospheric data output from National Center for Environmental Prediction (NCEP) large scale model reanalysis. The reanalysis packages available for this study were the North American Regional Reanalysis (NARR), the NCEP North American Model (NAM), and the NCEP Global Forecast System (GFS). Each of these model integration packages were tested for their performance in comparisons with observations from the downslope flow in northern Arizona. The NAM output demonstrated the best performance presumably due to the finer horizontal resolution and higher output frequency (every 3 hours), and was thus used for integration in every simulation within this study.

2. Lateral boundary conditions

The Klemp and Wilhelmson (1978) boundary layer scheme was chosen because of the superior performance of open lateral boundary conditions in resolving mesoscale and local-scale features like downslope flow (Bader et al., 1987). With open boundary

conditions the downslope flow is able to propagate out of the model domain without reflecting back. This scheme is dependent on the phase speed (20 ms^{-1}) to advect the normal velocity component from the interior to the lateral boundary (Pielke et al., 1992).

3. Radiation

The Chen and Cotton (1983) radiation parameterization scheme was chosen due to the importance of condensate in the atmosphere, which is not accounted for by the Mahrer and Pielke (1977) scheme. Downslope flow is a result of the decrease in net longwave radiation near the surface, which may be impacted by clouds or large increases in atmospheric moisture that can absorb and reflect longwave radiation back towards the surface. Neglect of these parameters would likely yield inaccurate results.

4. Turbulence diffusion

The Mellor and Yamada (1982) level 2.5 scheme was chosen to best represent turbulent kinetic energy (TKE) within the three grids. By simulating the balance of buoyancy, shear production, and turbulence dissipation, the Mellor and Yamada (1982) level 2.5 scheme provides the best option in RAMS for considering turbulence within the downslope flow layer (Skyllingstad, 2003). The scheme is also ideal because it allows the turbulent exchange across the jet maximum which is essential for accurately simulating downslope flow (Arritt and Pielke, 1986). The main assumption of the Mellor and Yamada (1982) level 2.5 scheme is the domination of vertical mixing in calculating turbulent mixing, which requires large horizontal grid spacing compared to vertical spacing. Model simulations within this study satisfy this assumption as the aspect ratio

between the horizontal and vertical spacing on the innermost grid is 100:1, sufficient for an accurate representation.

Appendix B – IOP Observations and Simulations

The observations and simulations presented within Chapter III were limited to three IOPs (4, 5, 6) to best represent the downslope flow in varying ambient wind conditions. Observations from the remaining IOPs (1, 2, 3, 7) do exhibit the general characteristics of the downslope flow, but were not ideal for analysis due to variable ambient conditions overnight. Supplemental observations and model simulations from all seven IOPs are offered within this section to enhance description of the downslope flow in northern Arizona.

a. IOP 1, 8 October 2006

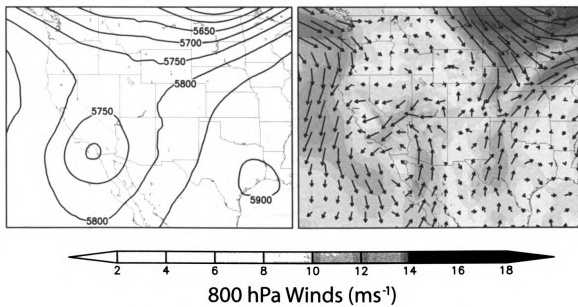

Fig. B.1 0500 MST 500-hPa geopotential height fields (left) and 800-hPa wind vectors (right) for IOP 1, 08 October, based on North American Regional Reanalysis (NARR) data.

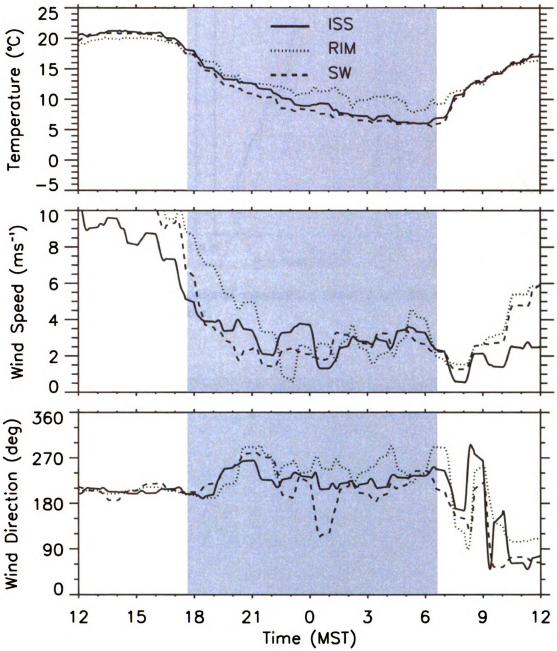

Fig. B.2 Time series of surface temperature, wind speed, and wind direction at ISS, RIM, and SW sites for IOP 1, 07-08 October. Nighttime period is indicated by the gray shading.

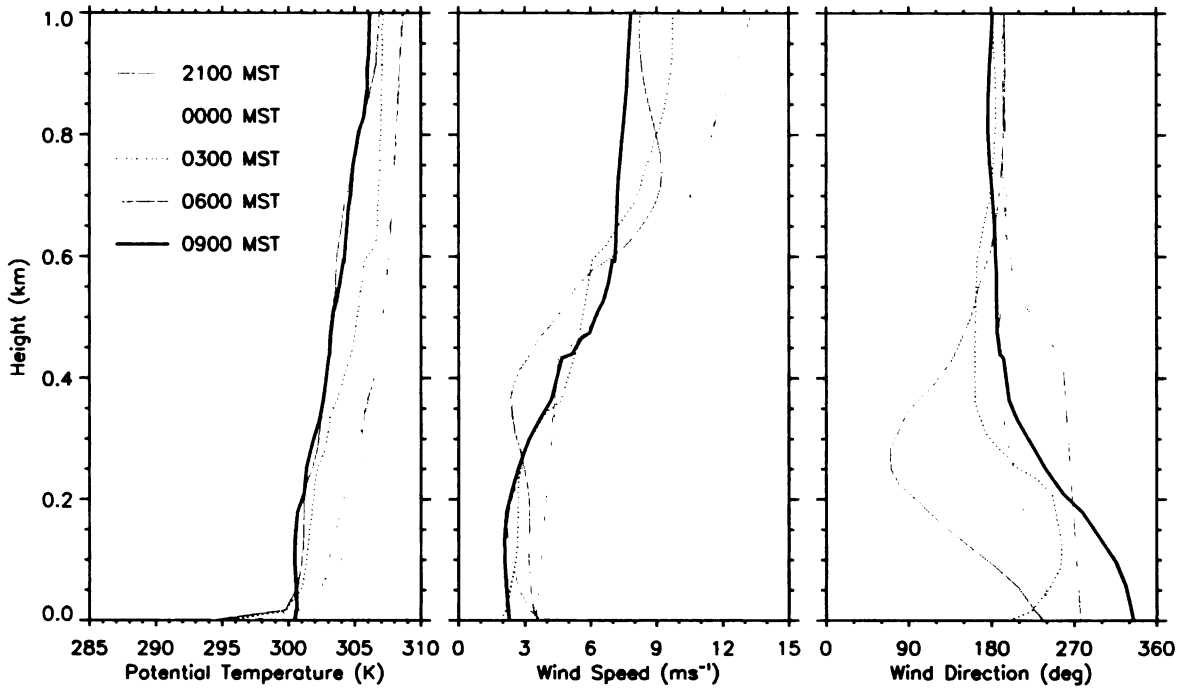

Fig. B.3 Vertical profiles of potential temperature, wind speed, and wind direction at the ISS site for IOP 1, 07-08 October.

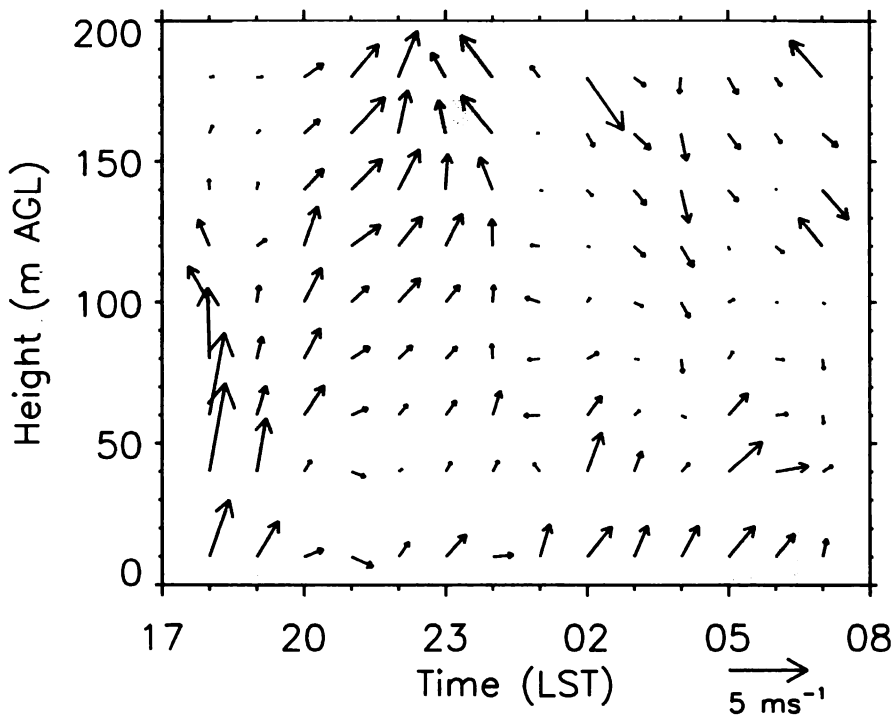

Fig. B.4 Hourly wind vectors from the Sodar and surface observations at the SW site for IOP 1, 1800 MST 07 Oct. - 0700 MST 08 Oct. Nighttime period is indicated by the gray shading.

b. IOP 2, 12 October 2006

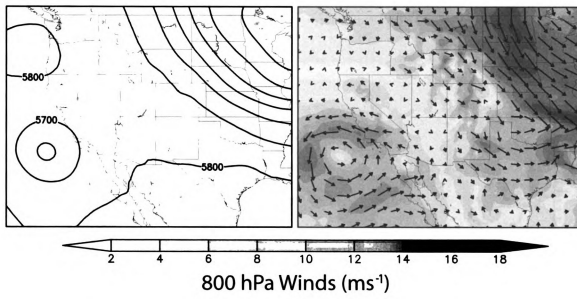

Fig. B.5 0500 MST 500-hPa geopotential height fields (left) and 800-hPa wind vectors (right) for IOP 2, 12 October, based on North American Regional Reanalysis (NARR) data.

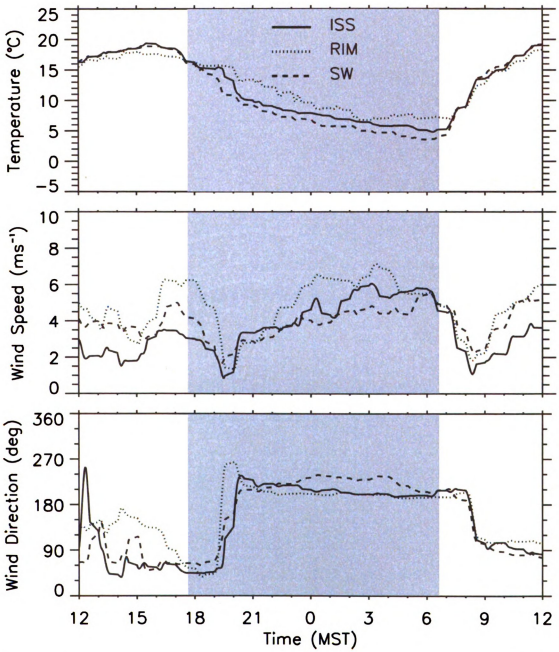

Fig. B.6 Time series of surface temperature, wind speed, and wind direction at ISS, RIM, and SW sites for IOP 2, 11-12 October. Nighttime period is indicated by the gray shading.

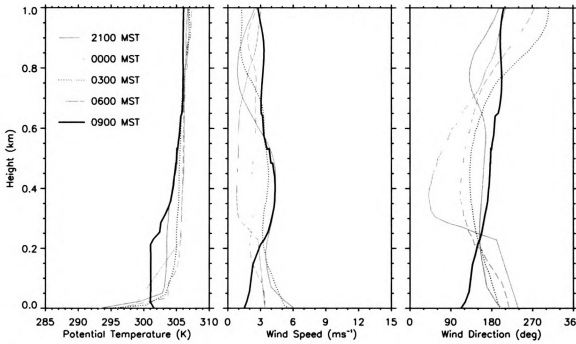

Fig. B.7 Vertical profiles of potential temperature, wind speed, and wind direction at the ISS site for IOP 2, 11-12 October.

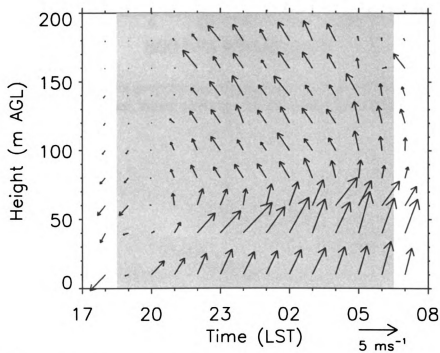

Fig. B.8 Hourly wind vectors from the Sodar and surface observations at the SW site for IOP 2, 1800 MST 11 Oct. - 0700 MST 12 Oct. Nighttime period is indicated by the gray shading.

c. IOP 3, 19 October 2006

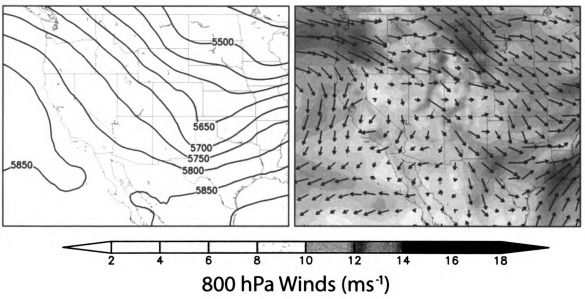

Fig. B.9 0500 MST 500-hPa geopotential height fields (left) and 800-hPa wind vectors (right) for IOP 3, 19 October, based on North American Regional Reanalysis (NARR) data.

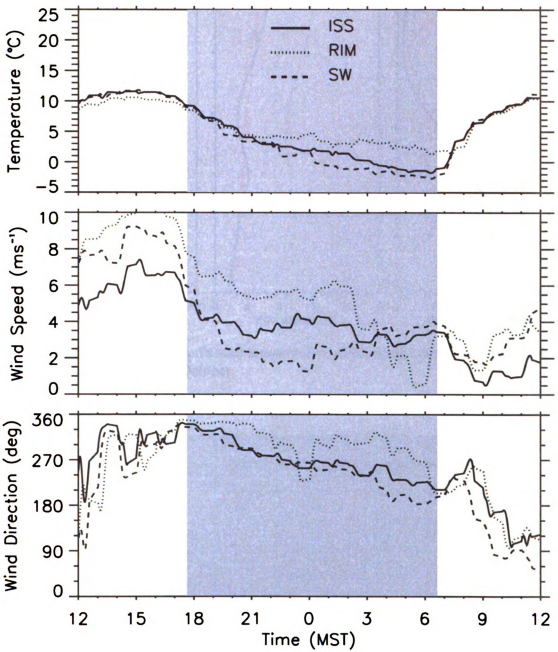

Fig. B.10 Time series of surface temperature, wind speed, and wind direction at ISS, RIM, and SW sites for IOP 3, 18-19 October. Nighttime period is indicated by the gray shading.

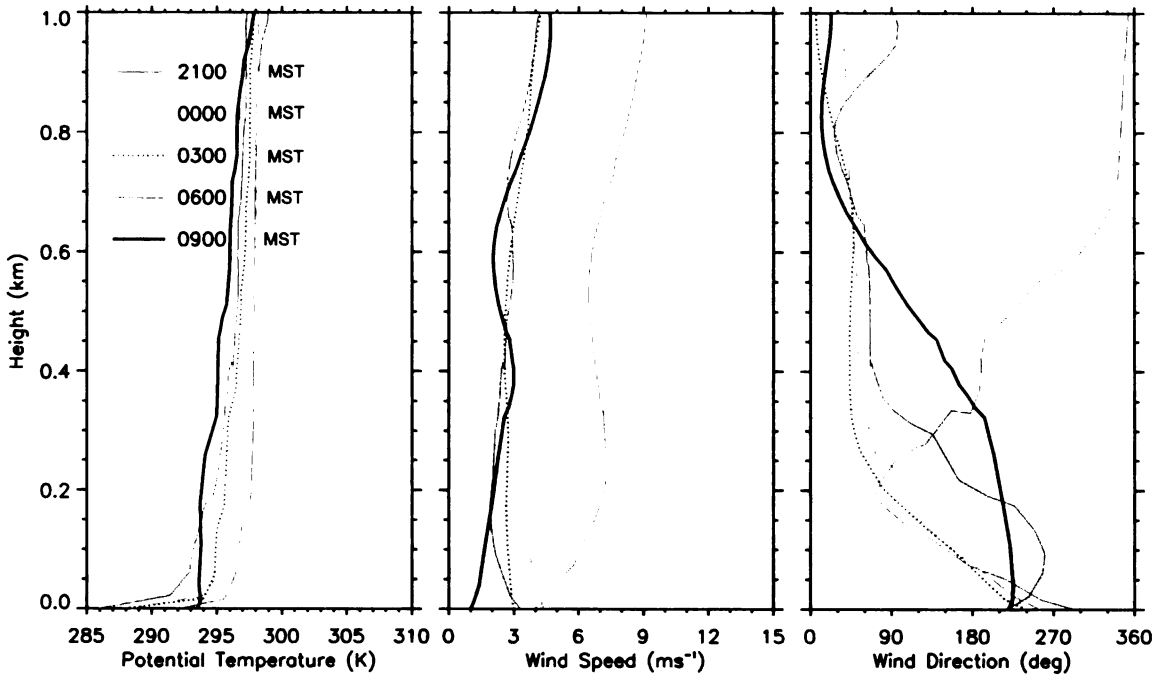

Fig. B.11 Vertical profiles of potential temperature, wind speed, and wind direction at the ISS site for IOP 3, 18-19 October.

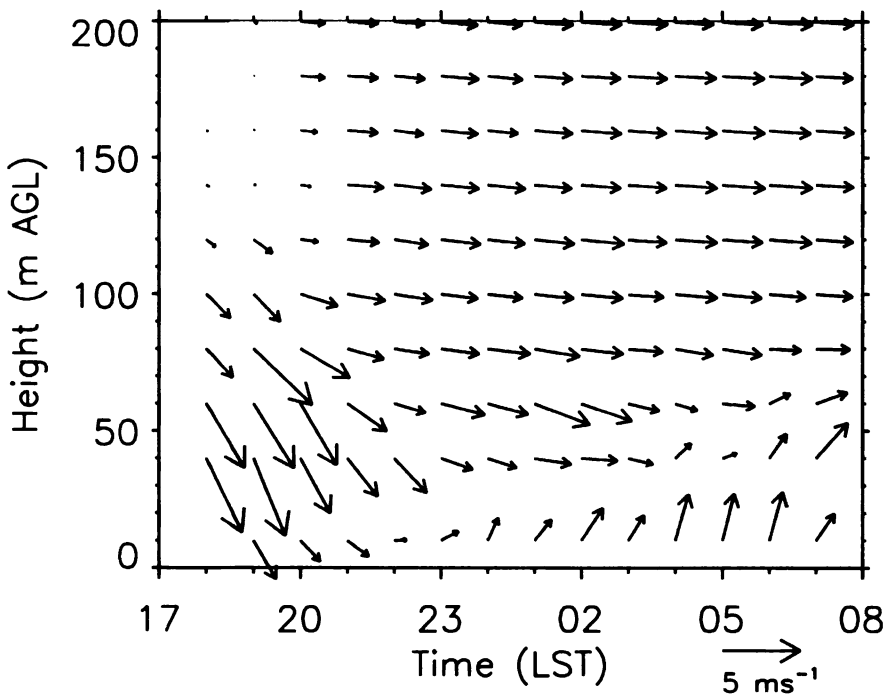

Fig. B.12 Hourly wind vectors from the Sodar and surface observations at the SW site for IOP 3, 1800 MST 18 Oct. - 0700 MST 19 Oct. Nighttime period is indicated by the gray shading.

d. IOP 7, 31 October 2006

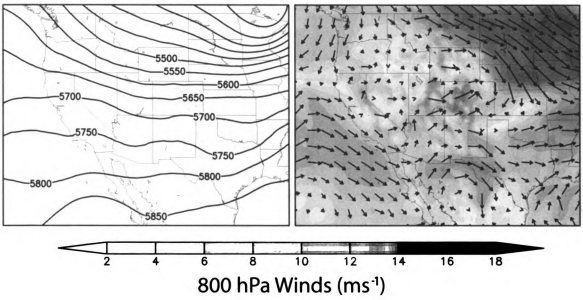

Fig. B.13 0500 MST 500-hPa geopotential height fields (left) and 800-hPa wind vectors (right) for IOP 7, 31 October, based on North American Regional Reanalysis (NARR) data.

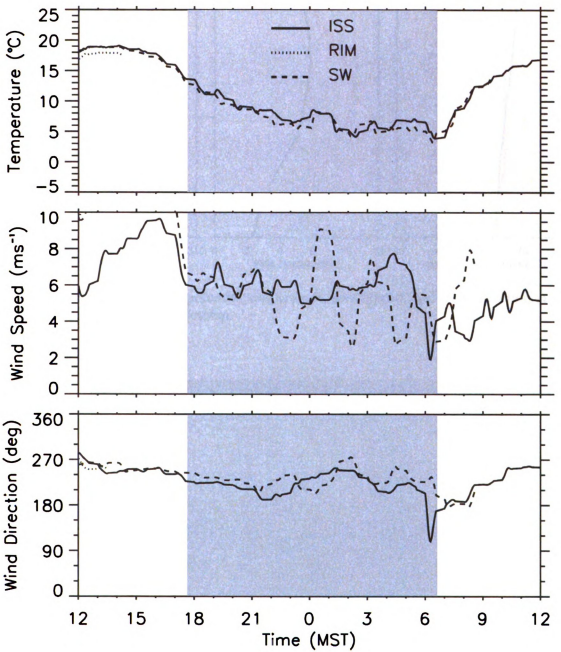

Fig. B.14 Time series of surface temperature, wind speed, and wind direction at ISS, RIM, and SW sites for IOP 7, 30-31 October. Observations from the RIM and SW site included erroneous data which was excluded. Nighttime period is indicated by the gray shading.

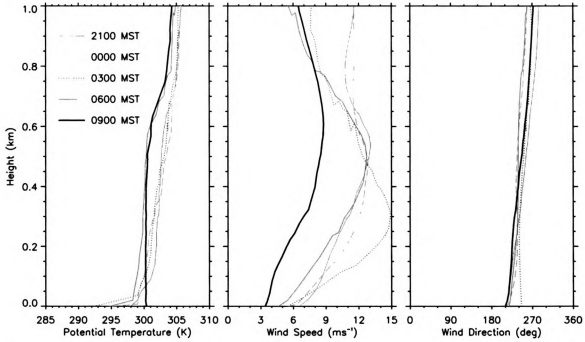

Fig. B.15 Vertical profiles of potential temperature, wind speed, and wind direction at the ISS site for IOP 7, 30-31 October.

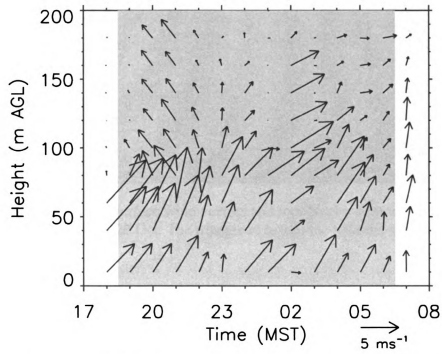

Fig. B.16 Hourly wind vectors from the Sodar and surface observations at the SW site for IOP 7, 1800 MST 30 Oct. - 0700 MST 31 Oct. Nighttime period is indicated by the gray shading.

e. IOP 5 (RAMS Simulation)

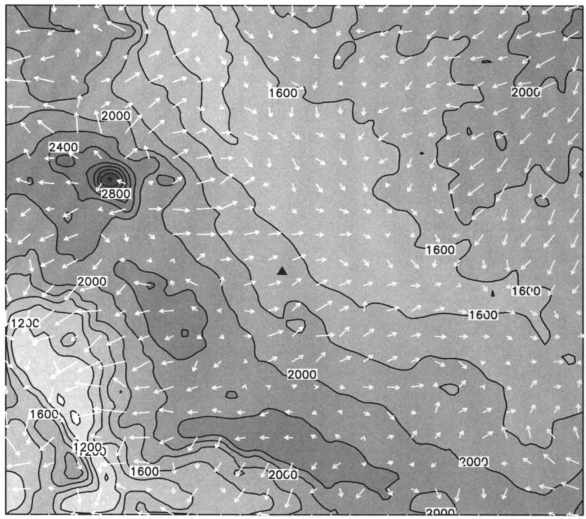

Fig. B.17 Simulated near-surface wind vectors and topography contours in the innermost grid for IOP 5, 2100 MST 22 Oct. The triangle indicates the location of the ISS site.

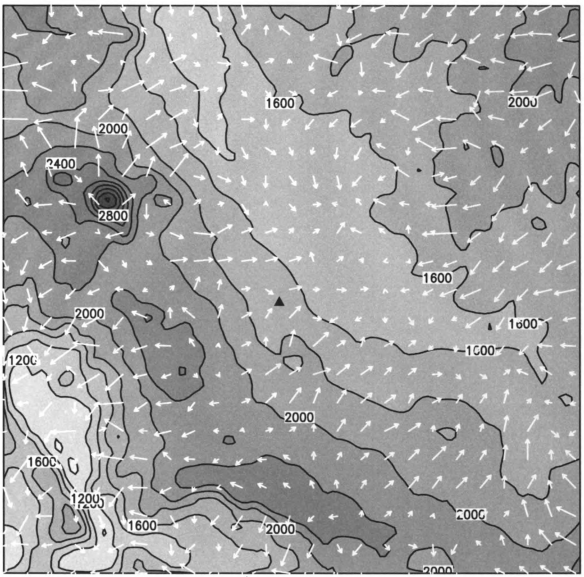

Fig. B.18 Simulated near-surface wind vectors and topography contours in the innermost grid for IOP 5, 0300 MST 23 Oct. The triangle indicates the location of the ISS site.

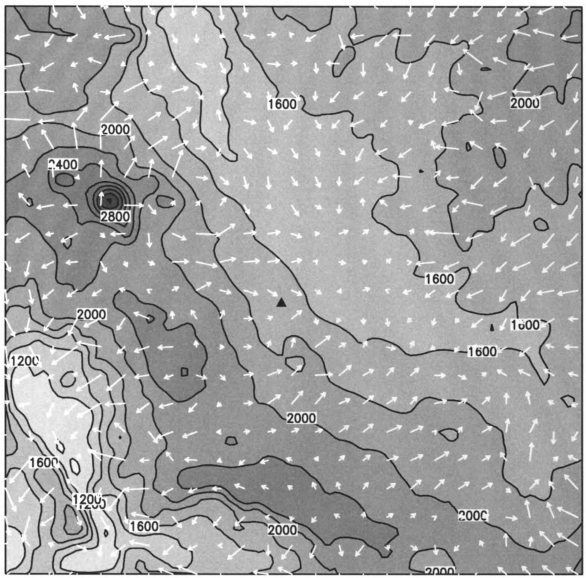

Fig. B.19 Simulated near-surface wind vectors and topography contours in the innermost grid for IOP 5, 0600 MST 23 Oct. The triangle indicates the location of the ISS site.

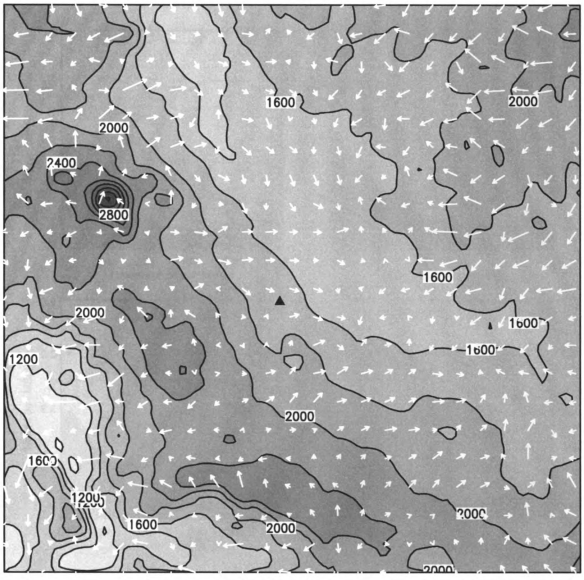

Fig. B.20 Simulated near-surface wind vectors and topography contours in the innermost grid for IOP 5, 0900 MST 23 Oct. The triangle indicates the location of the ISS site.

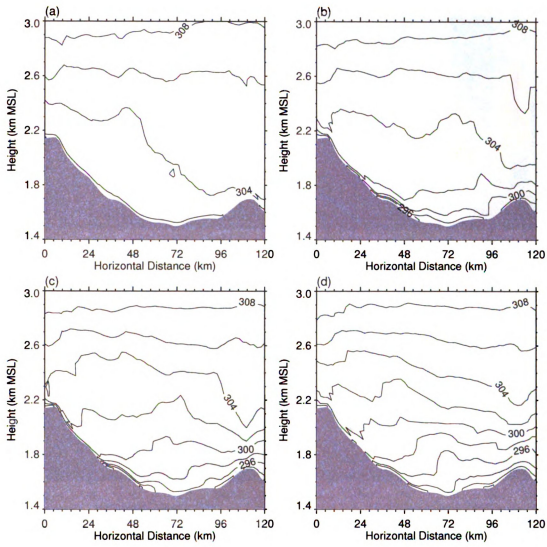

Fig. B.21 Simulated potential temperature on an east-west vertical cross section through the ISS site at (a) 2100 MST, (b) 0000 MST, (c) 0300 MST, and (d) 0600 MST for IOP 5, 22-23 Oct.

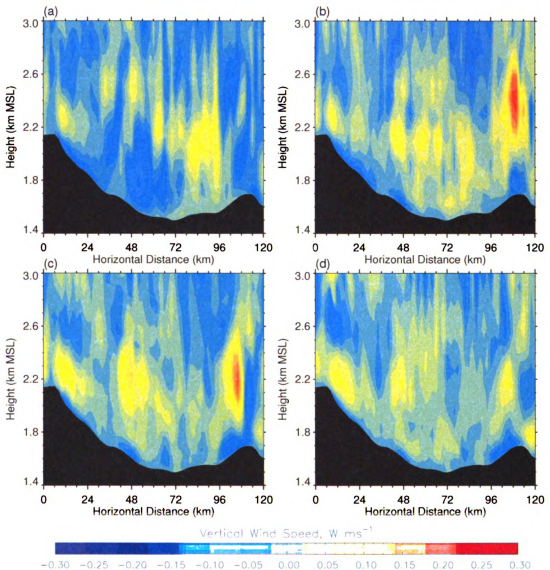

Fig. B.22 Simulated w wind components on an east-west vertical cross section through the ISS site at (a) 2100 MST, (b) 0000 MST, (c) 0300 MST, and (d) 0600 MST for IOP 5, 22-23 Oct. Images in this thesis are presented in color.

f. IOP 6 (RAMS Simulation)

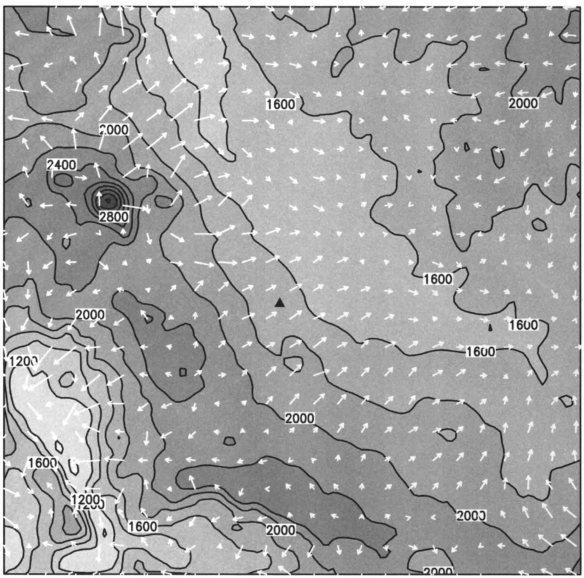

Fig. B.23 Simulated near-surface wind vectors and topography contours in the innermost grid for IOP 6, 2100 MST 28 Oct. The triangle indicates the location of the ISS site.

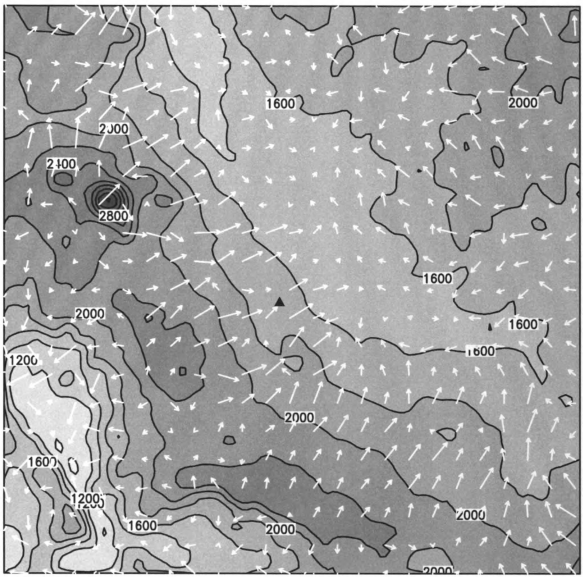

Fig. B.24 Simulated near-surface wind vectors and topography contours in the innermost grid for IOP 6, 0300 MST 29 Oct. The triangle indicates the location of the ISS site.

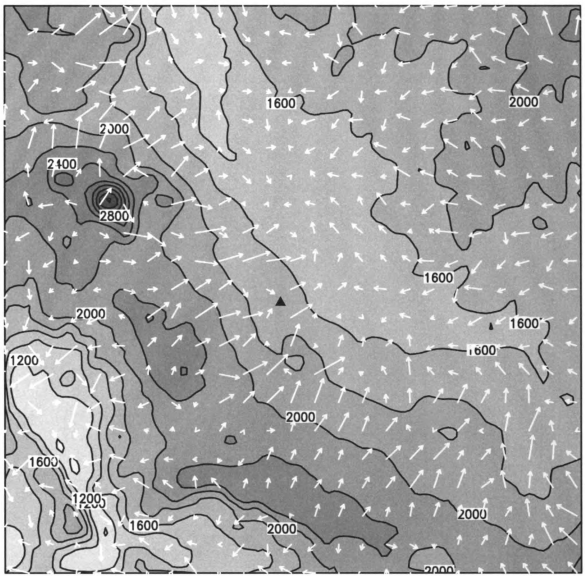

Fig. B.25 Simulated near-surface wind vectors and topography contours in the innermost grid for IOP 6, 0600 MST 29 Oct. The triangle indicates the location of the ISS site.

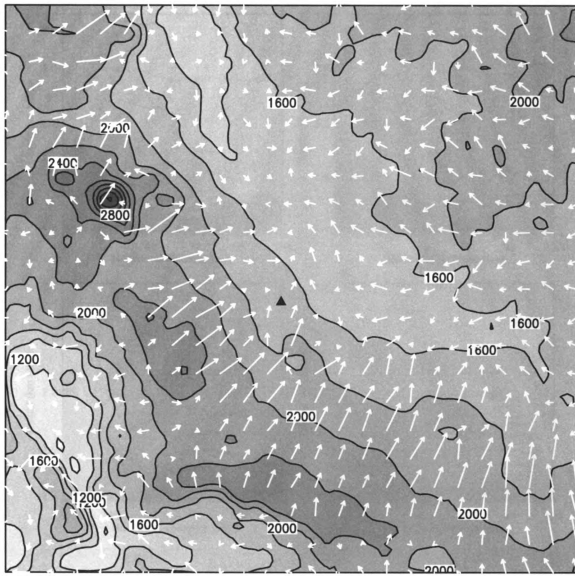

Fig. B.26 Simulated near-surface wind vectors and topography contours in the innermost grid for IOP 6, 0900 MST 29 Oct. The triangle indicates the location of the ISS site.

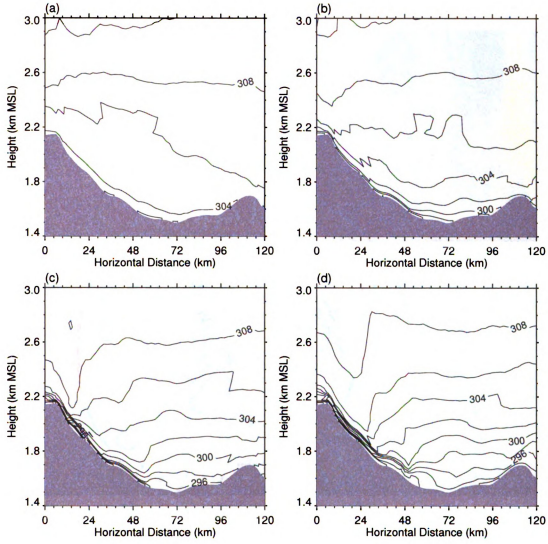

Fig. B.27 Simulated potential temperature on an east-west vertical cross section through the ISS site at (a) 2100 MST, (b) 0000 MST, (c) 0300 MST, and (d) 0600 MST for IOP 6, 28-29 Oct.

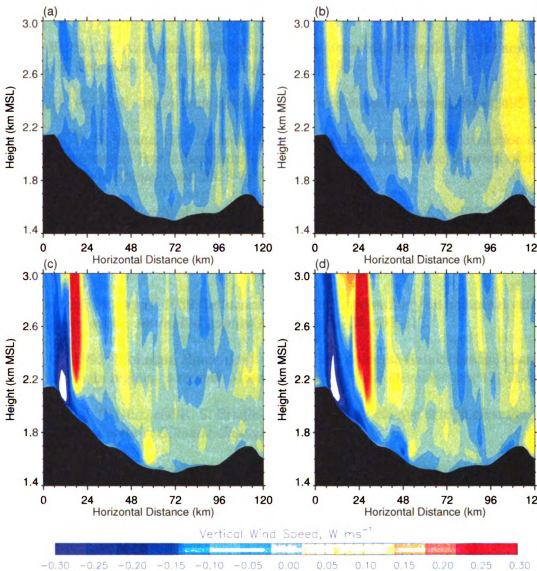

Fig. B.28 Simulated w wind components on an east-west vertical cross section through the ISS site at (a) 2100 MST, (b) 0000 MST, (c) 0300 MST, and (d) 0600 MST for IOP 5, 22-23 Oct. Images in this thesis are presented in color.

References

Alexandrova, O. A., D. L. Boyer, J. R. Anderson, H. J. S. Fernando, and Nt, 2003: The influence of thermally driven circulation on PM10 concentration in the Salt Lake Valley. *Atmospheric Environment*, **37,** 421-437.

Arritt, R. W., and R. A. Pielke, 1986: Interactions of nocturnal slope flows with ambient winds. *Boundary-Layer Meteorology*, **37,** 183-195.

Atkinson, B. W., 1981: *Meso-scale Atmospheric Circulations*. Academic Press, 495 pp.

Bader, C. D., T. B. Mckee, G. J. Tripoli, 1987: Mesoscale boundary layer evolution over complex terrain. Part I. numerical simulation of the diurnal cycle. *Journal of the Atmospheric Sciences*, **44**, 2823-2839.

Ball, F. K., 1956: The theory of strong katabatic winds. *Aust. J. Phys.*, **9**, 373-386.

Banta, R. M., and P. T. Gannon, 1995: Influence of soil-moisture on simulations of katabatic flow. *Theoretical and Applied Climatology*, **52,** 85-94.

Barr, S., and M. M. Orgill, 1989: Influence of external meteorology on nocturnal valley drainage winds. *Journal of Applied Meteorology*, **28**, 497-517.

Barry, R. G., 1992: Mountain climatology and past and potential future climatic changes in mountain regions- a review. *Mountain Research and Development*, **12,** 71-86.

Beniston, M., H. F. Diaz, and R. S. Bradley, 1997: Climatic change at high elevation sites: An overview. *Climatic Change*, **36,** 233-251.

Berg, L. K., and S. Y. Zhong, 2005: Sensitivity of MM5-simulated boundary layer characteristics to turbulence parameterizations, *J. Appl. Meteorol.*, **44**, 1467-1483.

Blackadar, A. K. (1957): Boundary layer wind maximum and their significance for the growth of nocturnal inversions. *Mon. Weather Rev.*, **38**, 283-290.

Bossert, J. E., and W. R. Cotton, 1994a: Regional-scale flows in mountainous terrain 2. simplified numerical experiments. *Monthly Weather Review*, **122,** 1472-1489.

Burt, P. J. A., and D. E. Pedgley, 1997: Nocturnal insect migration: Effects of local winds. *Advances in Ecological Research, Vol 27*, 61-92.

Castelli, S. T., S. Morelli, D. Anfossi, J. Carvalho, and S. Z. Sajani, 2004: Intercomparison of two models, ETA and RAMS, with TRACT field campaign data. *Environmental Fluid Mechanics*, **4**, 157-196.

Chen, C., and W. R. Cotton, 1983: A one-dimensional simulation of the stratocumulus-capped mixed layer, *Boundary Layer Meteorol.*, **25**, 289-321.

Clements, C. B., C. D. Whiteman, J. D. Horel, 2003: Cold air pool structure and evolution in a mountain basin: Peter Sinks, Utah, *J. Appl. Meteor.*, **42**, 752-768.

Cotton, W. R., and Coauthors, 2003: RAMS 2001: Current status and future directions. *Meteorology and Atmospheric Physics*, **82,** 5-29.

Derbyshire, S. H., 1995: Stable boundary-layer modeling: established approaches and beyond. *Boundary-Layer Meteorology*, **90**, 423-446.

Doran, J. C., J. D. Fast, J. Horel, and Rz, 2002: The VTMX 2000 campaign. *Bulletin of the American Meteorological Society*, **83,** 537-551.

Fast, J. D., and S. Zhong, 1998: Meteorological factors associated with inhomogeneous ozone concentrations within the Mexico City basin, *J. Geophy. Res.*, **103**, 18,927-18,946.

Fitzjarrald, D. R., 1984: Katabatic wind in opposing flow. *Journal of the Atmospheric Sciences*, **41,** 1143-1158.

Frye, J. L., and Y. L. Chen, 2001: Evolution of downslope flow under strong opposing trade winds and frequent trade-wind rainshowers over the island of Hawaii. *Monthly Weather Review*, **129**, 956-977.

Grisogono, B., and J. Oerlemans, 2001: Katabatic flow: analytic solution for gradually varying eddy diffusivities. *Journal of the Atmospheric Sciences*, **58**, 3349-3354.

Gudiksen, P. H., J. M. Leone, C. W. King, D. Ruffieux, and W. D. Neff, 1992: Measurements and modeling of the effects of ambient meteorology on nocturnal drainage flows. *Journal of Applied Meteorology*, **31,** 1023-1032.

Haiden, T., and C. D. Whiteman, 2005: Katabatic flow mechanisms on a low-angle slope. *Journal of Applied Meteorology*, **44,** 113-126.

Hanna, S. R., and R. X. Yang, 2001: Evaluations of mesoscale models' simulations of near-surface winds, temperature gradients, and mixing depths. *Journal of Applied Meteorology*, **40,** 1095-1104.

Heinemann, G., and T. Klein, 2002: Modelling and observations of the katabatic flow dynamics over Greenland, *Tellus Dyn. Meteorol. Oceanogr.*, **54**, 542-554.

Holton, J. R., 2004: *An introduction to dynamic meteorology*. Elsevier Academic Press, 529 pp.

Horst, T. W., and J. C. Doran, 1986: Nocturnal drainage flow on simple slopes. *Boundary-Layer Meteorology*, **34,** 263-286.

Jeffreys, H., 1922: On the dynamics of wind. *Quarterly Journal of the Royal Meteorological Society*, **48,** 29-47.

Klemp, J. B., and R. B. Wilhelmson, 1978: The simulation of three-dimensional convective storm dynamics. *Journal of the Atmospheric Sciences*, **35**, 1070-1096.

Köppen, W. P., 1918: Klassification der Klimate nach Temperatur, Niederschlag und Jahreslauf. *Petermanns Geog. Mitt.*, **64**, 193–203; 243–248.

Komatsu, H., N. Hotta, K. Kuraji, M. Suzuki, and T. Oki, 2005: Classification of vertical wind speed profiles observed above a sloping forest at nighttime using the bulk richardson number. *Boundary-Layer Meteorology*, **115,** 205-221.

Kondo, J., T. Sato, and M, 1988: A simple-model of drainage flow on a slope. *Boundary-Layer Meteorology*, **43,** 103-123.

Louis, J. F., 1979: Parametric model of vertical eddy fluxes in the atmosphere. *Boundary-Layer Meteorology*, **17,** 187-202.

Mahrer, Y., and R. A. Pielke, 1975: A numerical study of the air flow over mountains using the two-dimensional version of the University of Virginia mesoscale model. *Journal of the Atmospheric Sciences*, **32**, 2144-2155.

Mahrer, Y., and R. A. Pielke, 1977: The effects of topography on sea and land breezes in a two-dimensional numerical model. *Monthly Weather Review*, **105**, 1151-1162.

Mahrt, L., R. C. Heald, D. H. Lenschow, B. B. Stankov, and I. B. Troen, 1979: An observational study of the structure of the nocturnal boundary layer. *Boundary-Layer Meteorology*, **17**, 247-264.

Mahrt, L., 1982: Momentum balance of gravity flows. *Journal of the Atmospheric Sciences*, **39,** 2701-2711.

Mahrt, L., 1998: Nocturnal boundary-layer regimes. *Boundary-Layer Meteorology*, **88**, 255-278.

Manins, P. C., and B. L. Sawford, 1979a: Model of katabatic winds. *Journal of the Atmospheric Sciences*, **36,** 619-630.

Manins, P. C., and B. L. Sawford, 1979b: Katabatic winds: a field case study. *Quarterly Journal of the Royal Meteorological Society*, **105**, 1011-1025.

Manins, P. C., 1992: Vertical fluxes in katabatic flows. *Boundary-Layer Meteorology*, **60**, 169-178.

Martinez, D., J. Cuxart, and M. A. Jimenez, 2006: Katabatic wind over gentle slope on the Majorca island. *17th Symposium on Boundary Layers and Turbulenc*, 22-27 May 2006, San Diego, CA.

McCumber, M. C., and R. A. Pielke, 1981: Simulation of the effects of surface fluxes of heat and moisture in a mesoscale numerical-model. 1. soil layer, *J. Geophys. Res.*, **86**, 9929-9938.

Mellor, G. L., T. Yamada, and U, 1974: Hierarchy of turbulence closure models for planetary boundary-layers. *Journal of the Atmospheric Sciences*, **31**, 1791-1806.

Monti, P., H. J. S. Fernando, M. Princevac, W. C. Chan, T. A. Kowalewski, and E. R. Pardyjak, 2002: Observations of flow and turbulence in the nocturnal boundary layer over a slope. *Journal of the Atmospheric Sciences*, **59**, 2513-2534.

Mursch-Radlgruber, E., 1995: Observations of flow structure in a small forested valley system. *Theoretical and Applied Climatology*, **52**, 3-17.

Nappo, C., and K. S. Rao, 1987: A model study of pure katabatic flows. *Tellus Series A-Dynamic Meteorology and Oceanography*, **39A**, 61-71.

Neff, W. D., and C. W. King, 1987: Observations of complex-terrain flows using acoustic sounders: Experiments, topography, and winds. *Boundary-Layer Meteorology*, **40**, 363-392.

Orgill, M. M., J. D. Kincheloe, and R. A. Sutherland, 1992: Mesoscale influences on nocturnal valley drainage winds in western Colorado valleys. *Journal of Applied Meteorology*, **31**, 121-141.

Papadopoulos, K. H., C. G. Helmis, A. T. Soilemes, J. Kalogiros, P. G. Papageorgas, and D. N. Asimakopoulos, 1997: The structure of katabatic flows down a simple slope. *Quarterly Journal of the Royal Meteorological Society*, **123**, 1581-1601.

Papadopoulos, K. H., and C. G. Helmis, 1999: Evening and morning transition of katabatic flows. *Boundary-Layer Meteorology*, **92**, 195-227.

Pielke, R. A., and Coauthors, 1992: A comprehensive meteorological modeling system-RAMS. *Meteorology and Atmospheric Physics*, **49**, 69-91.

Pielke, R. A., R. T. McNider, M. Segal, Y. Mahrer, 1983: The use of a mesoscale numerical model for evaluations of pollutant transport and diffusion in coastal regions and over irregular terrain. *Bulletin of the American Meteorological Society*, **64**, 243-249.

Pinto, J. O., D. B. Parsons, W. O. J. Brown, S. Cohn, et al., 2006: Coevolution of down-valley flow and the nocturnal boundary layer in complex terrain. *Journal of Applied Meteorology and Climatology*, **45**, 1429-1449.

Poulos, G. S., 1996: The interaction of katabatic winds and mountain waves., Ph.D. dissertation, Colorado State University, 297 pp.

Poulos, G. S., J. E. Bossert, T. B. McKee, and R. A. Pielke, 2000: The interaction of katabatic flow and mountain waves. Part I: Observations and idealized simulations. *Journal of the Atmospheric Sciences*, **57,** 1919-1936.

Prandtl, L., 1942: Führer durch die Sromungslehre. Vieweg-Verlag, Braunschweig, 367-375.Available in English as *Essential of Fluid Dynamics*. Halner Publisher Co., New York, 1952.

Pypker, T. G., M. H. Unsworth, A. C. Mix, W. Rugh, T. Ocheltree, K. Alstad, and B. J. Bond, 2007: Using nocturnal cold air drainage flow to monitor ecosystem processes in complex terrain. *Ecological Applications*, **17**, 702-714.

Raga, G. B., D. Baumgardner, G. Kok, I. Rosas, and Yx, 1999: Some aspects of boundary layer evolution in Mexico City. *Atmospheric Environment*, **33,** 5013-5021.

Rao, K. S., and H. F. Snodgrass, 1981: A nonstationary nocturnal drainage flow model. *Boundary-Layer Meteorology*, **20,** 309-320.

Renfrew, I. A., and P. S. Anderson, 2006: Profiles of katabatic flow in summer and winter over Coats Land, Antarctica. *Quarterly Journal of the Royal Meteorological Society*, **132,** 779-802.

Ryan, B. C., 1977: A mathematical model for diagnosis and prediction of surface winds in mountainous terrain. *Journal of Applied Meteorology*, **16**, 571-584.

Sang, J., L. Guanming, and B. Zhang, 1999: Numerical modeling for emergency response of nuclear accident. *Journal of Wind Engineering and Industrial Aerodynamics*, **81**, 221-235.

Shapiro, A., and E. Fedorovich, 2007: Katabatic flow along a differentially-cooled sloping surface, *J. Fluid Mech.*, **571**, 149-175.

Skyllingstad, E. D., 2003: Large-eddy simulation of katabatic flows. *Boundary-Layer Meteorology*, **106**, 217-243.

Smith, R., and Coauthors, 1997: Local and remote effects of mountains on weather: Research needs and opportunities. *Bulletin of the American Meteorological Society*, **78,** 877-892.

Smith, C. M., E. D. Skyllingstad, 2005: Numerical simulation of katabatic flow with changing slope angle. *Monthly Weather Review*, **133,** 3065-3080.

Soler, M. R., C. Infante, P. Buenestado, and L. Mahrt, 2002: Observations of nocturnal drainage flow in a shallow gully. *Boundary-Layer Meteorology*, **105,** 253-273.

Sun, H., T. L. Clark, R. B. Stull, and T. A. Black (2006), Two-dimensional simulation of airflow and carbon dioxide transport over a forested mountain Part 1: interactions between thermally-forced circulations, *Agr. Forest Meteorol., 140*, 338-351.

Terjung, W., 1976: Climatology for Geographers. *Annals of the Association of American Geographers,* **66**,199-222.

Thyer, N. H., A theoretical explanation of mountain and valley winds by a numerical method. *Meteorology and Atmospheric Physics*, **15**, 318-348.

Tower, W. S., 1903: Mountain and valley breezes. *Monthly Weather Review,* **31**, 528-529.

Van Der Avoird, E., and P. G. Duynkerke, 1999: Turbulence in a katabatic flow. *Boundary Layer Meteorol.,* **92**, 37-63.

Wang, J. X. L., and J. K Angell, 1999: Air stagnation climatology for the United States (1948-1998), NOAA/Air Resources Laboratory ATLAS No. 1., 1-6.

Whiteman, C. D., 1982: Breakup of temperature inversions in deep mountain valleys 1. observations. *Journal of Applied Meteorology*, **21,** 270-289.

Whiteman, C. D., 1990: Observations of thermally developed wind systems in mountainous terrain. *Atmospheric Processes over Complex Terrain, Meteor. Monogr.*, No. 45, Amer. Meteor. Soc., 5-42.

Whiteman, C. D., and S. Zhong, 2008: Downslope flows in a low-angle slope and their interactions with valley inversions. Part I: Observations. *J. Appl. Meteorol. Climat.* (Forthcoming)

Ye, Z. J., M. Segal, J. R. Garratt, and R. A. Pielke, 1989: On the impact of cloudiness on the characteristics of nocturnal downslope flows. *Boundary-Layer Meteorology*, **49**, 23-51.

Ye, Z. J., J. R. Garratt, M. Segal, and R. A. Pielke, 1990: On the impact of atmospheric thermal stability on the characteristics of nocturnal downslope flows. *Boundary-Layer Meteorology*, **51**, 77-97.

Yu, Y., X. Cai, and X. Qie, 2007: Influence of topography and large-scale forcing on the occurrence of katabatic flow jumps in Antarctica: Idealized simulations. *Advances in Atmospheric Sciences*, **24**, 819-832.

Zammett, R. J., and A. C. Fowler, 2007: Katabatic winds on ice sheets: a refinement of the Prandtl model. *Journal of the Atmospheric Sciences*, **64**, 2707-2716.

Zhong, S. Y., J. D. Fast, and X. D. Bian, 1996: A case study of the great plains low-level jet using wind profiler network data and a high-resolution mesoscale model. *Monthly Weather Review*, **124,** 785-806.

Zhong, S. Y., and J. Fast, 2003: An evaluation of the MM5, RAMS, and Meso-Eta models at subkilometer resolution using VTMX field campaign data in the Salt Lake Valley. *Monthly Weather Review*, **131,** 1301-1322.

Zhong, S., and C. D. Whiteman, 2008: Downslope flows in a low-angle slope and their interactions with valley inversions. Part II: Numerical modeling. *J. Appl. Meteorol.. Climat.* (Forthcoming)